Stony Brook University

Enhanced Spectral Domain Optical Coherence Tomography for Pathological and Functional Studies

A Dissertation Presented

by

Zhijia Yuan

to

The Graduate School

in Partial Fulfillment of the

Requirements

for the Degree of

Doctor of Philosophy

in

Biomedical Engineering

Stony Brook University

August 2010

Stony Brook University

The Graduate School

Zhijia Yuan

We, the dissertation committee for the above candidate for the

Doctor of Philosophy degree, hereby recommend

acceptance of this dissertation.

Yingtian Pan - Dissertation Advisor
Professor, Department of Biomedical Engineering

Emilia Entcheva - Chairperson of Defense
Associate Professor, Biomedical Engineering Department

Jerome Liang - Committee Member
Professor, Department of Radiology

Klaus Mueller - Committee Member
Associate Professor, Department of Computer Science

Congwu Du - Outside Member
Associate Professor, Department of Anesthesiology

This dissertation is accepted by the Graduate School

Lawrence Martin
Dean of the Graduate School

Abstract of the Dissertation

Enhanced Spectral Domain Optical Coherence Tomography for Pathological and Physiological Studies

by

Zhijia Yuan

Doctor of Philosophy

in

Biomedical Engineering

Stony Brook University

2010

Optical coherence tomography (OCT) is a novel technique that enables noninvasive or minimally invasive, cross-sectional imaging of biological tissue at sub-10μm spatial resolution and up to 2-3mm imaging depth. Numerous technological advances have emerged in recent years that have shown great potential to develop OCT into a powerful imaging and diagnostic tools. In particular, the implementation of Fourier-domain OCT (FDOCT) is a major step forward that leads to greatly improved imaging rate and image fidelity of OCT.

This dissertation summarizes the work that focuses on enhancing the performances and functionalities of spectral radar based FDOCT (SDOCT) for pathological and functional applications. More specifically, chapters 1-4 emphasize on the development of SDOCT and its utility in pathological studies, including cancer diagnosis. The principle of SDOCT is first briefly outlined, followed by the design of our bench-top SDOCT systems with emphasis on spectral linear interpolation, calibration and

system dispersion compensation. For ultrahigh-resolution SDOCT, time-lapse image registration and frame averaging is introduced to effectively reduce speckle noise and uncover subcellular details, showing great promise for enhancing the diagnosis of carcinoma in situ. To overcome the image depth limitation of OCT, a dual-modal imaging method combing SDOCT with high-frequency ultrasound is proposed and examined in animal cancer models to enhance the sensitivity and staging capabilities for bladder cancer diagnosis.

Chapters 5-7 summarize the work on developing Doppler SDOCT for functional studies. Digital-frequency-ramping OCT (DFR-OCT) is developed in the study, which has demonstrated the ability to significantly improve the signal-to-noise ratio and thus sensitivity for retrieving subsurface blood flow imaging. New DFR algorithms and imaging processing methods are discussed to further enhance cortical CBF imaging. Applications of DFR-OCT for brain functional studies are presented and laser speckle imaging is combined to enable quantitative cerebral blood flow (CBF) imaging at high spatiotemporal resolutions. An angiography-enhanced Doppler optical coherence tomography (aDFR-OCT) was also demonstrated to enable quantitative imaging of capillary changes for brain functional studies. Lastly, future work on technological development and potential biomedical applications is briefly outlined.

Table of Contents

List of Figures

Acknowledgements

This thesis would not have been possible without the support of many people. Many thanks are given to my adviser, Professor Yingtian Pan, who continually encouraged me in research and patiently helped me in writing scientific publications. During my graduate life he not only provided me innovative ideas, but was also highly supportive of my own. I thank him for his trust in me and the research experience I enjoyed in his group.

I am indebted to Dr. Congwu Du, who greatly helped me on my functional and physiological studies. Many discussions with her have enriched my knowledge on relevant information about the field and helped me greatly to accomplish certain project goals. I would like to thank my colleagues Hugang Ren and Zhen Gong, for helping me in OCT experiments and data analysis, Like Shu and Zhongchi Luo, for LSI studies and performing tedious but crucial animal surgeries for me. In addition, I also have been benefited greatly from many insightful discussions with them and have gained fruitful results.

I am also extremely grateful to professors Emilia Entcheva, Jerome Liang, Congwu Du, and Klaus Mueller for serving on my dissertation committee and for their constructive criticism and comments on the research.

Lastly, I thank my family who supported me to pursue my academic goal far from home, and all my friends in Stony Brook who made my graduate life enjoyable.

Chapter 1 **Introduction**

Medical imaging covers a variety of techniques that create images for clinical purposes or medical sciences. Traditional medical imaging modalities such as ultrasonography, magnetic resonance imaging (MRI), X-ray and computer tomography (CT) imaging, have been developed for long-term and are widely used in medical research and clinical applications. However, due to their limited spatial resolution and inherent technical imperfections, these techniques fail to detect micro-level morphological changes which are crucial to the diagnosis of certain diseases in early stages. On the other hand, although optical imaging techniques such as confocal and multiphoton microscopy are able to provide sub-micrometer spatial resolution, they lack of sufficient imaging penetration and have difficulties performing non-invasive *in vivo* imaging of internal organs.

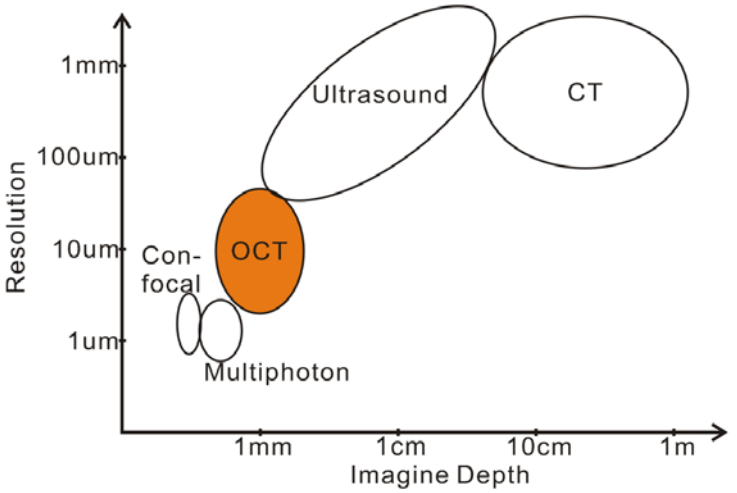

Fig. 1.1 Comparison of different imaging modalities by spatial resolution and imaging depth.

Optical coherence tomography (OCT) is an emerging technique analogous to ultrasound imaging, but provides higher spatial resolution sub ~10μm by taking the advantage of the short wavelengths of light. In addition OCT provides 1-3 mm imaging depth, which is deeper than conventional optical imaging techniques. These unique features, as shown in Fig. 1.1, grant OCT the potential to fill the gap between optical imaging (confocal and multiphoton microscopy) and conventional clinical imaging (ultrasound, x-ray, MRI) modalities[1].

The first demonstration of OCT for high-resolution biomedical imaging was performed in early 90's for imaging eyes[2]. Since then, numerous technological advances have been emerged and dramatically improved the performances of the OCT systems. For instance, Fourier domain OCT (FDOCT) remarkably boosts the imaging rate of OCT up to several hundred frames per second to permit real-time 2D or even 3D imaging and improves image quality[3-5] with reduced system complexity, therefore drastically promoting variant applications of OCT. Doppler OCT as a branch from OCT enables subsurface quantitative flow measurement for physiological and functional studies[6-7]. Polarization and spectroscopic OCT bring extra contrast and sensitivity to OCT to measure specific micro-structures and spectral properties of the sample[8-10]. Recent femto-second laser based ultrahigh-resolution OCT further improves the spatial resolution up to <2μm and demonstrates the potential of sub-cellular imaging [11-15].

Besides its own technical progresses, OCT also allows engineers to miniaturize its optical probes or catheters, i.e., sample arms, by utilizing fibro-optics and various advanced micro laser scanning techniques to enable *in vivo* endoscopic imaging of internal organs and diseases diagnosis in them[16]. Until now, *in vivo* OCT imaging has

been performed for skin[17-18], oral cavity[19], esophagus[20], colon[21], lung[22], bladder[23-25], cervix[26], and intravascular vessels[27] in both animal studies and human clinics, demonstrating the great potential of OCT as a powerful imaging tool for a variety of applications.

Prior to the discussions of techniques to enhanced SDOCT, this chapter first briefly explains the principles of OCT in its two major implementations, time domain OCT (TDOCT) and FDOCT, to help understand this unique imaging technique.

1.1 Michelson interferometer

OCT is based on the light interferometric technique, of which the most commonly used setup is the Michelson interferometer. As plotted in Fig. 1.2, a monochrome light source is usually used to illuminate the interferometer, where the light is spliced into reference and sample arms by a central beam splitter. The light reflected from each of the arms is recombined by the beam splitter and then directed to a photon detector. The electric field of the light from reference (E_R) and sample arms (E_S) can be described in Eq. 1.1 and Eq. 1.2 respectively[28]:

$$E_R = A_R exp\{-i[2kl_R - \omega t]\} \tag{1.1}$$

$$E_S = A_S exp\{-i[2kl_S - \omega t]\} \tag{1.2}$$

where A, k and ω are the amplitude, wavenumber ($2\pi/\lambda$) and angular frequency of the light respectively. The recombined light intensity can be derived accordingly as:

$$I = I_R + I_S + 2\sqrt{I_R I_S}\cos(2k\Delta l) \tag{1.3}$$

where I_R and I_S are the intensity of the light from reference and sample arm respectively, Δl is the path length difference between the two arms. The interference information is contained in the third item on the right: $2\sqrt{I_R I_S}\cos(2k\Delta l)$, which is a cosine function of Δl. By linearly translating the reference mirror to change Δl, a modulated fringe can thus be observed as a sinusoidal signal with a frequency of $2vk$, where v is the moving speed of the reference mirror.

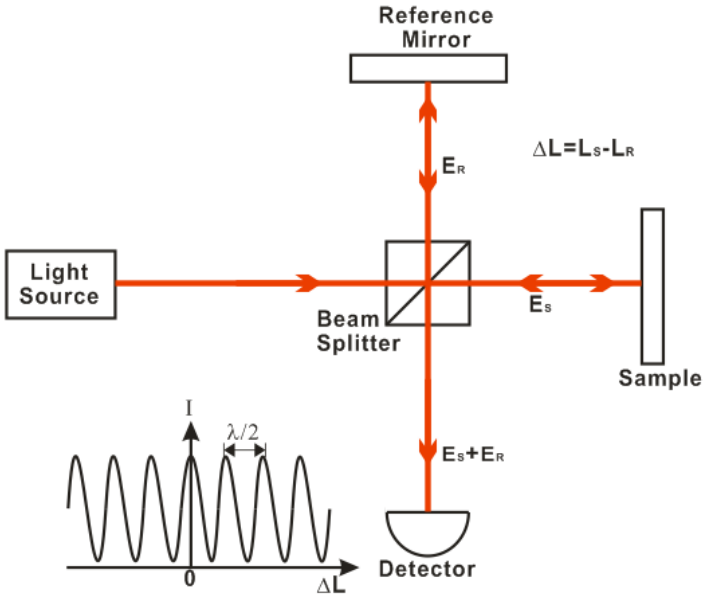

Fig. 1.2 Michelson interferometer

1.2 Low coherence interferometer (LCI)

Different from the monochromatic interferometer discussed above, an LCI uses the same optical setup but a broad band light source instead of monochromatic one to generate a low coherence interferometric signal. When adapted to broad band light, E_R and E_S in Eq. 1.1 and Eq. 1.2 should be rewritten as[28]:

$$E_R(\omega) = A_R(\omega)exp\{-i[2k(\omega)l_R - \omega t]\} \quad (1.4)$$

$$E_S(\omega) = A_S(\omega)exp\{-i[2k(\omega)l_S - \omega t]\} \tag{1.5}$$

Subsequently, the interference signal becomes the sum of each monochromatic component. Considering the most common continuous spectrum, this can be written as the integral over the whole range:

$$I = \int_{-\infty}^{\infty} 2\sqrt{I_R(\omega)I_S(\omega)}\cos[2k(\omega)\Delta l]d\omega \propto Re\left\{\int_{-\infty}^{\infty} S(\omega)\exp[-i\Delta\phi(\omega)]\frac{d\omega}{2\pi}\right\} \tag{1.6}$$

where $S(\omega)$ is the power spectrum:

$$S(\omega) = A_S(\omega)A_R^*(\omega) \tag{1.7}$$

The phase term in Eq. 1.6 can be approximated by Taylor expansions:

$$\Delta\phi(\omega) = k(\omega_0)(2\Delta l) + k'(\omega_0)(2\Delta l)(\omega-\omega_0)(2\Delta l) + \frac{k''(\omega_0)}{2}(\omega-\omega_0)^2(2\Delta l) + ... \tag{1.8}$$

Considering a dispersion-free system, where $k^n(\omega_0) = 0$ for $n \geq 2$, Eq. 1.6 can be simplified as,

$$I \propto \mathrm{Re}\left\{\exp(\frac{-i\omega_0 2\Delta l}{v_p})\int_{-\infty}^{\infty} S(\omega-\omega_0)\exp[\frac{-i(\omega-\omega_0)2\Delta l}{v_g})]\frac{d(\omega-\omega_0)}{2\pi}\right\} \tag{1.9}$$

where $v_p = \omega_0 / k(\omega_0)$, $v_g = \omega_0 / k'(\omega_0)$ are the phase and group velocities respectively. Assume the laser source has a Gaussian power spectrum centered at ω_0:

$$\mathrm{S}(\omega-\omega_0) = \frac{\sqrt{2\pi}}{\sigma_\omega}\exp\left[\frac{(\omega-\omega_0)^2}{2\sigma_\omega^{\,2}}\right] \tag{1.10}$$

which can be normalized so that:

$$\int_{-\infty}^{\infty} S(\omega-\omega_0)\frac{d(\omega-\omega_0)}{2\pi}=1 \tag{1.11}$$

where $2\sigma_\omega$ is the standard deviation of $S(\omega)$. Thereafter, Eq. 1.9 gives:

$$I \propto \mathrm{Re}\left\{\exp\left(\frac{-i\omega_0 2\Delta l}{v_p}\right)\exp\left[-\frac{2\sigma_\omega^2\Delta l^2}{v_g^2}\right]\right\}=\cos(k_0 2\Delta l)\exp(-\frac{2\sigma_\omega^2\Delta l^2}{v_g^2}) \tag{1.12}$$

Here, *'I'* becomes a modulated pulse with a Gaussian envelope as plotted in Fig. 1.3. Considering $v_g = c$ in free space, the full-width-half-maximum (FWHM) of this envelope, i.e., the coherence length, can be given as:

$$L_C = \frac{2\ln 2}{\pi}\left(\frac{{\lambda_0}^2}{\Delta\lambda}\right)\approx 0.44\frac{{\lambda_0}^2}{\Delta\lambda} \tag{1.13}$$

where λ_0 is the central wavelength and $\Delta\lambda$ is the FWHM of wavelength bandwidth.

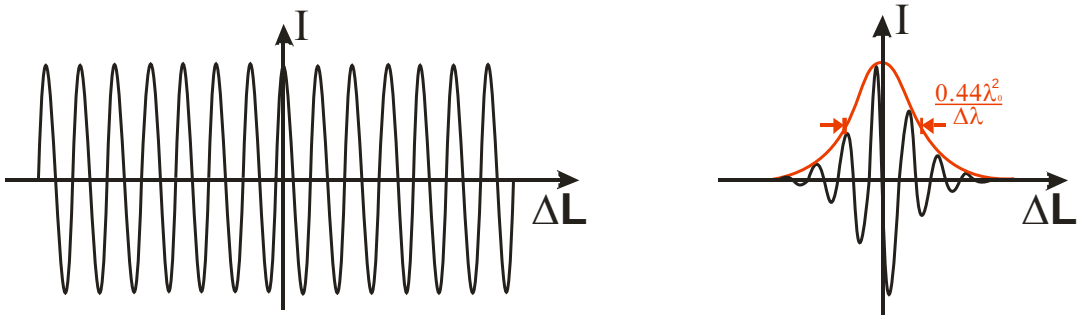

a) interference signal of monochrome light source

b) interference signal of broadband light source

Fig. 1.3 Interference signal of a) monochrome Michelson interferometer vs. b) broadband light source based LCI

1.3 OCT in time domain

Because of its low coherence property, LCI is able to "section" the signal from the sample arm at different depths by translating the reference mirror axially (A-scan), thereby measuring the depth resolved structural profile of the sample, i.e., A-line, with a

resolution defined by its coherence length L_C. By further adding a focusing lens with synchronized scanning scheme at the sample arm to retrieve signals from other dimensions, a prototype of OCT is ready to be built for 2D (B-scan) or even 3D (C-scan) imaging. Fig. 1.4 depicts the setup of an OCT system based on fiber optic LCI, where the light from the broad band source (BBS) is first coupled into single mode fiber and then split by a fiber coupler into the reference arm and the sample arm respectively. The reflected light from the reference arm and the sample arm is recombined and detected by a photodiode detector. Thereafter, an envelope detector extracts the interference signal and then sends it to the computer for image reconstruction and displaying. A-scan in reference arm is performed repeatedly during each step of B-scan to form cross sectional 2D images. By stacking the sequential 2D images acquired in C-scan, OCT is also able to provide 3D images.

Due to the fact that the A-line of the sample is acquired in time series, this OCT implementation is so called Time domain OCT (TDOCT). Apparently, TDOCT needs a fast optical delay line (ODL) in the reference arm to perform accurate and repeatable A-scans. In the early implementations, this was completed by moving piezo stages, which restrained the imaging speed of OCT because of mechanical limitations. The later invention of rapid scanning optical delay line (RSOD)[29] in the Fourier domain drastically improved the A-scan speed, which provided OCT with the capability of instantaneous or real time cross sectional imaging. Currently, the highest speed achieved by TDOCT is around ~8k A-scans per second by using RSOD.

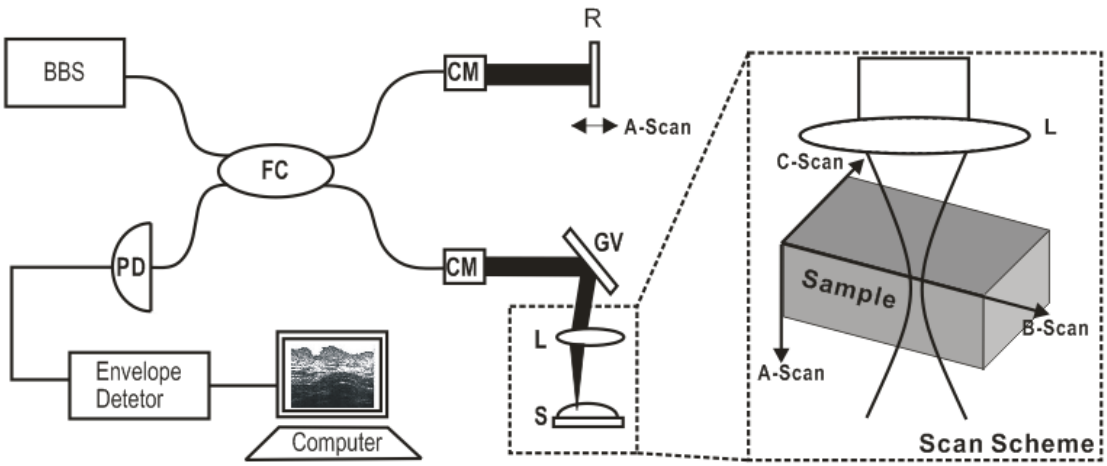

Fig. 1.4 Fiber-optics base OCT setup for 2D and 3D imaging. BBS: broad band light source; FC: Fiber coupler; CM: collimator; PD: Photodiode detector; L: focusing lens; S: sample; R: Reference Mirror.

1.4 Fourier Domain OCT and its challenges

In TDOCT, the detected interference signal *I* is the sum of all wavenumber components of the broadband light and the sample depth profile is encoded in time domain. While in Fourier Domain OCT (FDOCT), the interference signal is spectrally distributed, and the depth profile is encoded in frequency or Fourier domain. To explain this, the spectrally resolved interference signal between reference and sample can be rewritten as[28, 30]:

$$I(k) = S(k)\left\{ A_R \exp(ik \cdot 2r) + \int_0^\infty A_S(z) \exp[-ik \cdot 2(r+nz)]dz \right\}^2 \tag{1.14}$$

where k is the wavenumber, $S(k)$ is the light power spectrum, $2r$ is the matched double-passed pathlength in both reference and sample arm, n is the refractive index of the sample (approximately ~1.35 for biological tissues) and $2(r+nz)$ is the pathlength in sample arm at depth z; A_R is the amplitude of the reference arm and is set to 1 for further investigation; when the pathlength of the sample matches the reference arm, z becomes

the depth within the sample and $A_S(z)$ is the backscattering amplitude from sample at depth z. Assuming that $A_S(z)$ is symmetrically expanded to: $\hat{A}_S(z) = A_S(z) + A_S(-z)$, Eq. 1.14 can then be simplified as:

$$\begin{aligned} I(k) &= S(k)\left\{1+2\int_0^\infty A_S(z)\cos(2knz)dz + \int_0^\infty\int_0^\infty A_S(z)A_S(z')\cos[2kn(z-z')]dzdz'\right\} \\ &= S(k)\left\{1+\int_{-\infty}^\infty \hat{A}_S(z)\cos(2knz)dz + \frac{1}{4}\int_{-\infty}^\infty\int_{-\infty}^\infty \hat{A}_S(z)\hat{A}_S(z')\cos[2kn(z-z')]dzdz'\right\} \end{aligned} \quad (1.15)$$

where the first item is a DC offset, the second item is the spectrally encoded interference signal between sample and reference arm, and the third item is the autocorrelation signal (AC), i.e., the mutual interference within the sample. Apparently, an inverse Fourier transform decodes the backscattering profile $\hat{A}_S(z)$ as:

$$F^{-1}[I(k)] = F^{-1}[S(k)] \otimes \left\{\delta(z) + \frac{1}{2}\hat{A}_S(z) + \frac{1}{8}\mathrm{AC}[\hat{A}_S(z)]\right\} \quad (1.16)$$

As a convolution function, $S(k)$ sets the axial resolution of the system. To retrieve a clear $\hat{A}_S(z)$, it is necessary to minimize the noise induced by the first (DC noise) and third term (AC noise) in Eq. 1.16. In practical application, the AC noise usually locates around z=0 with a negligible intensity (~3 orders lower than the second term), thus can be easily filtered. The DC noise is usually removed by subtracting the baseline signal acquired when sample arm is blocked. Through these steps, the back scattering profile $\hat{A}_S(z)$ can be easily calculated using an inverse Fourier transform of the acquired spectra without any mechanical ODL scan in reference arm.

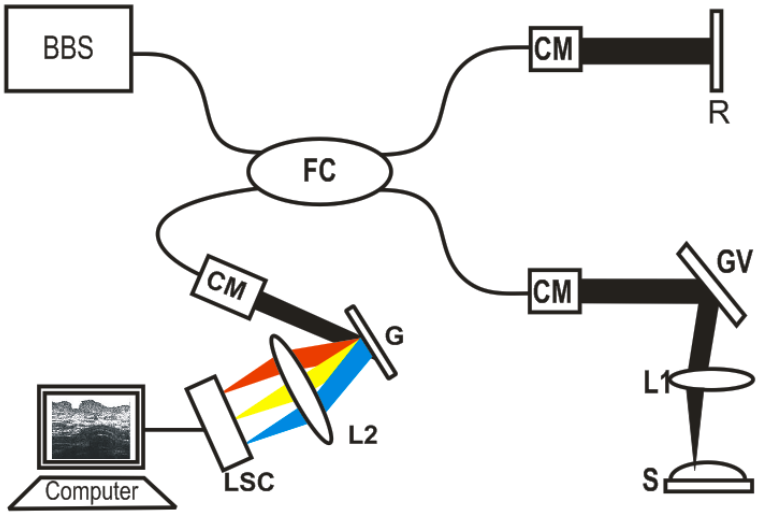

Fig. 1.5 A schematic diagram of SDOCT. BBS: broad band light source; FC: Fiber coupler; CM: collimator; L: focusing lens; S: sample; R: Reference Mirror; LSC: line scan camera

Fig. 1.5 illustrates a typical setup of spectral radar based FDOCT or so called SDOCT, which is similar to the TDOCT in Fig. 1.4 but the reference mirror in Doppler OCT remains static and a spectral radar is built for detecting the spectral interferogram instead of photodiode. The recombined broad band light was collimated and shined onto a diffractive grating, from which different optical frequencies are separated and projected onto a line scan camera (LSC) or a photodiode array (PDA) via a focusing lens. This parallel detecting approach dramatically increases the imaging speed of SDOCT over TDOCT. Currently with commercially available high speed LSC or PDA, the A-line rate of SDOCT reaches up to 20~80 KHz, permitting real-time 2D or instantaneous 3D imaging. Moreover, SDOCT reportedly provides better sensitivity and signal to noise ratio (SNR) from longer exposure times of the spectral radar (~20μs for 50K A-line rate), during which all the photons from each layer of the sample will be integrated to generate the OCT signal[31]. On the contrary, the signal in TDOCT is coherence gated to extremely short time period (~1μs for 1K A-line rate with 1000 samples each A-line),

thus introducing considerable noise. It's also noteworthy that with the virtue of Fourier transform, SDOCT provides a convenient way to extract the phase shift induced by Doppler effects and therefore simplifies the performance of Doppler flow measurements for functional studies using OCT.

Despite these obvious advantages, SDOCT also suffers its own technical limitations. Firstly, according to the Nyquist–Shannon sampling theorem, the imaging depth of SDOCT is limited to:

$$D = \frac{N}{4n\Delta k} = \frac{N\lambda_1\lambda_N}{4n(\lambda_N - \lambda_1)} \tag{1.17}$$

where D is the deepest imaging depth, N is the pixel number or sampling point number, Δk is the wavenumber range, λ_1 and λ_N are the shortest and longest wavelengths of the detectable range respectively. Since the camera detects the convolution of the focus profile and the pixelated quasi-rectangular portion of an optical frequency range instead of a single frequency, the spectral resolution is limited and causes a depth dependent fall-off of the signal from the zero delay. Additionally, because the dispersive element, the diffraction grating in the spectral radar, distributes the optical frequency nonlinearly onto the detector the spectral interferogram has to be re-sampled linearly in wavenumber or *k*-space to facilitate the Fourier transform. This calibration step also introduces computation load and potential artifacts that compromise the overall performance of the system. Moreover, other technique imperfections and physical limitations, such as speckle noise, inadequate imaging depth, and excessive Doppler phase noise, still remain as unresolved problems that greatly compromised the utility of OCT.

In this dissertation, several methods are proposed to address some of these

problems to enhance our SDOCT systems for both pathological and functional studies. To be more specific, the major work in this dissertation can be listed as follows:

1. Design the spectral radar to improve the spectral resolution and optimize the data acquisition and processing procedures for high speed artifact-free OCT imaging
2. Clinical trials demonstrated that OCT provides superior sensitivity and specificity over traditional methods for bladder cancer diagnosis. However, due to the limited imaging depth, OCT often fails to delineate the invading tumor edge for staging. Combining ultrasound with OCT for parallel imaging can potentially solve this problem. Prior to this, a detailed comparison of these two techniques for cancer diagnosis and staging is necessary.
3. Speckle noise is the major hindrance for uOCT when resolving sub-cellular structures of biological tissues, preventing the utilization of uOCT for precise clinical diagnosis, such as the grading of cancer which is of great importance for appropriate treatments. Recently, sub-cellular uOCT was demonstrated using frame averaging method[15] in time domain. However, to enable *in vivo* imaging, uOCT has to run at much higher speed to prevent severe motion artifacts. Therefore, the frame averaging method has to be modified and adapt to SDOCT to enable faster sub-cellular imaging.
4. SDOCT can work as Doppler OCT (Doppler OCT) to measure Doppler shifts as a map of dynamic flow imaging. However it suffers from excessive phase noises induced from different sources including multiple scattering, speckle noise, sample heterogeneity, amplitude shot noise, phase wrapping artifacts,

or even handshaking when used as *in vivo* endoscope. A new numerical algorithm is proposed to quantify Doppler phase signal with higher SNR than conventional method. In addition, several image processing techniques were described to further improve the performance of current Doppler OCT.

5. Although real-time 2D OCT imaging has already been achieved, 3D imaging is still considered to be time consuming. To enable quantitative CBF imaging with high spatiotemporal resolution, OCT was combined with another complementary technique, laser speckle imaging to investigate the utility of this parallel imaging system in drug challenged brain functional studies.

It is noteworthy that the spectral interferogram in FDOCT can be either time encoded by swept source or spatially encoded by spectral radar. The implementations of them are regarded as swept source OCT (SSOCT) and SDOCT respectively. Until now, all the work and methods presented in this dissertation was conducted on SDOCT systems. Nevertheless, all the methods and conclusions in this dissertation are theoretically applicable to SSOCT as well.

Chapter 2 Development of SDOCT systems

This chapter focuses on the design of two SDOCT systems at ~1310nm and ~800nm respectively and the optimization of them in spectral resolution, data processing and dispersion compensation. Since the process of building these two systems are almost identical to each other, we only describe the design details of the system at ~1310nm and briefly cover the other.

2.1 Design of Spectral Radar

As shown on the top left of Fig. 2.1 the spectrum of light source used is centered at 1310nm, with a FWHM bandwidth of ~90nm and a usable range of ~120nm from ~1250nm to ~1370nm, which provides a theoretical axial resolution of ~8μm in free space. The spectral radar is illustrated on the right of the figure. The InGaAs camera has a linear PDA of 1024 pixels with 25μm pitch size, providing a sampling density of about 0.93 points per nm, and an imaging depth of 2.9mm based on Eq. 1.17. According to the Littrow condition, the angle between incident light and diffracted light should be as small as possible for the best diffraction efficiency. Thus, the minimum angle in cage system design was used:

$$\Delta\theta = \theta_i - \theta_{t0} = 12.5^\circ \tag{2.1}$$

where $\Delta\theta$ is the angle between the incident light (black trace) and the first order diffraction of central wavelength (green trace). The diffraction formula gives:

$$d\left(\sin\theta_i + \sin\theta_{t0}\right) = m\bar{\lambda} \tag{2.2}$$

where $\bar{\lambda}$ is the central wavelength of 1310nm and m is the diffraction order that equals to 1. To match the required wavelength detecting range, a standard holographic grating with d^{-1}=1200 l/mm is used. Thereafter, by combining Eq. 2.1 and 2.2, θ_i and θ_{t0} can be calculated as 59^o and 46.5^o respectively and $\Delta\theta_t$ is set to be ~5.1^o. The focus length of the lens L before the camera is then given as:

$$f = \Delta x / \tan\Delta\theta_t \tag{2.3}$$

where Δx=12.5 is the half dimension of the linear PDA, thus f is calculated to be ~140mm. The focus size should be smaller than the camera pixel size (25μm) to achieve the ultimate spectral resolution of the camera:

$$1.22 f\bar{\lambda}/\phi < 25\mu m \text{ or } \phi > 9mm \tag{2.4}$$

where ϕ is the beam size of the incident light and was collimated to 10mm. Based on the above design parameters, the system detects a wavelength range from 1255nm~1365nm, with a theoretical spectrum resolution of ~0.11nm and an imaging depth of 2.9mm in biological tissues (n=1.35).

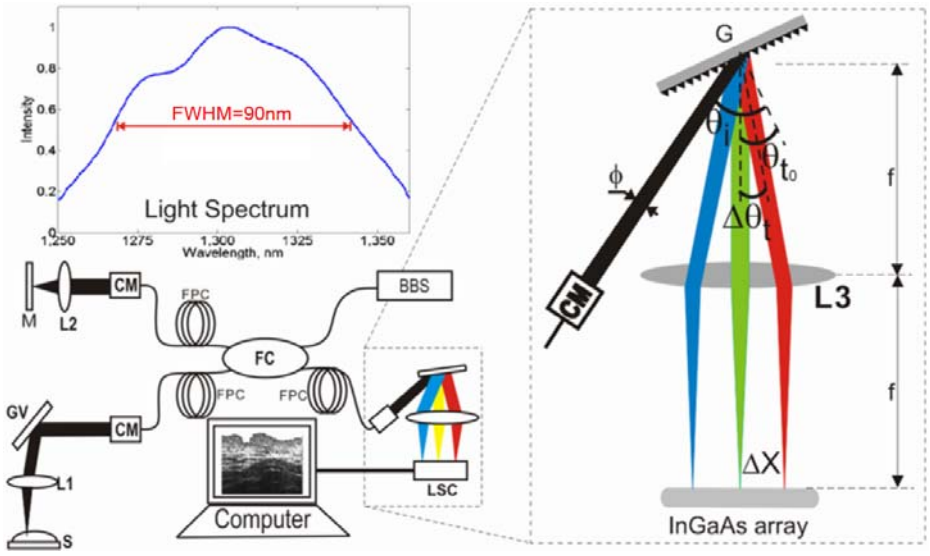

Fig. 2.1 Schematic diagram of SDOCT system at ~1310nm. BBS: broad band light source; FC: Fiber coupler; FPC: fiber polarization controller; CM: collimator; L: focusing lens; S: sample; R: Reference Mirror; LSC: line scan camera. Design parameters of the spectral radar: ϕ=10mm, f=140mm, incident light angle θ_i=59^o, grating offset angle θ_{t0}=46.5^o, grating density: d^{-1}=1200 l/mm, camera pixel size: 25μm × 1024

After the installation of spectral radar, an SDOCT system can be easily built based on the illustration in Fig. 2.1. The broad band laser was pigtailed into a single mode fiber and then split equally by a 2×2 fibreoptic coupler into sample and reference arm. The reference arm was connected to a stationary mirror to match the optical path lengths. The sample arm was connected to a stereoscope in which light exiting the fiber was collimated to 5mm, scanned laterally by a servo mirror, and focused by an f=40mm achromatic lens onto the sample under examination. The light returning from the sample and the reference arms were recombined in the detection arm on the way to the spectral radar built above. As discussed in section 2.2, a lab built program retrieved each spectral interferogram from the camera by camera-link and converted it to A-scan profile of the sample by inversed Fast Fourier Transform (FFT). Sequential, transverse scans of the sample beam were synchronized after acquisition of each spectrograph/A-line so that 2D

OCT images can be reconstructed and displayed at ~47fps and 1000×1024 resolution. The measured axial and lateral resolutions were $8\times12\mu m^2$ in biological tissues and the system dynamic range was measured to be ~111dB.

Spectral domain ultrahigh resolution OCT (SDuOCT) system can be built according to the same design procedure. An ultra broad band $Ti:Al_2O_3$ laser with center wavelength at $\bar{\lambda}$ =800nm and the spectrum FWHM $\Delta\lambda$=128nm were utilized to provide a theoretical axial resolution of ~2.2um in free space. A commercially available CCD camera with 10μm×2048pixel sensors was installed to collect the focused spectrogram. Based on thesis construction, the parameters of the spectral radar in SDuOCT were calculated to be: light beam diameter ϕ=10mm, focus length of L3 f=80mm, incident light angle $\theta_i=36.9^o$, grating offset angle $\theta_{t0}=21.4^o$, grating density: d^{-1}=1200 l/mm. The usable wavelength range is from ~700nm to ~900nm with a theoretical spectrum resolution of ~0.1nm, providing an imaging depth of 1.2 mm in biological tissues (n=1.35). To roughly match the axial and later resolution, the light in the sample arm of SDuOCT was collimated to Φ5mm and focused by a short focus (f=16mm) achromatic lens to yield a lateral resolution of ~3um. In addition, a pair of BK7 wedge prisms was placed in the sample path to balance the dispersion between sample and reference arm.

2.2 Data Acquisition (DAQ) and Processing

To acquire the spectra and process the data a customized C++ program was built, the framework of this program is demonstrated in Fig. 2.2. The program consists of four modules: data acquisition, calibration, FFT and image display, which were run by different threads and a main thread manages the data exchange between these modules. In

order to make the program adaptive, the modules were well encapsulated and can be independently modified to fit different camera interfaces and add extra processing modules. This multithread design further enhanced the program speed by taking the advantage of multi-core CPUs. More specifically, a well known FFT C library from FFTW[32] was utilized to compute the FFT with optimized performances, and a free tiff library was used to save the raw spectra in tiff format[33] for better disk access. Besides the enormous computation load of data acquisition and processing, the real time refreshing of the reconstructed OCT images in the UI also demands considerable computing resources. Therefore, the image display thread was built on Direct2D which is much faster than windows graphics device interface (GDI) [34].

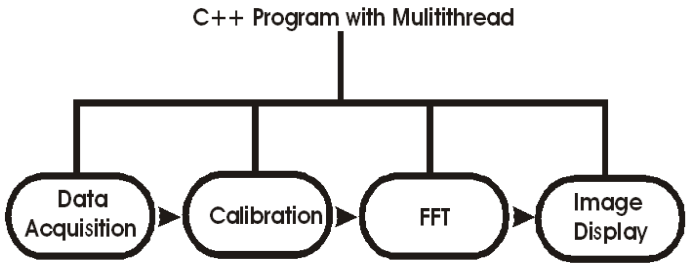

Fig. 2.2 Diagram of the SDOCT program. To enhance the imaging speed, the program is divided into four processing modules that run their own threads. With this multithreading technique, speed performance is improved 80% on a computer with dual-core CPU.

Fig. 2.3 displays the user interface (UI) of the program. The window in panel (A) is the control panel for program configurations including camera setting, galvo-scanner and translation stage driving, data saving and accessing; the top graphic window in panel (B) shows the spectrum and intensity profile of the selected A-line; the windows in panel (C) and (D) displays the 2D cross sectional OCT image and the corresponding phase mapping image of dynamic flows, respectively.

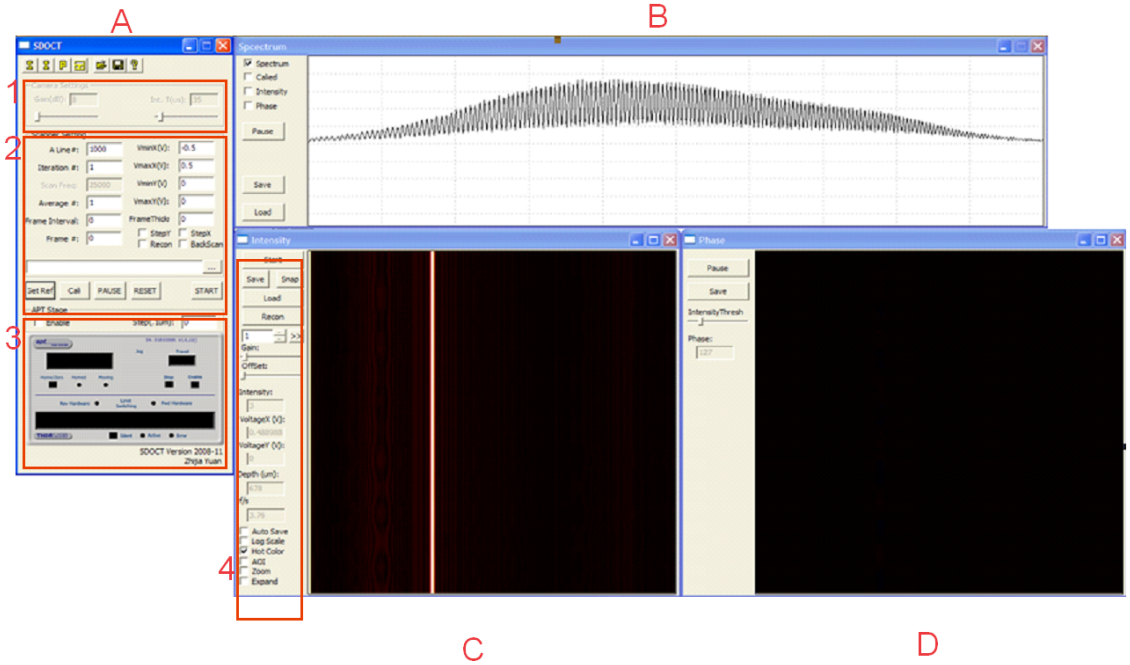

Fig. 2.3 User interface of the SDOCT program. Window A: Control panel, where red box 1 configures camera. 2 controls scanning scheme and data accessing, 3 controls the translation stage; window B: individual spectrum and A-line profile preview; window C: OCT cross sectional structural image window, where red box 4 configures the display options and shows pixel information; window D: phase image window.

2.3Dispersion compensation with improved calibration method

In OCT system, almost all optical components including the focusing lens, collimators, unmatched fiber leads between samples, reference arms, and diffraction grating induce dispersion, which is found to be negligible for ~1310nm SDOCT when roughly matched between sample and reference arms, but could still drastically compromise the axial resolution and thus the contrast of SDuOCT images. Therefore, the dispersion between the sample and reference arms in an SDuOCT system must be balanced, which has often been implemented by inserting dispersive materials[35-37]. Although a grating-lens-based rapid-scanning optical delay (RSOD) in the reference arm of time-domain uOCT can provide additional dispersion adjustment by shifting the

grating off the focal plane[38-39], a thorough compensation for the unbalanced dispersion in SDuOCT, by using either insertion of dispersive material or fine adjustment of RSOD and in most cases both methods, remains a technical challenge due to predominant higher-order dispersions.

Recent studies in SDOCT have found that the group delay dispersion (GDD) can be retrieved by analyzing the preserve phase of spectral interferograms[40-44], thereby allowing numerically compensation of dispersion, i.e., wavelength-dependent phase distortion. As a matter of fact, most of these methods were based on introducing an anti-dispersion phase function and multiplying it with the original interferogram so as to minimize the overall dispersion[41]. To retrieve the anti-phase function, however, iterative numerical approaches had to be applied by either maximizing image sharpness[42] or minimizing the entropy[43], and as a result these methods could be computation intensive. Therefore, a method that can directly and instantaneously measure the dispersion-induce nonlinear phase errors is desirable for fast and accurate dispersion compensation, especially for SDuOCT.

Spectral calibration, converting a measured raw interferogram from λ- to k-space in SDOCT, is critical to the reconstruction of a SDOCT image, in particular, for SDuOCT. Calibration approaches include parametric iteration, fringe mapping, auto calibration and phase linearization [36, 45-48], among which phase linearization provides an easy solution by processing a single frequency spectral interferogram. Here we further optimized the phase linearization method, in which a dispersion-free spectral interferogram (baseline) is acquired first by measuring the autocorrelation between two air-gap glass interfaces, i.e., error-free spectral calibration. Then a simple linear

interpolation look-up-table (LUT) is calculated for instantaneous and accurate spectral calibration. Thereafter a cross-correlation spectral interferogram is acquired and calibrated using this LUT, and the GDD-induced phase distortion between the sample and reference arms is retrieved via Hilbert transform and corrected by removing the nonlinear phase components. As a result, the dispersion is compensated and the system axial resolution can be effectively recovered. To demonstrate the efficacy of this method, the simulations and experiments were performed for SDuOCT and the results were presented below, yet the method is also applicable for the standard SDOCT.

2.3.1 Dispersion-free Spectral Calibration

In a dispersion-free system, the detected spectral interferogram that encodes depth-dependent backscattering can be described as [28, 30]:

$$I(k) = S(k)(1 + 2\int_0^\infty a(z)\cos(2kz + \phi(z))dz + \int_0^\infty\int_0^\infty a(z)a(z')e^{-i2k(z-z')}dz\,dz') \qquad (2.5)$$

where the first term is the DC signal from the reference arm that can be easily filtered out digitally, the third term is the autocorrelation signal (AC) from the sample arm that is negligible for most biological tissue imaging. The 2nd term represents the cross-correlation in which the depth profile (i.e., A-line) *a(z)* is frequency modulated or encoded in the *k*-space ($k=2\pi/\lambda$ is wave number). Apparently, the measured raw spectral interferogram *I(λ)* must be uniformly re-sampled to *I(k)* prior to FFT for OCT image reconstruction[49], which can be implemented by phase linearization[47]. However, phase distortion caused by dispersion mismatch must be eliminated in this process. To do so, a dispersion-free single-frequency modulated spectral interferogram is required, which, in our study, was acquired by measuring the AC term from two air-gaped glass

interfaces whose separation determined the spectral modulation frequency. This process is illustrated in Fig. 2.4 in which panels (b, c) are a recorded spectral interferogram or AC modulation and the result of FFT, respectively. Signal processing, e.g., digital filtering using red-squared window functions was applied to remove the DC offset and random noises. Panels (d,e) show the amplitude term after iFFT and the corresponding phase term ϕ_0 retrieved from the analytic signal of the spectral interferogram by Hilbert transform. As a result of non-uniform sampling in *k*-space, ϕ_0 (blue curve) deviates from the red linear curve ϕ_c intercepting $\phi_0(1)$ and $\phi_0(2048)$ that corresponds to the counterpart of uniform sampling in *k*-space. As shown in panel (f), a linear phase point $\phi_c(n)$ falls in between two neighboring points of $\phi_0(m)$ and $\phi_0(m+1)$ and can thus be linearly interpolated as:

$$\phi_c(n) = w(n)\cdot\phi_0(m) + (1-w(n))\cdot\phi_0(m+1),\ n=1,2,3,\ \ldots,\ 2048 \tag{2.6}$$

where *m* and *n* represent the discretely sampled *k* values, and *w(n)* is the weighting coefficient:

$$w(n) = \frac{\phi_c(n) - \phi_0(m+1)}{\phi_0(m+1) - \phi_0(m)} \tag{2.7}$$

Because of the linear relationship between *k* and ϕ_c, the calibrated discrete spectral interferogram *I(n)* in Eq. 2.5 can be calculated by

$$I(n) = w(n)I_0(m) + (1-w(n))I_0(m+1) \tag{2.8}$$

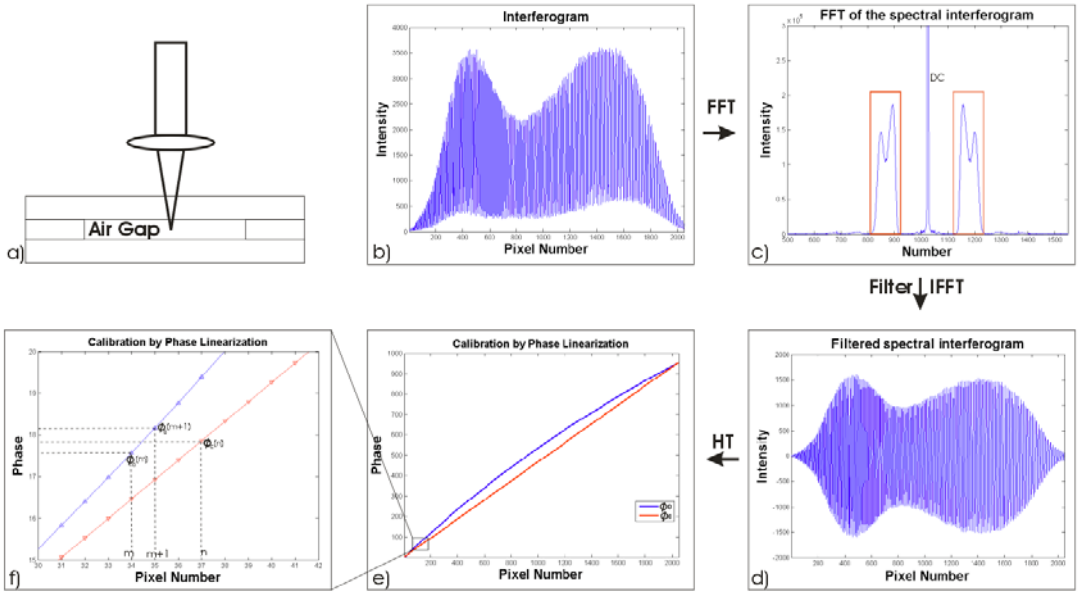

Fig. 2.4 Graphic illustration of dispersion-free spectral calibration. a) air-gap calibration chamber for acquisition of autocorrelation function (i.e., dispersion-free interferogram); b) a recorded raw interferogram, c) noise filtering using square window in Fourier domain, d) filtered spectral interferogram, e) phase linearization, and f) magnified view of a section in e) to illustrate the phase linearization algorithm

Accordingly, a LUT consisting of weighting coefficient w and index m can be generated for fast spectral calibration (i.e., spectral linearization). Since a dispersion-free AC interferogram is used to acquire the LUT, the dispersion-induced errors or phase distortion is eliminated. Fig. 2.5 compares the calibrated and uncalibrated point spread functions (PSFs) which were acquired by measuring the cross-correlation functions between reference and the sample mirrors at different depth mismatches z. The results show dramatic improvements on both signal strength and axial resolution Δz; the broadening of Δz for $z>1$mm was less than 10%, exceeding the calibration performances of other numerical approaches such as parametric iteration and fringe mapping. Therefore, this simple dispersion-free linear interpolation method is faster and more accurate than other higher-order curve fitting and interpolation algorithms.

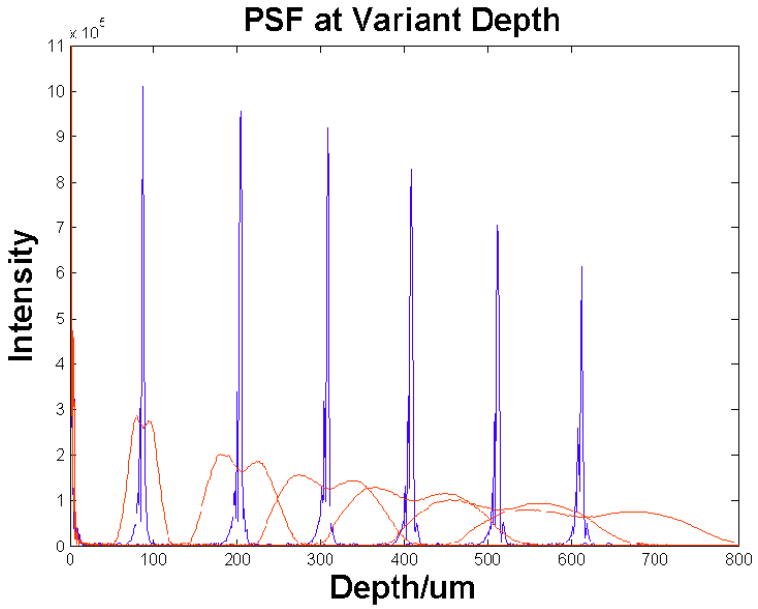

Fig. 2.5 Point spread functions (PSFs) versus pathlength mismatch. The performances (e.g., axial resolution and peak amplitude) of the PSFs (blue curves) after spectral calibration were significantly better than the uncalibrated counterparts (red curves) which showed obvious deterioration along the depth

2.3.2 Dispersion Compensation

As shown in Fig. 2.5, because of unbalanced GDD between sample and reference arms, the measured FWHM axial resolution (Δz=3.2±0.2μm) based on cross-correlation functions was ~35% broader than the theoretical value of $\Delta z \approx 2.4\mu m$ (under transform limit with GDD=0). For GDD compensation, a nonlinear phase delay in *k*-space $\phi_d(n)$ can be introduced to the spectral interferogram to represent the phase distortion induced by the unbalanced system GDD; thereby, the cross-correlation term after spectral calibration can be rewritten as[28, 30]:

$$I(n) = S(n) \cdot \int_0^{\infty} a(z) cos(2nz + \phi_d(n) + \phi_z(z)) dz \tag{2.8}$$

where n is the sampled *k* value and the AC and DC terms in Eq. 2.5 are neglected for mathematical simplicity. Fig. 2.6 illustrates the procedure to characterize $\phi_d(n)$, in which

panel (a) shows a trace of the measured cross-correlation spectral interferogram for a mirror placed at z in the sample arm to generate a high-frequency spectral modulation ($k=2z$) that can be sufficiently resolved by the CCD camera. Similar to spectral calibration, $\phi(n)$ is calculated from the analytic signal by applying Hilbert transform on $I(n)$ as illustrated in panels (b, c), and the disperse-induced nonlinear phase distortion, i.e.,

$$\phi_d(n) = \phi(n) - \phi_l = \phi(n) - n \cdot \frac{\left(\phi(2048) - \phi(1)\right)}{2048} \tag{2.9}$$

where the blue curve in panel (d) is $\phi(n)$, and the red curve is its linear component $\phi_l(n)$. With $\phi_d(n)$ retrieved, the dispersion-free spectrally calibrated interferogram in Eq. 2.9 can be derived as:

$$\begin{aligned} I_{corr}(n) &= S(n) \cdot \int_0^\infty a(z)\cos(2nz + \phi_z(z))dz \\ &= S(n) \cdot \int_0^\infty a(z)\{\cos[\phi_d(n)] \cdot \cos[2nz + \phi_d(n) + \phi_z(z)] + \sin[\phi_d(n)] \cdot \sin[2nz + \phi_d(n) + \phi_z(z)]\}dz \\ &= \cos[\phi_d(n)] \cdot I(n) + \sin[\phi_d(n)] \cdot H[I(n)] \end{aligned} \tag{2.10}$$

where H is Hilbert transform operator. It is noteworthy that the GDD induced by the biological tissue itself is not taken into account in Eq. 2.10, which may result in noticeable effect on SDuOCT imaging at depths of 1-2mm or more (e.g., in the cases of intraocular imaging). To further correct this dispersion, we assume that the GDD induced by most soft tissue can be approximated by saline and compensated accordingly using Eq. 2.10. The phase difference $\phi_s(n)$ induced by the GDD of saline per unit thickness (e.g., 1mm) can be easily measured using the above method; then the phase distortion $\phi_s(n, z)$ of a biological tissue at depth z can be scaled up, i.e., $\phi_s(n, z)=z\phi_s(n)$, and

applying it to Eq. 2.10 yields the GDD correction for all the synthesized spectral interferograms:

$$I_{corr}(n, z_i) == \cos[z_i \cdot \phi_s(n)] \cdot I(n) + \sin[z_i \cdot \phi_s(n)] \cdot H[I(n)] \tag{2.11}$$

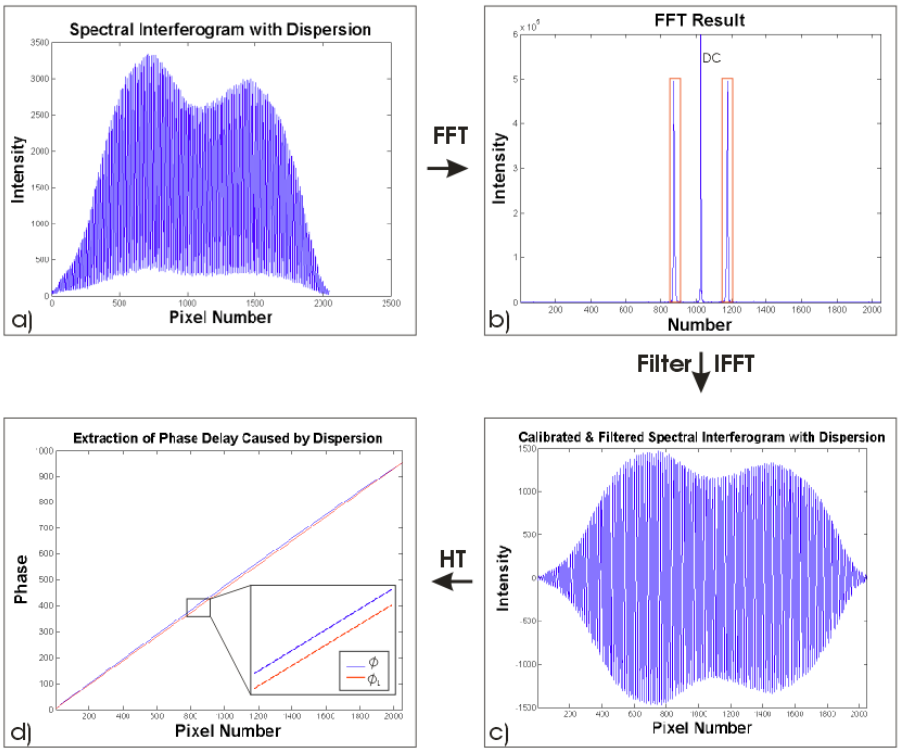

Fig. 2.6 Graphic illustration of numerical GDD compensation. a) measured cross-correlation function with GDD induced by a dispersive glass slide; b, c) noise filtering using square window in Fourier domain and the resultant spectral interferogram; d) phase linearization for $\phi_d(n)$ extraction. The difference between the blue phase curve and its linear component (red curve) is the GDD-induced phase distortion $\phi_d(n)$.

To examine the effectiveness of this method, we compared the reconstructed PSDs of the cross-correlation functions before and after dispersion compensation using our algorithm, Eq. 2.11. The results in Fig. 2.7 clearly show that not only the signal strength (i.e., SNR) is doubled but also the axial resolution is markedly enhanced. The measured axial resolution of Δz=2.5±0.2μm closely matches the transform limit (GDD=0)

of Δz=2.4μm, suggesting that this simple method enables accurate compensation of unmatched GDD in our fiberoptic SDuOCT system.

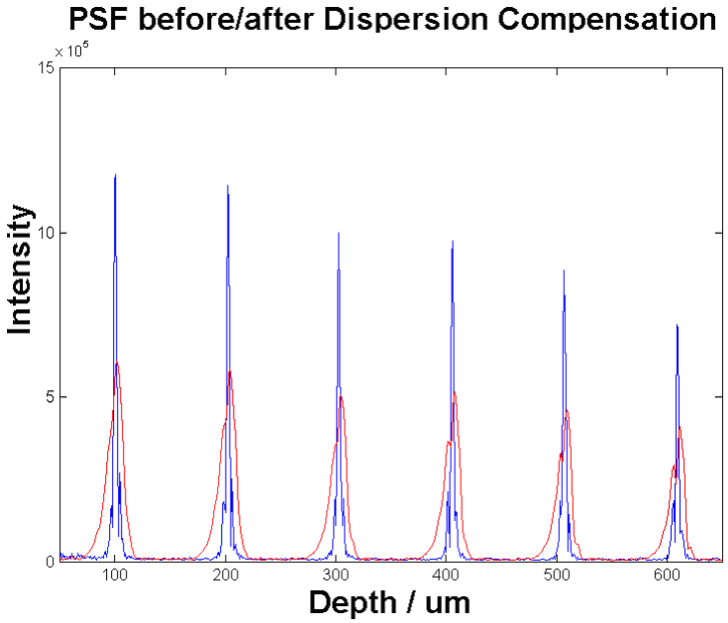

Fig. 2.7 Point spread functions (PSFs) versus pathlength mismatch. Dispersion compensation substantially improves the axial resolution (FWHM) with doubled signal strength. The performances (e.g., axial resolution and peak amplitude) of the PSFs (blue curves) after GDD compensation were significantly better than the counterparts (red curves) without GDD compensation.

To further examine the utility of this method in SDuOCT imaging of biological tissue, we applied the algorithm to a rat bladder image. Fig. 2.8 compares the SDuOCT images of a fixed rat bladder reconstructed using different GDD compensation approaches. Panel (a) was acquired by inserting dispersive material (e.g., BK7 prism pair) to minimize the unbalanced dispersion. Panel (b) was acquired after inserting additional 2mm-thick cover glass in the sample arm to induce extra GDD, thus resulting in noticeably degraded image quality. Panel (c) was the result obtained using Eq. 2.11 to compensate the induced GDD; panel (d) was the result of complete dispersion compensation using Eq.(8) which included the dispersion induced by the biological tissue

itself. For detailed comparison, a small area of interest (AOI) in each panel was chosen to evaluate the difference in image contrast and resolution. Because of high GDD, the image details in panel (b) were severely blurred so that the features such as highlighted by a blue arrow were barely identifiable. Also, a more careful comparison of the same spot reveals that the features (e.g., SNR, boundary sharpness) in panels (c, d) were than those in panel (a), thus evidencing that our phase linearization approach can offer more effective GDD compensation and thus enhanced SDuOCT image quality than the conventional counterpart using material compensation.

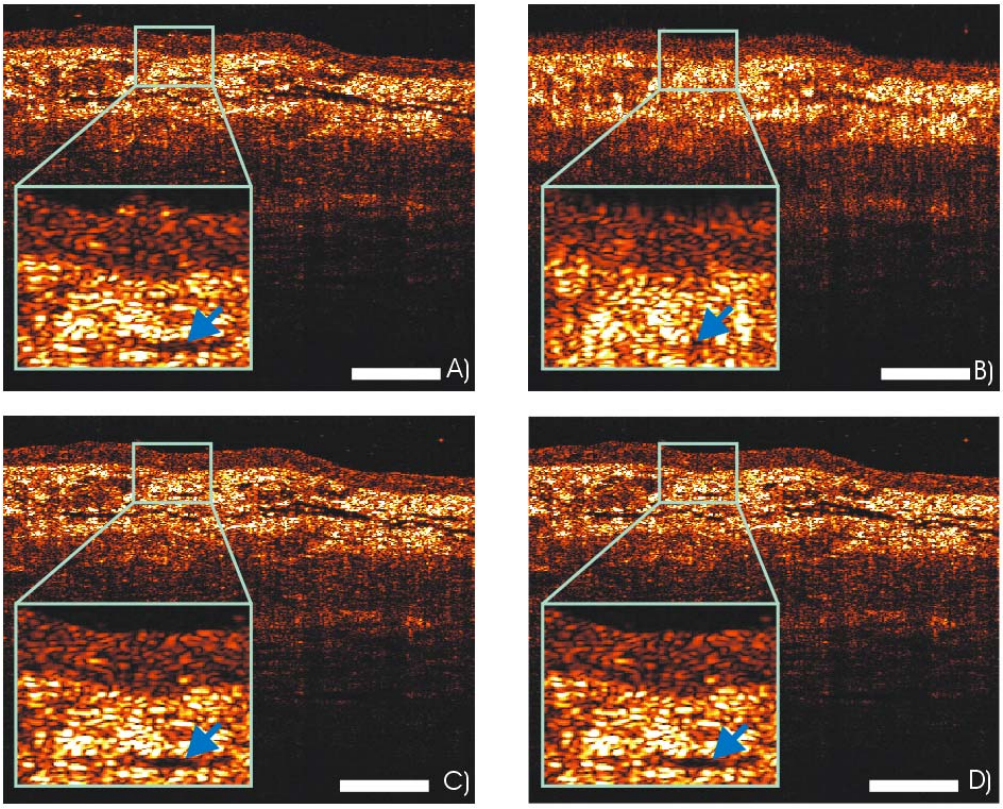

Fig. 2.8 2D SDuOCT images of a rat bladder. a) GDD balanced by dispersive prism pairs, b) extra GDD induced by additional 2mm thick glass, c) GDD compensated by phase linearization, and d) further correction of tissue GDD. Scale bar: 100μm.

It's noteworthy that as the method is based on phase information processing, accurate phase measurement is crucial. Theoretically, complete GDD compensation

should always be achievable; however, an overwhelming GDD might introduce dramatic phase error over the spectrum that may compromise the accuracy of phase error correction in its analytic signal. To demonstrate this, Fig. 2.9 presented groups of SDuOCT images acquired from another fixed bladder sample under severe dispersion conditions (5mm and 10mm thick BK7 inserted in sample arm respectively). Although the method effectively recovered micro-structures with substantially enhanced axial resolution and contrast, the image quality started to compromise comparing to the one with dispersion balanced. Therefore, a coarse GDD match by either RSOD or a pair of dispersive wedge prisms is suggested to ensure complete and accurate compensation of the numerical method. Similarly, an appropriate modulation frequency of the spectral interferogram (k=2z) used for spectral linearization and GDD-induced phase measurement is critical, which can be implemented by adjusting the separation of the air-gap glass chamber or the pathlength mismatch between the sample and reference arms. The most appropriate pathlength mismatch (i.e., modulation frequency) for this method is a compromise between the accuracy of phase measurement and the spectral resolution of the spectral radar imager. Nevertheless, we found 10-20 sampling points within each modulating cycle provided the best results for the setup used in this study.

In summary, the numerical method presented above is able to compensate the unbalanced dispersion between the sample and reference arms of SDOCT system. The principle of this method is to unwrap the phase distortion induced by spectral linearization and GDD using Hilbert transform, thus allowing for accurate and instantaneous dispersion-free spectral calibration and GDD compensation.

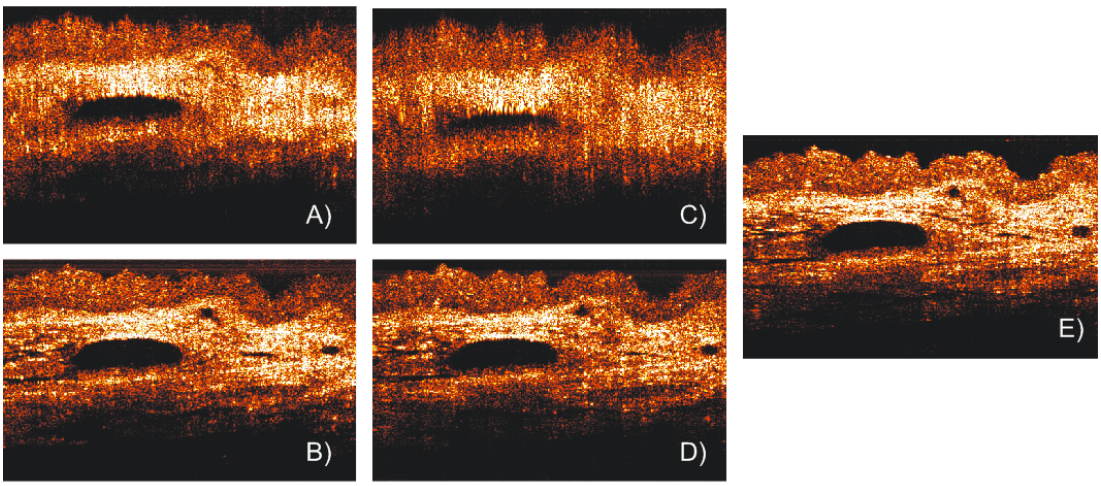

Fig. 2.9 SDuOCT images of rat bladder under different dispersion conditions. a) 5mm BK7 glass inserted in sample arm, b) GDD in a) was compensated by phase linearization; c) 10mm BK7 glass inserted in sample arm, d) GDD in c) was compensated by phase linearization; and E) dispersion balanced.

Chapter 3 **Time lapse ultrahigh resolution SDOCT**

Confocal microscopy (including optical coherence microscopy, i.e., OCM) and multiphoton microscopy permit sub-cellular imaging of superficial biological tissue such as skin and oral and cervical epithelia; however, these techniques use a high NA objective and require focal tracking to provide sub-cellular images at different depths, thus endoscopic adoption for *in vivo* diagnosis may pose a technical challenge. On the contrary, OCT is a coherence-gated technique that enables sub-10μm cross-sectional imaging of biological tissue. As discussed in chapter I, the axial resolution of OCT is defined by the source coherence length $L_c \approx 0.44\ \lambda^2/\Delta\lambda$ (λ, $\Delta\lambda$: central wavelength, spectral bandwidth), ultrahigh-resolution OCT, i.e., uOCT with L_c<1-2μm is possible by employing a broadband source and sub-cellular imaging of translucent tissue, e.g., xenopus laevis has been reported[12-13], However, sub-cellular uOCT imaging of scattering mammalian tissue (e.g., epithelium) remained unsolved, preventing this promising technique to render optical biopsy for clinical diagnosis. Interestingly, it was recently demonstrated that time-domain TL-uOCT, taking advantage of cellular micro motion in living tissue for effective speckle noise reduction, was able to uncover the seemingly impossible sub-cellular details (i.e., nuclei) in bladder epithelium using a low-NA commercial achromatic lens (f10mm/NA0.25)[15]. However, time domain TL-uOCT works for a controllable ex vivo studies, it suffers from low frame rate, thus, the technique bulky motion during in vivo study prevent this technique from being

effectively used. Therefore, we explored the possibility of using spectral-domain TL-uOCT to further improve image contrast and resolution for uncovering sub-cellular details with higher speed and provide new experimental results to examine the utility of this new technique for epithelial cancer grading.

3.1 Method

The SDuOCT system built in chapter 2 was slightly changed as illustrated in Fig. 3.1 to perform TL-uOCT sub-cellular imaging for bladder. In the reference arm, a grating-lens optical delay (RSOD, d^{-1}=400/mm, f=80mm) for matching the pathlength and dispersion between the two arms of the Michelson interferometer. Optimizing L_c of uOCT was achieved by spectral reshaping using RSOD in the reference arm and fiberoptic polarization controllers (FPC) to maximize the bandwidth of the modulation cross-spectrum (e.g., $\Delta\lambda \geq 155$nm); this procedure was found much easier to implement than in previously reported time-domain uOCT[15]. Mismatch of dispersion between the two arms was coarsely adjusted by RSOD, wedge prisms and FPC (for polarization-mode dispersion) and then fully compensated by a simple numerical method[50], which ensured an axial resolution approaching the transform limit, i.e., L_c=2.3μm or 1.7μm in bladder tissue (refractive index $n \approx 1.37$ is assumed). In addition, a lens group composed of two f=160mm lens and one meniscus lens was built and optimized by ZEMAX modeling as a better substitute of the single f=80mm achromate in the spectral radar, the simulation results was plotted on the right panel (b), showing optimized modulation transfer function (MTF), implying a better spectral resolution.

TL-uOCT, based on time-lapse frame averaging of dynamic cellular backscattering has been shown to effectively reduce speckle noise and uncover sub-cellular details in living epithelium[15]. Spectral-domain uOCT, owing to its improved image sensitivity and frame rate, can further enhance time-lapse phase scrambling for speckle removal and thus sub-cellular delineation. The detected TL-uOCT signal can be simplified by ensemble averaging of snapshots of uOCT signal $I_{uOCT}(L_r)$,

$$I_{TL-uOCT}(L_r) = \sum_\tau I_{uOCT}(L_r) / N_\tau = (1/N_\tau) \sum_\tau 2 I_r^{1/2} \sum_i E^b(L_{s,i}) e^{-4(L_{s,i}-L_r)^2/L_c^2} \cos\left[k(L_{s,i}-L_r)\right] \qquad (5.1)$$

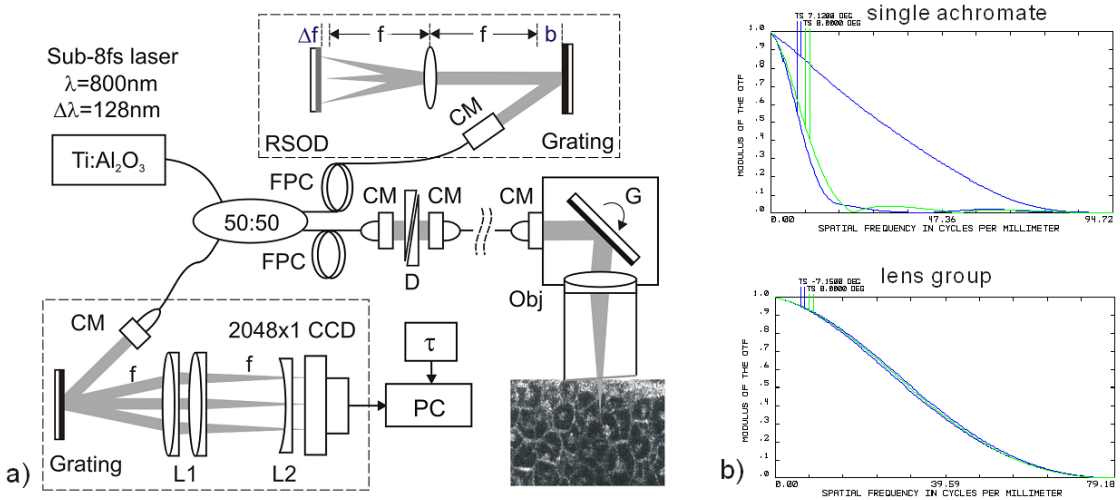

Fig. 3.1 A schematic of spectral-domain TL-uOCT. a): CM: fiberoptic collimator, FPC: fiber polarization controller; D: BK7 wedge prism pair and RSOD: grating-lens-based rapid optical delay for dispersion compensation; G: servo mirror; Obj: achromatic lens (f10mm/NA0.25); τ: delay trigger for TL-uOCT; L1, L2: achromatic lens group for field correction. Panel b): a comparison of the MTF between single achromate and lens group, showing an obvious improvement.

where N_τ is the number of τ-delayed averaging. $E^b(L_{s,i})$ is the backscattering from an intracellular organelle at a pathlength of $L_{s,i}=L_{s0}+\Delta L_{s,i}$ to analyze the effects of two types of motion on speckle dynamics. The motion of L_{s0} (origin, e.g., center of a nucleus) pertains to translation of cell matrix (tissue) which can be compensated by image

registration and might otherwise blur the τ-lapse averaged image. $\Delta L_{s,i}(t)$ is attributed to intracellular relative motion of living cells which is essential to TL-uOCT. For a snapshot, $\Delta L_{s,i}$ is stationary and the summation of all backscattering $E^b(L_{s0}+\Delta L_{s,i})$ constitutes a speckle pattern $I_{uOCT}(L_r)$. However, intracellular motion over time τ scrambles the phase $k\Delta L_{s,i}(\tau)$, thus time-lapse averaging $\Sigma_\tau I_{uOCT}(L_r)$ can minimize the speckle noise and accordingly uncover sub-cellular details (e.g., nucleus). It is noteworthy that L_{s0} may not be completely compensated by image registration (e.g., moving out of focus or image plane); therefore, a proper time lapse τ (e.g., τ≈0.1-0.7s) is a compromise between image blurring and sufficient phase scrambling for effective speckle noise reduction.

3.2 Results

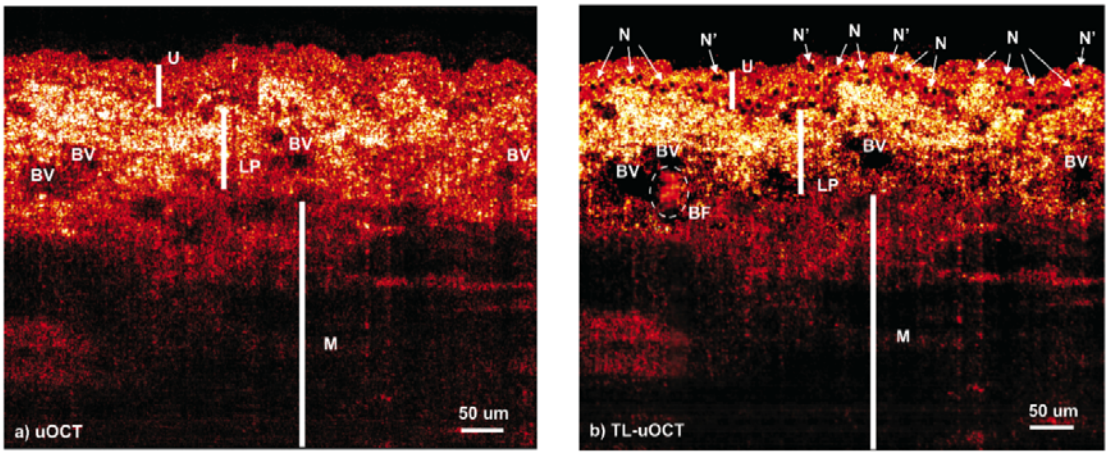

Fig. 3.2 2D uOCT of a living rat bladder *ex vivo*. a): A snap shot, b): TL-uOCT image (τ≈0.15s). U: urothelium, LP: laminar propria, M: muscularis, BV: bladder vessel, BF: residual blood flow (blurred by phase averaging). N: nuclei (D_N≈6.9μm); N': umbrellal cell nuclei ($D_{N'}$≈13μm).

Fig. 3.2 compares a snapshot of uOCT image (a) of a fresh rat bladder acquired at 50fps showing no resolvable cellular morphology due to speckle noise and a TL-uOCT

image (b) that uncovers sub-cellular details, e.g., the nuclei N (D_N=6.9±0.5μm) of rat urothelium (τ≈0.15s). Compared with time-domain TL-uOCT, both image the contrast and resolution for nuclear delineation is markedly enhanced and the effective imaging depth is increased (e.g., >500μm) to the upper muscularis (M) of the bladder wall without focal tracking. Fig. 3.3 further demonstrates the 3-D sub-cellular imaging capability of TLuOCT owing to the enhanced temporal resolution of SDuOCT. Ten slices of 2-D SD uOCT were acquired each time and were repeated 10 times for time-lapse frame averaging (N_t≈10, τ≈0.2 s).

To further examine the utility of this technique in the diagnosis and grading of epithelial cancers, a transgenic mouse model was used to provide orthotropic bladder cancers. Fig. 3.4 compares the results of TL-uOCT and the corresponding histology. For normal mouse bladder (a), TL-uOCT was able to resolve the nuclei of the urothelium (U) and delineate the underlying bladder morphology (e.g., lamina propria LP, muscularis M) without focal tracking. The nuclear size measured by TL-uOCT (DN=6.7±1.1μm) well matched that of histology (DN=6.0±0.8μm). Compared with normal bladder, structural heterogeneity in the cancerous lesion (b) was markedly increased resulting in reduced OCT imaging depth, consistent with our clinical observations using endoscopic OCT. More importantly, TL-uOCT was able to track the increase of the nuclear size to DN"=(12.9±1.3)μm in the bladder tumor; this measurement based on the 10 sampled nuclei (N1"–N10") closely matched the histological counterpart of DN"=(11.7±0.9)μm, thus allowing us to diagnose the tumor as a high-grade urothelial cancer or transitional cell carcinoma.

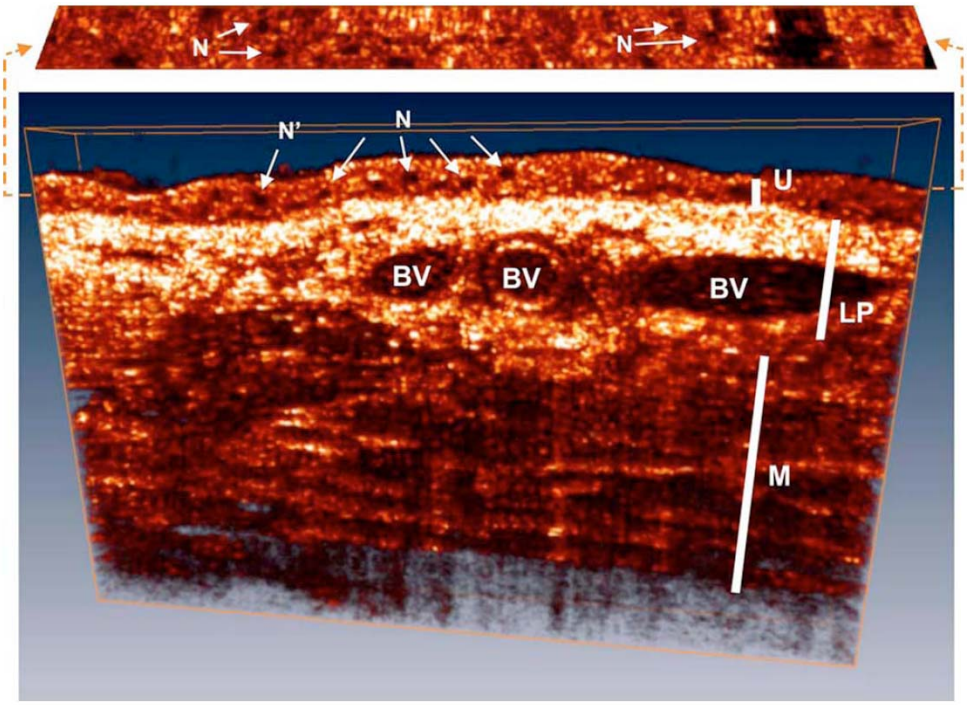

Fig. 3.3 Three-dimensional TL-uOCT of a fresh rat bladder *ex vivo*. $N_\tau \approx 10$, $\tau \approx 0.2$s. 3-D image size: $500 \times 265 \times 40 \mu m^3$ (40 slices). The upper panel is the en face image within the urothelium as indicated by two dashed lines. N: nuclei, $D_N = 7.4 \pm 0.8 \mu m$; N': umbrella-cell nuclei, $D_N \approx 11$ μm.

3.3 Conclusion

In summary, we present spectral-domain TL-uOCT technique to further enhance sub-cellular imaging of epithelial tissue. The key is to enhance local cellular-motion-induced phase scrambling while minimizing global motion (translation for shift), e.g., by image registration. Apparently, the higher detection SNR and imaging rate (temporal resolution) of the spectral-domain approach enables more effective phase scrambling for speckle reduction and thus sub-cellular delineation. Results of animal cancer model study confirmed that TL-uOCT measurements of urothelial nuclei closely matched those of the corresponding histology. More importantly this technique was able to track the nuclear enlargement in cancerous lesions, thus demonstrating the potential for direct epithelial

cancer grading. It is important to note that as TL-uOCT uses a low-NA achromatic lens (f10mm/NA0.25), it enables imaging of sub-cellular details in the epithelium and the underlying morphology of bladder wall over 0.5mm of depths without focal tracking, thus potentially highly suitable for endoscopic optical biopsy of carcinoma *in situ* where grading of cancer is crucial. Development and test of microelectromechanical systems (MEMS) based endoscopic TL-uOCT is being conducted to transform current hand-held device to a rigid endoscopic setting for *in vivo* sub-cellular imaging of bladder cancer.

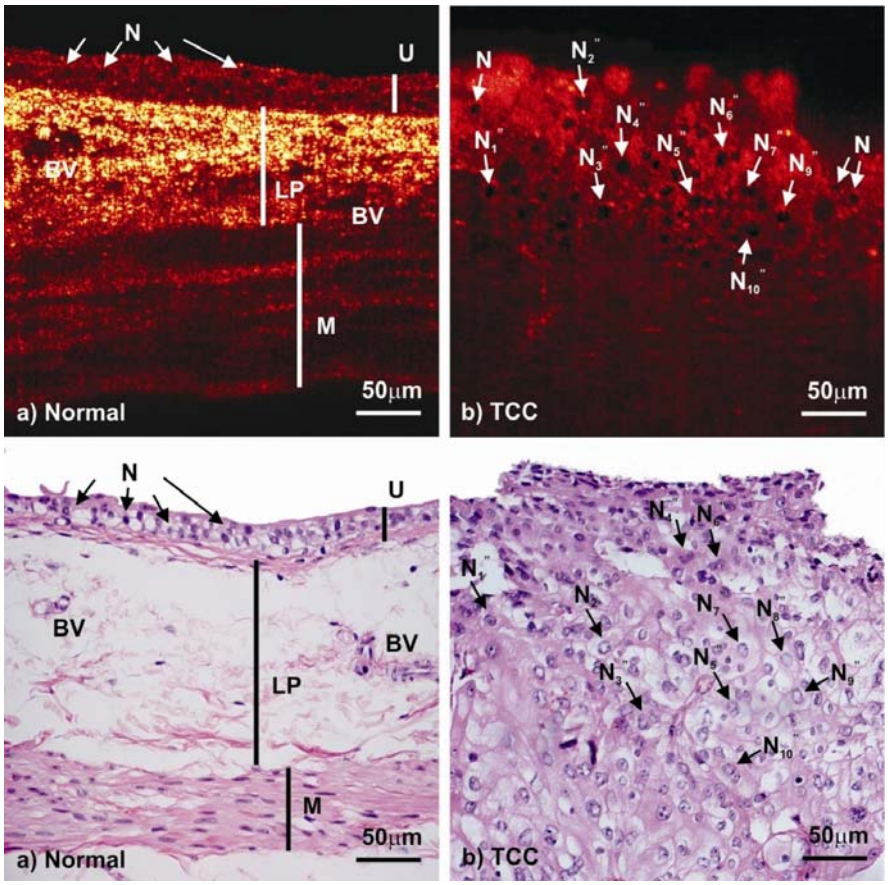

Fig. 3.4 Subcellular TL-uOCT of fresh mouse bladders *ex vivo* compared with the corresponding histology. (a) Normal bladder (N_τ=4, τ≈0.32 s); (b) transitional cell carcinoma or TCC (N_τ=4, τ≈0.4 s). Nuclear sizes measured by TL-OCT/histology were (a) D_N≈6.7±1.1μm/6.0±0.8μm for normal urothelium, (b) D_N≈12.9±1.3μm/11.7±0.9μm for high-grade (G3 TCC).

Chapter 4 Combining SDOCT and ultrasound for enhanced bladder cancer diagnosis

Bladder cancer is one of the most common cancers and leading cause of cancer death in the US[51]. Clinical statistics reveal that most bladder cancers are superficial carcinomas that originate within the thin basal cell layers (20-200μm) of the bladder epithelium or urothelium. These are usually curable if detected early (e.g., prior to invasion to the underlying muscularis) and treated appropriately; therefore, early diagnosis of TCC is of great clinical significance to the therapeutic benefits of bladder cancer patients. OCT has found potential applications in this field and has been developed for bladder cancer diagnosis in the lab since 1998. While clinical study using MEMS endoscopic OCT[52] shows drastically enhanced diagnosis of bladder cancers, OCT may not be able to provide sufficient imaging depth to stage bladder tumor invasion beyond stage T1 (invaded into lamina propria) or higher because of increased heterogeneity and blood-induced light attenuation within cancerous lesions,

Parallel with OCT, which detects the backscattering of light wave from the bladder wall, ultrasound imaging evaluation of the bladder can be performed noninvasively and quickly by detecting the backscattering of ultrasonic wave. Because of resolution limitations of trans-abdominal ultrasound imaging, the identification of morphological features pertinent to bladder cancers and progression has shown limited success for noninvasive detection in the clinic except for gross, outgrowing bladder

tumors[53]. Transurethral ultrasound imaging has also been used in assessment of bladder tumor, but is limited to the detection of large papillary tumors possibly due to insufficient resolution[54]. Recently, high frequency ultrasound (HFUS) imaging has been applied for *in vivo* diagnosis and assessment of a variety of epithelial cancers[55-57]. Because of drastically improved resolution (e.g., ~40μm for 40MHz ultrasound), the delineation of some anatomic architectures such as the lamina propria, the muscularis, and the fatty layer of the bladder wall is permitted (under pseudo-color display). This may show the promise of HFUS as a high-resolution imaging method for diagnosis and staging of bladder cancers. Although the resolution of HFUS is 5-10 times lower than OCT, the penetration of HFUS can be extended from 1-3mm for OCT to 5-10mm, which is potentially very useful for the staging of bladder cancers. The larger field of view (FOV) of ultrasound is also an important advantage to image the entire bladder which has a fairly large surface area. Furthermore, recent technological advances in both OCT and HFUS developments have permitted their integration into endoscopes or catheters for high-resolution transurethral imaging diagnosis. Here we propose the comparative study between 1.3μm SDOCT and 40MHz HFUS on bladder tissue imaging *ex vivo* to assess the utility and potential limitations of these two imaging modalities in the diagnosis and staging of bladder cancers, based on a rat bladder carcinogenesis model.

4.1 Methods

4.1.1 Animal cancer model

A standard rat bladder cancer model[58] was employed in which transitional cell

carcinoma (TCC) was induced by intravesical instillation of AY-27 cells into the bladders of 39 female Fischer 344 rats. AY-27 cells, obtained from Dr. Selman's Lab at Ohio Medical College, were a cultured rat bladder TCC cell line which was induced chemically from *N*-(4-[5-nitro- 2-furyl]-2-thiazolyl) formamide. The AY-27 cells from freezing stock were rapidly thawed in water bath at 38°C and grown in cell culture medium RPMI-1640 supplemented with 10% fetal calf serum and 2mM L-glutamine, incubated at 37°C with humidified 5%-CO_2 and 95% air flow for cellular accumulation. After 3-4 days the sub confluent AY-27 cells were split and seeded onto more culture plates until sufficient cellular accumulation was reached. Then the confluent AY-27 cells were detached from the plates by adding 0.1% trypsin, rinsed with PBS, centrifuged, and counted. The cells were re-suspended at a concentration of 3×10^6/ml in growth medium and maintained in a 37°C water bath; based on body weight (150g/each), 0.15ml of this cell suspension was to be instilled intravesically to yield ~4.5×10^5 cells per rat bladder. The rats were anesthetized using inhalational 5% isoflurane for induction and 1-2.5% for maintenance, and maintained supinely on euthermic blanket. A xylocaine-coated sterile Tom Cat catheter was gently guided through the urethra and into the bladder of the rat to drain the urine prior to instillation. To facilitate tumor seeding, 0.15ml of 0.1mol/L HCl was instilled into the bladder for 15s to mildly disrupt the urothelium and then neutralized with 0.15ml 0.1mol/L KOH for 15s. The bladder was further drained and flushed 2-3 times with sterile PBS until pH≈7.4. Subsequently, 0.15ml of either 4.5×10^5 AY-27 cell suspension or sterile PBS (control) was instilled into the rat bladder and maintained for 1 hr, during which the rat was turned 90° every 15 minutes to expose the entire bladder to the instills evenly. After 1hr, the catheter was removed and anesthesia was curtailed to

allow the animal to void in cage.

Fig. 4.1 In vivo trans-abdominal HFUS imaging. A ~1mm tumor is highlighted by a circle in a rat bladder on day 21 post AY27 cell instillation

Studies indicated that TCCs routinely developed in rat bladders roughly between day 12 and 50[58]; therefore, *ex vivo* imaging studies were begun during day 10-30 to track daily the changes induced by tumorigenesis induced by AY-27 cell induction. However, it was found in our previous experiments that the TCC growth induced by this cancer model was not uniform; therefore, we performed *in vivo* trans-abdominal HFUS twice weekly after day 10 to track the onset of large TCCs, allowing us to effectively avoid papillary outburst and to determine the proper time course (i.e., from early to high-grade TCC) for final *ex vivo* study. For instance, Fig. 4.1 shows an in *vivo* HFUS image of a ~Φ1mm tumor in the bladder on day 21. Prior to *ex vivo* imaging evaluation (endpoint), both control and treated rats (blinded) were euthanized using anesthetic overdose and the intact bladder was removed by a midline laparotomy incision, opened from the urethra to the dome and mounted uniformly on a ring holder placed in a modified Ringer's buffer solution (37^{o}C, pH7.4) to undergo multiple OCT and HFUS scans *ex vivo*. Hematoxylin and eosin (H&E) stained histology was performed on the

sections precisely marked during OCT and HFUS scans to confirm the identifications of the image features made during imaging studies.

4.1.2 OCT and HFUS Imaging

The ~1310nm SDOCT system was modified here with HFUS to perform the imaging as illustrated in Fig. 4.2. In addition to the original setup, a 532nm green light was coupled into fiber to visually guide the scan. The HFUS imaging was performed with an ultrasonic micro-imaging system (Vevo 770, Visualsonics Inc., Toronto, Canada) using a single-element, 40MHz f/2 probe (RMV 704) with a focal length of f_{US}=6mm. 2D cross-sectional ultrasound B-mode (USB) imaging can be performed in real time (34fps). The axial and lateral resolutions of the HFUS transducer were $\Delta z_{HFUS}\approx 40\mu m$ (in soft tissue) and $\Delta r_{HFUS}\approx 80\mu m$, respectively. And the field of view per HFUS scan was $FOV_{HFUS}\approx 10mm\times 10mm$ (lateral/axial directions). For ex vivo HFUS imaging performed in this study, the bladder specimens were immersed in PBS which also served as the ultrasonic coupling media between the HFUS transducer and the bladder tissue under examination. Images were acquired with the region of the bladder specimens (e.g., mostly the urothelium or TCCs) centered at the focus. HFUS images were reviewed independently to ensure a double-blind study. Sensitivity and specificity were calculated for both OCT and HFUS, in which histology served as the objective standard. The results of OCT and HFUS were classified as normal, inflammation, or TCC, based on the backscattering and echo characteristics that differentiated rat bladder morphology. More specifically, inflammation was diagnosed by OCT and in some cases by HFUS based on decreased backscattering or echo in the LP; TCC was diagnosed by OCT as urothelial

thickening with enhanced urothelial heterogeneity or backscattering with drastically reduced penetration, and by HFUS as increased mass (e.g., outgrown lesions). Similarly, necrotic lesion was detected by OCT as extremely high backscattering with missing underlying structures, but exhibited low echo in HFUS. Normal urothelium and inflammatory lesions were considered negative (-) whereas TCC was considered positive (+). Chi-square analysis was performed to compare the sensitivity and specificity of HFUS and SDOCT with $p < 0.05$ considered statistically significant.

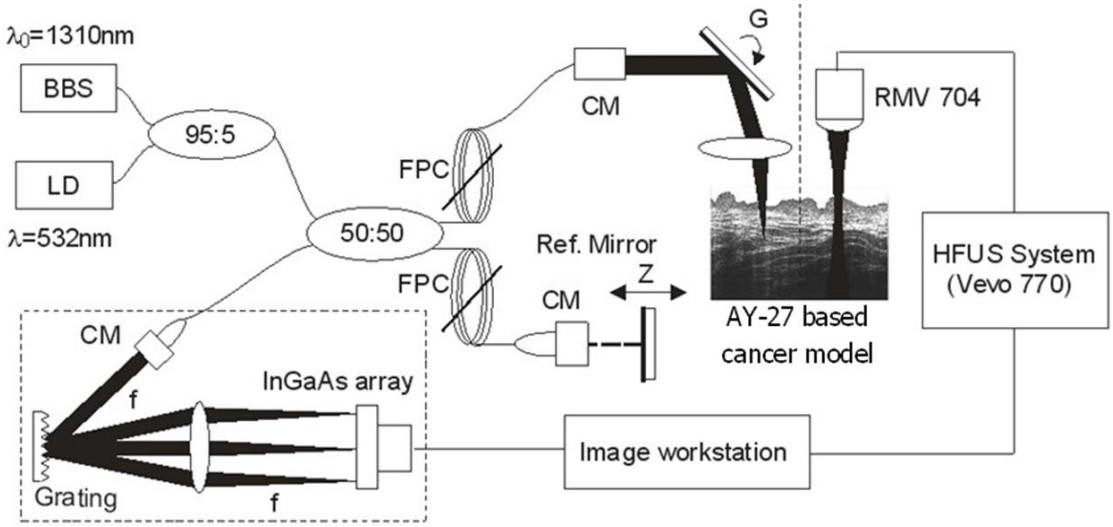

Fig. 4.2 Schematic of the SDOCT and HFUS combined system. BBS: broadband source (λ_0=1320nm, $\Delta\lambda$(FWHM)=90nm, P=18mW); LD: aiming laser diode (λ=532nm); CM: fiberoptic collimator; FPC: fiber polarization controller; SM: scanning mirror; RM: reference mirror

4.2 Results

Both OCT and HFUS detect bladder morphological features based on their backscattering differences optically or ultrasonically. Previous studies indicated that because of high resolution (e.g., ~10μm), OCT delineated the urothelium (U) as a low scattering thin layer, the lamina propria (LP) as of high scattering, the muscularis (M) as of high scattering but showing large bifurcated structures, and in some cases the attached

fatty layer (F) as barely resolved larger fat cells in a normal rat bladder. OCT was able to differentiate urothelial denudation, LP edema, urothelial hyperplasia and TCC of rat bladder based on urothelial thickening and backscattering enhancement; however, staging of TCC was limited to T1 (not for major papillary lesions) because of limited imaging depth of OCT within the cancerous lesions which often induced drastic OCT signal drop.

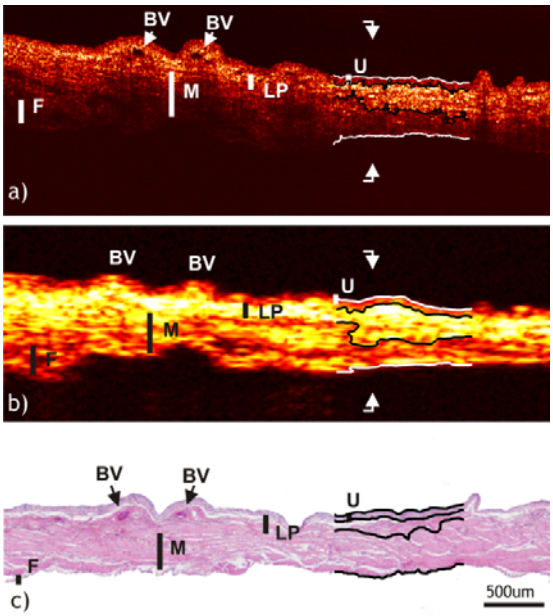

Fig. 4.3 Normal rat bladder imaged. a)OCT, b)HFUS, and c)histology. OCT delineated morphological details such as the low scattering urothelium (U, ~51±5μm), the high-scattering lamina propria (LP, ~119μm), the muscularis (M, ~296μm), and attached fat (F, ~185μm), as well as two blood vessels (BV) in the LP. The traces in images (a, b) were the interfaces of the segmented layers, e.g., U, LP and M using image processing methods including de-speckling, thresholding and edge detection. Traces in image (c) were pathologist's manual segmentation.

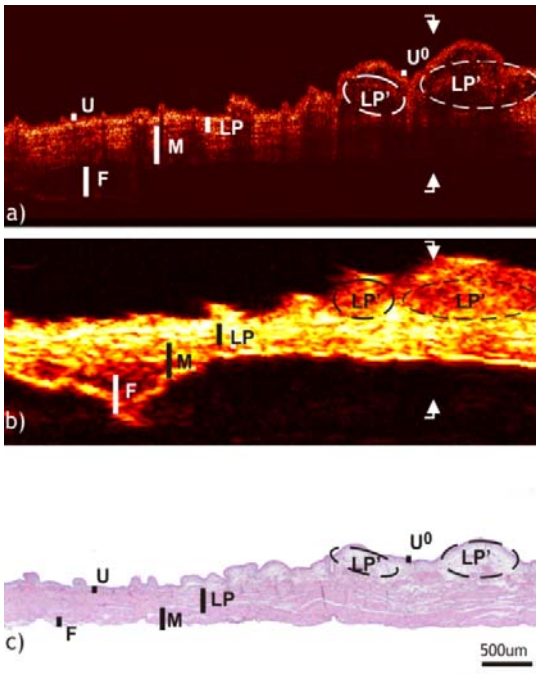

Fig. 4.4 Rat bladder undergoing inflammatory reaction. OCT (a) was able to image the morphological details of the bladder and detect two inflammatory infiltrates or edemas (LP') in the lamina propria as confirmed by histology (c). HFUS (b) barely resolved the difference between LP and M. Although two lesions (LP') were detected as echo low, the diagnosis was unspecific because it was unable to differentiate the thin urothelium U^0.

To compare with HFUS, a set of 3 cross-sectional images, i.e., OCT, HFUS, and

histology are presented for each lesion. All the originally 12-bit grayscale cross-sectional images (6mm lateral × 2.1mm vertical in bladder tissue) are displayed in pseudo color with no further post-image processing. All the originally 8-bit grayscale HFUS images are displayed in pseudo color to enhance the visibility for different layers of rat bladder and are cropped to match the size of the corresponding OCT scans. Fig. 4.3 shows the results of a normal rat balder imaged by OCT (a) and HFUS (b) in comparison with histology (c). OCT delineated morphological details such as the low scattering urothelium (51±5μm), the high-scattering lamina propria (~119μm), the muscularis (~296μm) and attached fat (~166μm), as well as the two blood vessels in the LP. The results compared favorably to the corresponding histology (U: 52±4μm, LP: ~113μm, M: ~322μm) except that the attached fatty layer (F: ~10μm) shrunk substantially during tissue fixation. Surprisingly, HFUS (b) was able to resolve U (66±11μm) as low ultrasonic scattering or low echo and the underlying bladder layers (LP: ~123μm, M: ~333μm, F: ~222μm), similar to those of OCT identifications (e.g., LP: echo high, M and F: echo lower). As can be seen, the speckle patterns in the HFUS image are much larger than those in OCT image, especially in the transverse direction. As a result, the two small blood vessels (BVs) were not identified by HFUS imaging. Because of inherent speckle noise in OCT and HFUS images, accurate tissue differentiation (e.g., U, LP, and M) by computer image segmentation remains challenging, in particular in areas such as lesions and folds that exhibit shadowing artifacts induced by either irregular surface or decrease in LP scattering. Nevertheless, computer segmentation in flat and normal areas of the rat bladder can be implemented, as shown Fig. 4.3. The following image processing methods were applied to segment bladder layers (U, LP and M) in OCT (a) and HFUS (b) images:

1) both were converted to 8-bit grayscale images; 2) low-pass Gaussian filtering with radius of 4 pixels was applied to minimize speckle noise; 3) edge detection to segment different bladder layers. To do this, the mean grayscale value with standard deviation $M\pm\sigma$ of a small 5×50-pixel RIO within a layer such as U or M was sampled (e.g., M_U=74±15 M_M=50±10 for U and M layers), and then the regions were extended to the surrounding pixels to form the contours (i.e., edge of the layer) using the thresholding values of $M\pm2\sigma$ (e.g., M_U=74±30, M_M=50±20) where 2σ is the tolerance range which takes into account of speckle-induced intensity fluctuations. Due to residual speckle noise or shadowing artifacts (e.g., surface folds), often a few contours were formed so that they had to be manually connected to form the entire layer. The histological image (c) was manually segmented based on pathologist's identification. It is noteworthy that further attempts of segmentation to the left region in image (a) and to the right side in both images (a) and (b) failed due to shadowing artifacts induced by the BVs and the folds, respectively.

Fig. 4.4-Fig. 4.7 represent 4 groups of *ex vivo* images of rat bladders at different stages of tumorigenesis following AY-27 cell instillation. Like the MNU cancer model[25], the disease progression of this cancer model involves early acute chemical cystitis or injuries of the urothelium (e.g., acid wash during instillation), causing leakage of urine constituents or AY27 cells through disruptive bladder barriers which begins to a process of inflammatory reactions of the underlying LP and M layers and in turn causes fibrosis and urothelial malignancies (e.g., mostly due to AY27 cell growth). Therefore, the cancer model allows us to evaluate the potential of OCT and HFUS for visualizing the morphological alternations pertinent to the growth of bladder tumors including edema,

inflammation, ulceration, urothelial lesions and the subsequent TCC invasion. Fig. 4.4 shows the rat bladder undergoing acute inflammatory reaction. OCT (a) was able to image the morphological details (e.g., U, LP, M, and F) of the bladder and detect the underlying lesions as two inflammatory infiltrates or edemas (LP'), as confirmed by histology (c). HFUS (b) in this case barely resolved the difference between LP and M, but detected the two lesions (LP') as echo-low shadow. Because of swelling (LP'), this part of urothelium (U^0) above the lesions was considerably stretched thinner than the surrounding normal U. Unlike OCT that resolved it as a thin, low-scattering superficial layer (30~40μm), HFUS failed to identify the thinning urothelium. It must be noted that the ability to identify U^0 is critical; otherwise, the large echo-low lesions might be misdiagnosed as TCCs by HFUS, as will be discussed below.

Fig. 4.5 shows the results of a bladder containing two lesions. Based on enhanced urothelial backscattering ($V_{U"}/V_U \approx 1.3$) and decrease of OCT signal below the surface, OCT (a) diagnosed the lesion on the left as TCC (U"). However, because of steep slope, OCT failed to identify the attached urothelial hyperplasic lesion over the TCC as highlighted by the dashed circle. For the right lesion, OCT was able to diagnose it as minor hyperplasia (U') based on delineation of the low scattering, slightly thickened but uniform urothelium (83±10μm). Unlike the inflammatory lesions in Fig. 4.4, the submucosal edema (LP') was more severe with local vasodilatation as confirmed by histology (c), which led to missing underlying bladder structures in OCT image (a) as a result of enhanced blood-induced light attention [25]. In comparison, HFUS (b) was able to stage the invasion of U" as a T1 cancer (622±37μm) which OCT failed (indicated by dash line). However, as HFUS was unable to differentiate U' and LP', the right lesion

might be misdiagnosed as either an inflammatory lesion or a T1 TCC.

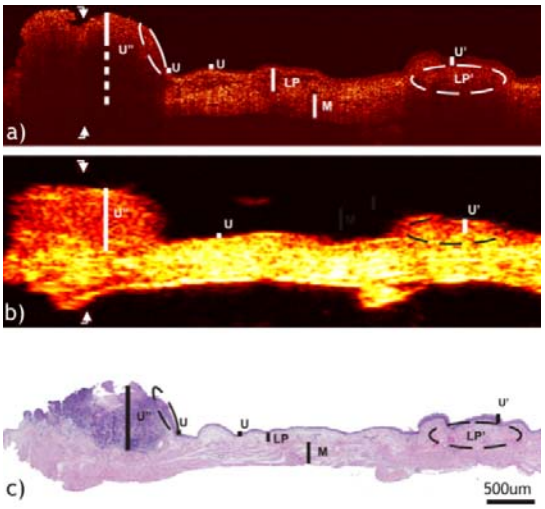

Fig. 4.5 Rat bladder with two lesions. OCT (a) diagnosed the left lesion as TCC (U") and the right lesion as minor hyperplasia (U'), but failed to identify the attached urothelial hyperplasia (dashed circle) and to stage U". HFUS (b) was able to stage the invasion of U" as a T1 cancer but was unable to diagnose the right lesion because it failed to identify U' and LP'

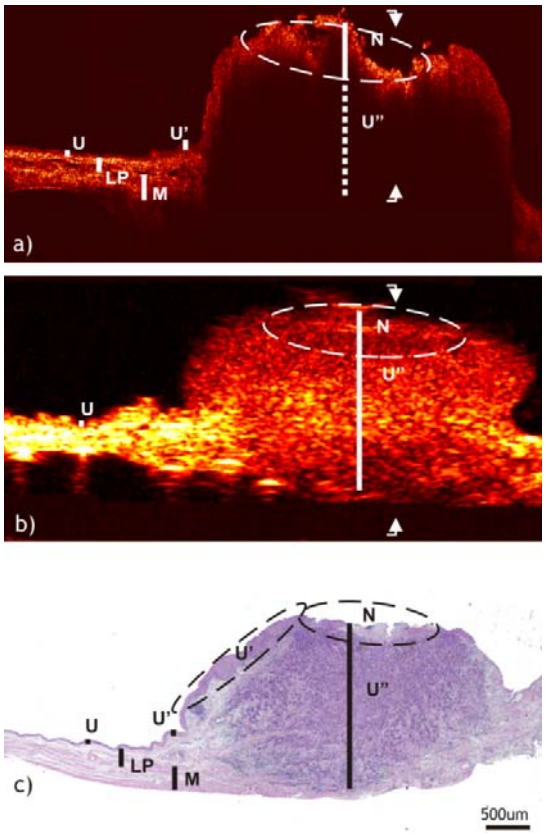

Fig. 4.6 Rat bladder with a large T2 tumor. OCT (a) was able to identify the boundary and the transition with a minor hyperplasia (U'), as well as the necrosis (N) above the large TCC (U"). Again, OCT failed to stage the tumor. HFUS (b) was able to stage it as T2

Fig. 4.6 shows the results of a large T2 cancer. Because of limited penetration, OCT (a) was unable to stage the TCC (U"), whereas HFUS (b) could stage it as T2. At the left boundary, OCT could identify the minor hyperplasia (U') which HFUS barely resolved. However, as indicated by the dashed circle, the large TCC (U") was encapsulated by the hyperplasic urothelium (U'), causing the lesion not to show enhanced backscattering ($V_{U"}$) except at the center where the necrotic tissue as indicated by the

dashed circle (N) exhibited increased scattering. On contrary, the necrotic lesion showed echo low in the HFUS image. Although this large TCC might be misdiagnosed by OCT as severe hyperplasia (i.e., urothelial thickening without backscattering enhancement), the abrupt decrease of OCT signal within the lesion should differentiate it from hyperplasia. Fig. 4.7 shows a more advanced high-grade T3 TCC. Similar to Fig. 4.6, the cancerous lesion was embedded under the urothelium as shown by histology (c). Therefore, no enhanced backscattering was observed in OCT image (a) except in the area of the large necrosis. As has been found in previous animal and clinical OCT studies, necrotic lesions tended to exhibit substantially enhanced backscattering ($>2.5V_U$). Again, HFUS (b) showed low echo in the necrotic lesion. However, possibly due to increased heterogeneity in the TCC (high grade) leading to increased ultrasonic scattering, the HFUS signal level dropped substantially along the depth of the lesion so that HFUS failed to stage the invasion of this T3 tumor. Interestingly, the urothelium adjacent to the large TCC was almost denuded ($U^0 \approx 19 \pm 2\mu m$) so that OCT barely detected the thin urothelium ($U^0 \approx 21 \pm 5\mu m$), but the HFUS measurement was overestimated ($U^0 \approx 65 \pm 10\mu m$) and appeared as normal. Both OCT and HFUS could identify the inflammatory lesion (LP') underneath the denuded urothelium (U^0).

A total of 56 spots (i.e., sites) were imaged from 39 bladders, among which 7 lesions were confirmed as TCCs by histology. Both OCT and HFUS were able to identify these large lesions as TCCs. However, HFUS falsely identified 32 lesions which were detected by OCT and histology as benign inflammatory lesions. According to the results on a per lesion basis, the sensitivity and specificity for OCT were 100% and 100%, respectively; whereas for HFUS, they were 100% and 61%, respectively.

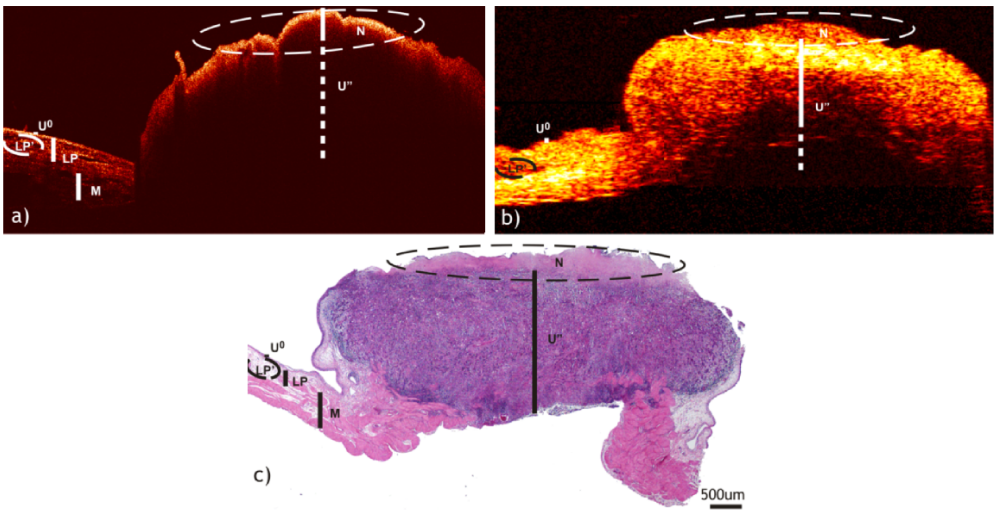

Fig. 4.7 Rat bladder with a high-grade T3 tumor. OCT was able to diagnose the lesion as TCC (U") and detect the superficial necrosis (N). HFUS (b) failed to stage the tumor because of insufficient imaging depth. In contrast to OCT, necrosis showed low echo in HFUS. Unlike the T2 TCC in Fig.7, the high-grade T3 TCC appeared echo high, possibly due to increased heterogeneity to enhance ultrasonic scattering.

4.3 Discussion and Conclusions

Because of resolution limitations of current medical imaging techniques (e.g., X-ray, MRI), white-light cystoscopic *en face* imaging or cystoscopy following urine cytology is presently the clinical standard for diagnosis of bladder cancers and the recurrence following transurethral resection of bladder tumors (TURBT). Unfortunately, cystoscopy lacks depth resolution; it may miss flat TCCs (e.g., carcinoma in situ) and often relies on random biopsy for conclusive diagnosis whose diagnosis depends on the selection of biopsied sites and results in insufficient diagnostic sensitivity and specificity, according to clinical statistics. OCT is a new enabling optical imaging technique that offers sub-10μm spatial resolution and superb signal-to-noise ratio. Our recent clinical study demonstrated that MEMS-based OCT cystoscopy has the potential to drastically enhance the sensitivity to 91% and specificity to 80% for noninvasive bladder cancer

diagnosis[52]. However, the study also suggested limited usage of OCT for staging the invasion of large bladder cancers to T1 or less. Therefore, a more effective staging technique is desirable.

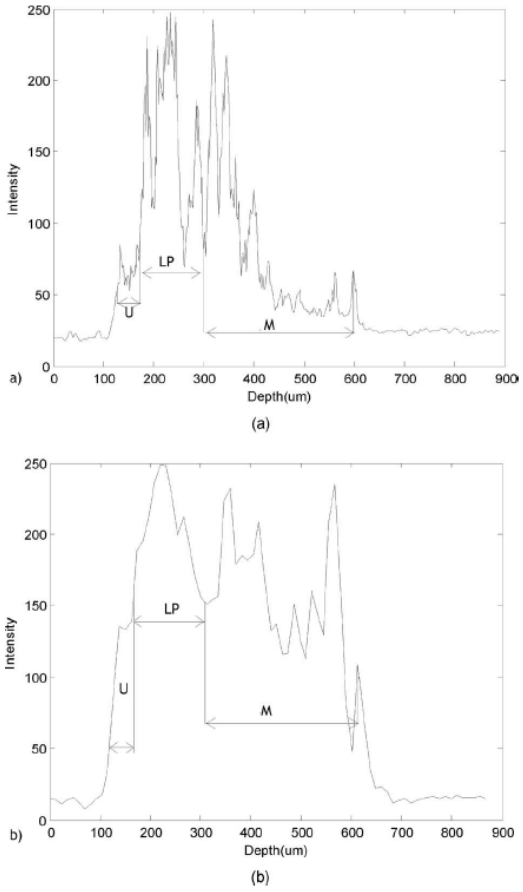

Fig. 4.8 A-scans on normal bladder. The lateral position is highlighted by a pair of arrows in Fig. 4.3. a)The OCT measurement of U≈50μm matched well with histological evaluation, whereas that of b)HFUS (U≈60μm) was a rough estimate

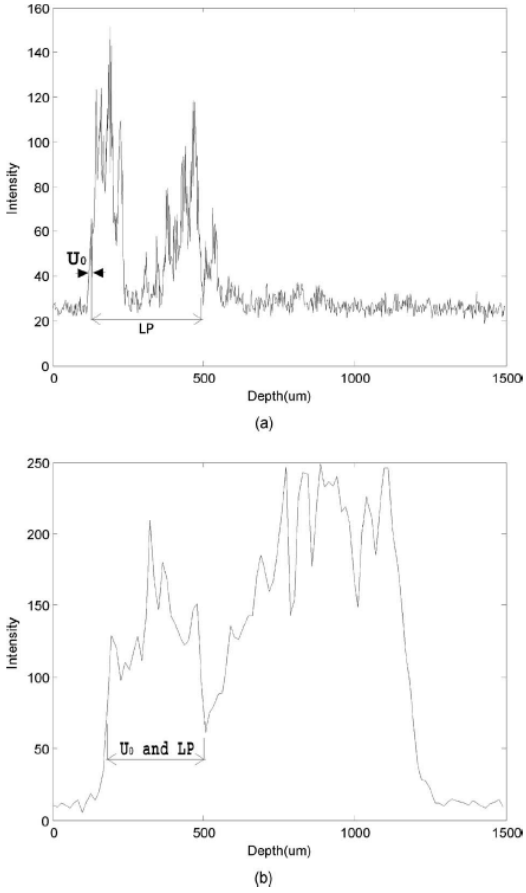

Fig. 4.9 A-scans across an inflammatory lesion. The lateral position is highlighted by arrows in Fig. 4.4. a)OCT identified the very thin urothelium (U^0≈18μm) which b)HFUS missed because both U^0 and the underlying lesion LP' exhibited echo low

In this study, we compare two promising high-resolution imaging modalities, i.e., OCT and HFUS, for imaging urinary bladders and for diagnosing and staging bladder cancers. The research methodology that confirmed the OCT and HFUS identifications

with the corresponding histology (i.e., gold standard for clinical diagnosis) allowed us to evaluate the potential of these two imaging techniques for future noninvasive clinical diagnosis of bladder cancers and their technical limitations. Moreover, the rat bladder cancer model by AY-27 cell instillation provided a platform to enable systematic imaging identifications of the morphological changes induced by bladder tumorigenesis such as edema, cystitis, hyperplasia, and urothelial carcinomas.

The results in Fig. 4.3 show that both OCT and HFUS were able to resolve the urothelium of a normal rat bladder as an echo-low thin layer. Fig. 4.8 further compares the A-scans between these two imaging techniques at a lateral position highlighted by arrows in images Fig. 4.3(a)-(b). Apparently, the OCT measurement of U≈51±5μm is accurate compared to the histological evaluation of U≈52±4μm whereas that of HFUS (U≈66±11μm) can only be a rough estimate, as a result that its axial resolution (Δz_{HFUS}≈40μm) is inferior to OCT (Δz_{OCT}≈8.9μm). Nevertheless, the ability to resolve urothelium is critical and may provide HFUS with the potential to diagnose urothelial cancers. Similar to Fig. 4.8, Fig. 4.9 compare the A-scans signal of OCT and HFUS over an inflammatory lesion at the lateral position highlighted by arrows in images Fig. 4.4(a)-(b). Based on the signal changes in Fig. 4.9, OCT can identify the benign urothelium, whereas HFUS fail to identify the interface between the urothelium (U) and the underlying lesion in the lamina propria (LP), both of which exhibit low echo. This will seriously limit the diagnostic value of HFUS for bladder cancer detection, because both benign lesions such as the inflammatory lesion (LP') in Fig. 4.4 and the hyperplasia (U') and LP edema (LP') in Fig. 4.5 and malignant lesions such as TCCs in Fig. 4.5 and Fig. 4.6 are echo low and therefore cannot be differentiated. However, despite the inability to

differentiate these lesions, HFUS can precisely stage the invasions of these two large TCCs in Fig. 4.5 and Fig. 4.6. Fig. 4.10 and Fig. 4.11 show the A-scans signal of OCT and HFUS over T1 and T2 tumor highlighted by arrows in images Fig. 4.5(a)-(b) and Fig. 4.6(a)-(b) respectively, which OCT imaging fails to stage. Therefore, these two techniques can be combined to take advantage of their individual characteristics for bladder imaging, i.e., OCT for diagnosis and HFUS for staging of bladder cancers. It should also be noted that in many cases OCT and HFUS show similar contrasts for bladder components. For instance, both techniques show low backscattering/echo for urothelium, muscularis, and fat and high scattering/echo for lamina propria. However, the image contrast of HFUS for bladder cancers may be different. For instance, the two TCCs in Fig. 4.5 and Fig. 4.6 appear as uniform and echo low, whereas the high-grade TCC in Fig. 4.7 appears as less homogeneous and echo high at the top of the cancer. This could be attributed to the increased heterogeneity in high-grade TCCs. Also, on contrary to OCT which drastically diminishes penetration, necrosis which often exists on top of large high-grade TCCs appears echo low and "transparent" (without substantive attenuation) in HFUS imaging.

In this study, all the 7 TCC lesions induced by AY-27 cancer model were diagnosed by both OCT and HFUS (100% sensitivity); however, these tumors were outgrown and thus likely identifiable by via surface appearance. While the specificity of OCT reached 100%, HFUS falsely identified 32 inflammatory lesions as TCCs, resulting in a reduced specificity of 61%, due to the fact that both TCCs and inflammatory lesions exhibited low echo so that HFUS failed to differentiate. With a 39% difference in specificity, Chi-test shows a significant enhancement of OCT over HFUS diagnoses.

However, it is noteworthy that only 7 TCCs were yielded out of 39 AY27 cell treated rats and all were all outgrown, the high diagnostic sensitivity/specificity may not necessarily reflect those of either clinical scenario or other animal TCC models (e.g., MNU or SV40-T transgenic mouse models). Results of our recent *in vivo* clinical study demonstrated both the potential and complexity endoscopic OCT for bladder cancer diagnosis.

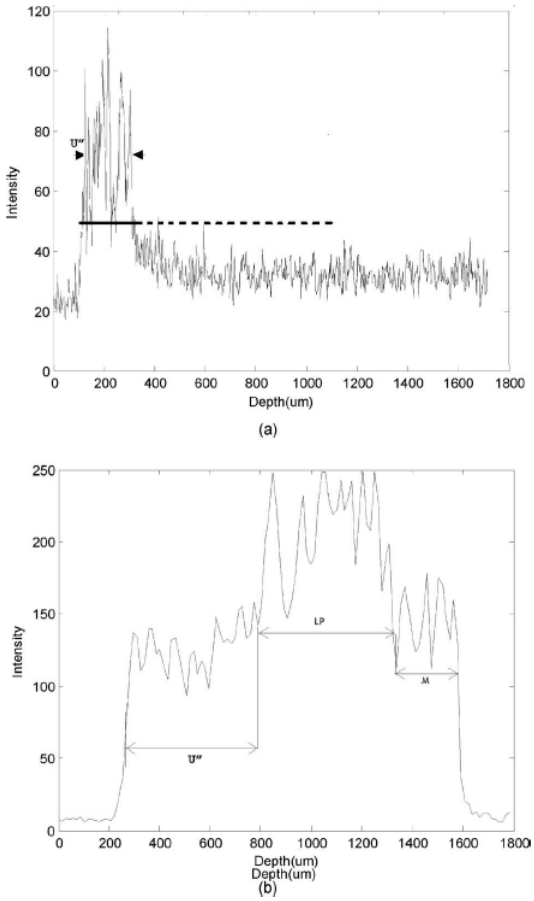

Fig. 4.10 A-scans across a T1 tumor. The Lateral position is highlighted by a pair of arrows in Fig. 4.5. a)OCT signal dropped to noise background within the first 200μm and thus failed the tumor invasion whereas b)HFUS measured the invasion to 540μm and staged it as T1 tumor.

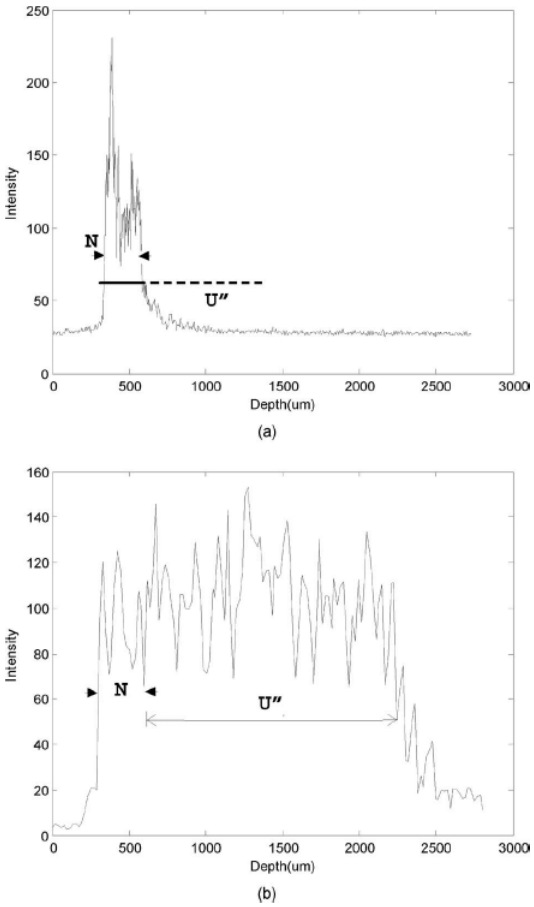

Fig. 4.11 A-scans across a T2 tumor . The lateral position is highlighted by a pair of arrows in Fig. 4.6. a)OCT detected necrosis (N) but failed to stage the tumor whereas b)HFUS measured the full thickness (2.1mm) of the tumor and staged it as T2.

In conclusion, despite that the image fidelity (both contrast and resolution) of

OCT is superior to HFUS, both techniques are able to delineate the morphological architectures of normal rat bladder and exhibit similar image contrasts in terms of high or low backscattering or echo. OCT is able to diagnose inflammatory lesions, hyperplasia, and TCC based on urothelial thickening and urothelial backscattering or heterogeneity enhancement; however, its staging of bladder cancer invasion is limited to T0-T1 due to limited penetration depth. In contrast, HFUS fails to differentiate some benign lesions and TCC, but it can stage the invasion of T2 TCC (to muscularis). Therefore, a multimodality approach combining OCT and HFUS may potentially enhance the diagnosis and staging of bladder cancers. In addition, since technological advances have permitted transurethral HFUS and endoscopic OCT, a cystoscopic approach combining these two image techniques may improve current urological examinations of bladder cancers and help to guide TURBT, in which both high-resolution imaging for diagnosis and deep penetration for tumor staging are desirable.

Chapter 5 SDOCT based Doppler flow meter with digital frequency ramping method

OCT based Doppler Flow meter, or Doppler OCT, is a new imaging approach that is derived from conventional OCT technique to detect dynamic flows at high resolution, thus allowing for a more specific functional imaging diagnosis. The principle of Doppler OCT is based on the extraction of the Doppler phase changes induced by flowing scatterers. High-speed Doppler OCT was first developed in time-domain OCT by subtracting the phase difference between two adjacent depth scans, i.e., A-scan based Doppler flow measurement [59-61]. This technique was largely simplified in FDOCT resulting in drastically improved imaging rate and signal-to-noise ratio (SNR) by virtue of fast Fourier transform (FFT) so that *in vivo* real-time 2D and 3D Doppler OCT can be permitted [62-65]. Despite its superior spatiotemporal resolutions for noninvasive subsurface flow imaging Doppler OCT has suffered a major drawback from excessive phase noise. Phase noise may originate inherently from dynamic multiple scattering, speckle noise, heterogeneity of biological tissue or the amplitude shot noise of the detected spectral interferometric fringes. It could also result from motion-induced artifacts of *in vivo* regime, in particular, in endoscopic Doppler OCT imaging, where unsteady hands often induce substantial phase noise or artifacts. Several approaches have been explored to enhance the SNR for flow detection [46, 66-71], among which optical angiography (OAG), based on B-scan phase modulation thresholding in FDOCT, has

been recently reported by Wang's group to effectively suppress phase noise and thus allow for 3D mapping of cerebral microvascular perfusion through intact mouse cranium at unprecedented sensitivity and resolution[69, 72]. In these OAG systems, a constant Doppler frequency shift v_0 was used to threshold the phase or frequency term in the transverse Hilbert transform to differentiate the dynamic flow signal from static or random, slow-moving noise background. A stable v_0 was generated by either linearly scanning the reference mirror with a PZT translator or by angularly actuating an off-center servo mirror in the sample arm of an FDOCT system [69, 73].

Based on the principle of B-scan phase modulation thresholding (Hilbert transform in the transverse direction), we further develop a solely numerical approach, i.e., digital frequency ramping method (DFRM), which employs computer generated numerical Doppler frequency to enhance flow detection sensitivity and resolution. As the need for hardware-based Doppler frequency shift implementation is circumvented, this new technique can be applied to conventional FDOCT, thus potentially allowing for 2D and even 3D optical angiography in real time. More importantly, by digitally ramping the Doppler frequency v_0 from low to high and from positive to negative, this technique enables quantitative flow imaging, which is crucial to a wide variety of physiological and functional imaging studies where quantitative blood flow monitoring is required. To examine the efficacy of DFRM for enhancing flow imaging, computer simulation and tissue phantom study were conducted for phase noise reduction and flow quantification. In addition, initial *in vivo* validation of this new technique was performed in our clinical bladder imaging studies using endoscopic FDOCT.

5.1 Methods

5.1.1 Digital frequency ramping method (DFRM)

As has been reported, the depth-resolved backscattering profile (i.e., A-scan) is encoded on the spectral interferogram at different modulation frequencies and can thus be reconstructed by inverse fast Fourier transform (iFFT) after spectral calibration to convert the measured spectrograph to k-space where $k=2\pi/\lambda$ [30, 49]. The interferometric signal with respect to spectral modulation at depth Δz within a biological tissue (i.e., 1/2 of the optical pathlength difference between the sample and reference arms) can be expressed as

$$I_i(k,\Delta z) = 2\sqrt{I_r I_{s,i}(\Delta z)}S(k)\cos\left[2k\Delta z + \phi + (\nu_s + \nu_f)\cdot i\tau\right],\ (i=1,\ 2,\ \ldots,\ N_x) \tag{5.1}$$

where I_r is the light intensity in the reference arm and $\sqrt{I_{s,i}(Dz)}$ is the backscattering amplitude from depth of Δz in the sample arm which constitutes the structural OCT image. $S(k)$ is the cross spectrum and ϕ is a random phase of the scattering biological tissue, i is the sequential A-scan index and N_x is the pixel number of the FDOCT image in the transverse direction, ν_s refer to the Doppler frequency shifts induced by the relative motion between the sample and reference arms (e.g., motions of the sample probe and of the living biological tissue, and system vibration) and ν_f refer to the shift caused by the local blood flows that to be detected from the biological tissue, τ is the duration between each A-scan.. The spectral amplitude term can be simplified to $A_i(k,Dz) = 2\sqrt{I_r I_{s,i}(Dz)}S(k)$. Conventional Doppler OCT that measures the phase difference, i.e., $(\nu_s+\nu_f)\tau$, by phase subtraction (or conjugate multiplication) between adjacent A-scan. We notices that the phase modulation will be further amplified if

measured along the transverse direction (i.e., B-mode Doppler OCT). Fig. 5.1 illustrates the flowchart of DFRM for flow image reconstruction. The first step of DFRM is to introduce a phase shift into the original spectral interferometric signal; this is numerically implemented using Hilbert transform. As shown in Fig. 5.1, the sinusoidal phase term of Eq. 5.1, i.e., $I^*_i(k, \Delta z)$, is first obtained by a Hilbert transform in k-space,

$$I_i^*(k,\Delta z) = H\left[I_i(k,\Delta z)\right] \tag{5.2}$$

where H stands for Hilbert transform operator. The result can be rewritten as,

$$I_i^*(k,\Delta z) = A_i(k,\Delta z)\sin\left[2k\Delta z + \phi + (\nu_s + \nu_f)i\tau\right],\ (i=1,\ 2,\ \ldots,\ N_x) \tag{5.3}$$

with the sine and cosine interferogram pairs in Eq. 5.1 and Eq. 5.3, an arbitrary digital Doppler frequency ν_0 can be introduced to form a new spectral interferometric signal $P_i(k, \Delta z)$

$$P_i(k,\Delta z) = I_i(k,\Delta z)\cos(\nu_0 i\tau) + I_i^*(k,\Delta z)\sin(\nu_0 i\tau) \tag{5.4}$$

which gives

$$P_i(k,\Delta z) = A_i(k,\Delta z)\cos\left[2k\Delta z + \phi + (\nu_s + \nu_f - \nu_0)\cdot i\tau\right]\ ,\ (i=1,\ 2,\ \ldots,\ Nx) \tag{5.5}$$

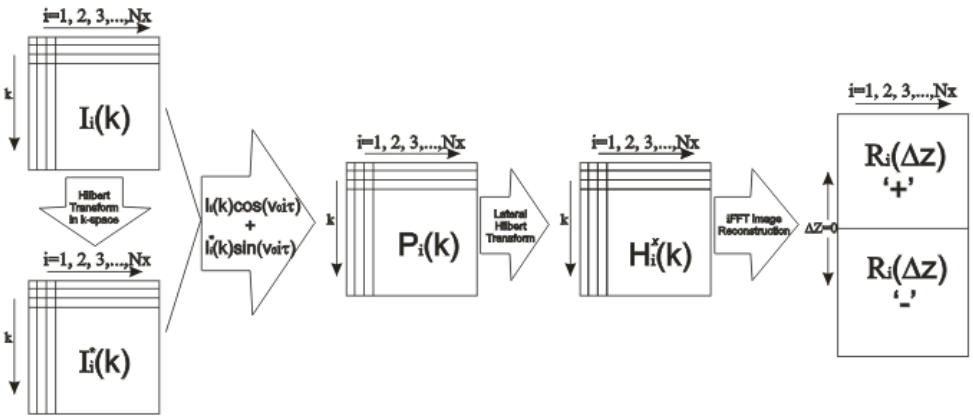

Fig. 5.1 Flow chart of DFRM. The spectral interferometric signal $I_i(k)$ was first combined with its Hilbert transform $I^*_i(k)$ to generate a target signal Pi(k) with arbitrary phase shift ν0iτ along the lateral direction. Thereafter, a lateral Hilbert transform was performed to compute $P_i(k)$'s analytic signal $H_i^x(k)$. By applying iFFT to $H_i^x(k)$ to reconstruct the

image $R_i(z)$, the signal is separated to positive or negative part of $R_i(z)$ depending on the sign of their lateral phase modulation frequency.

Apparently, Eq. 5.4 indicates that the new target function $P_i(k, \Delta z)$ allows us to numerically provide a constant Doppler frequency ν_0 or a phase modulation $(\nu_0)i\tau$ to a standard FDOCT system, thus circumventing the need for hardware implementation by either by scanning reference mirror or actuating an off-center servo mirror in the sample arm. After ν_0 is inserted, a Hilbert transform in the transverse direction is applied to obtain the analytic signal of $P_i(k, \Delta z)$ [69]. If ν_0 is within the range of (ν_s, $\nu_s+\nu_f$), then the net frequency term $\Delta\nu_{f,0}=(\nu_s+\nu_f-\nu_0)>0$ and that in the surrounding tissue background without flow $\Delta\nu_{b,0}=(\nu_s-\nu_0)<0$, which will allow us to binarize the flow ν_f above the background ν_s. As a result, the analytic signal within the dynamic flow range can be written as,

$$H_i^x(k,\Delta z)=A_i(k,\Delta z)\left\{\cos\left[2k\Delta z+\phi+\Delta\nu_{f,0}i\tau\right]+j\sin\left[2k\Delta z+\phi+\Delta\nu_{f,0}i\tau\right]\right\},\ (i=1,\ \ldots,\ N_x) \quad (5.6)$$

and that in the surrounding tissue as

$$H_i^x(k,\Delta z)=A_i(k,\Delta z)\left\{\cos\left[2k\Delta z+\phi+\Delta\nu_{b,0}i\tau\right]+j\sin\left[2k\Delta z+\phi+\Delta\nu_{b,0}i\tau\right]\right\},\ (i=1,\ldots,\ N_x) \quad (5.7)$$

where the flow in Eq. 5.6 has a positive lateral phase modulation ($\Delta\nu_{f,0}>0$), while background in Eq. 5.7 has a negative lateral phase modulation ($\Delta\nu_{b,0}<0$). Thereafter, an inverse FFT (iFFT) along the axial (z) direction,

$$R_i(\Delta z)=iFFT\left[H_i^x(k,\Delta z)\right] \quad (5.8)$$

will allow for reconstruction of the image $R_i(\Delta z)$ in which the Doppler flow part distributed in the positive side (i.e., $\Delta z\geq 0$), thus can be explicitly differentiated from the noise background distributed in the negative side (i.e., $\Delta z\leq 0$) [69].

More importantly, as v_0 is arbitrary, the above procedure can be repeated to ramp v_0 from $-\pi/(i\tau)$ to $\pi/(i\tau)$ to cover the full-range Doppler frequency shift, rendering this numerical approach highly suitable for clinical applications with quantitative measurement capability, where pre-determination of the optimal v_0 critical to enhancing Doppler flow detection is always difficult if not impossible. Fig. 5.2 further illustrates how v_0 can be ramped to enable quantitative flow measurements. To simplify the procedure, we set the A-scan duration τ=1 and system phase noise v_s=0, so that $(v_s+v_f-v_0)\tau = (v_f-v_0)$. For a positive flow (e.g., $v_{f1}>0$), Fig. 5.2(a) shows that, as v_0 (Red curve) is ramped, e.g., $v_0(n)=-\pi+\pi(2n/N)$, $n=0, 1, \ldots N$ from $-\pi$ to π, the green curve $\Delta v_f=(v_f-v_0)$ changes sign from "+" to "-" at $v_0(i)=v_{f1}$. The flow component in the reconstructed image $R_i(\Delta z)$ will flip accordingly from "+" to "-", indicating a positive flow at v_{f1}. Similarly, Fig. 5.2(b) shows the sign change of Δv_f for a negative flow at $v_0(j)=v_{f2}$. Noteworthily, the dashed arrows indicate the periodic 2π phase ramp of Δv_f in both cases.

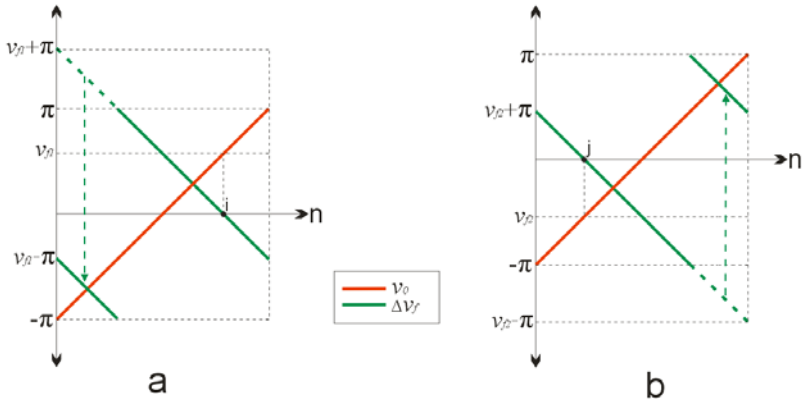

Fig. 5.2 Illustration of DFRM for bidirectional flow quantification. a): "+" flow, b): "-" flow. v_{f1}: a positive flow, v_{f2}: a negative flow, v_0 digital Doppler frequency shift ramped from $-\pi$ to π. Δv_f: net frequency term $\Delta v_f = (v_f - v_0)$; i: $\Delta v_f = 0$ at $v_0(i)=v_{f1}$; j: $\Delta v_f = 0$ at $v_0(j)=v_{f2}$. Green arrows: phase jump dues to periodic 2π phase ramping.

5.1.2 Experimental setup

DFRM is a numerical approach for flow imaging enhancement; therefore, a standard FDOCT system was used to examine the efficacy of this technique in both tissue phantom study and *in vivo* biological tissue study. As depicted in Fig. 5.3, a pigtailed high-brightness (18mW) broadband source (BBS) was employed to illuminate a fiberoptic interferometer, whose central wavelength and full-width-half-maximum spectral bandwidth were λ=1310nm and $\Delta\lambda$=90nm to provide a source coherence length of $L_c \approx 8\mu m$. A green diode laser (4mW, 532nm) was coupled via a 95%:5% fiber coupler to visually guide 2D and 3D OCT scans. Light exiting the reference fiber was collimated (ϕ1.6mm), attenuated and retroreflected by a reference mirror mounted onto a 1D stage to match the path length in the sample arm of the Michelson interferometer. The sample arm was connected to a handheld stereoscope in which light exiting the fiber was collimated (ϕ4.5mm), scanned laterally by a 2D servo mirror, and focused by an achromate (f=40mm) onto the biological tissue under imaging. The sample arm could instead be connected to a MEMS-based OCT endoscope in which light exiting the fiber was collimated (ϕ1.2mm), scanned laterally by a 1D MEMS mirror, and focused by an achromate (f=10mm) onto the lumen of biological tissue for *in vivo* imaging. The light beams returning from the sample and reference arms were recombined in the detection fiber and connected to a spectral imager in which light was collimated by a fiberoptic achromate (f=55mm), diffracted by a holographic grating G (d=1200mm^{-1}) and focused by an achromatic lens group (f=120mm) onto a linear InGaAs array. The detected spectral graph, including spectrally encoded interference fringes from different depth (Δz) within the biological sample, was digitized and streamlined to a workstation via a 2-

channel 12bit A/D at 5MHz, allowing for 2D imaging (1024pixel × 1000pixel) at ~8fps. The axial and transverse resolutions of the system were ~9μm and ~12μm, respectively. Because of extensive computation, 2D and 3D DFRM flow images were processed and displayed in post-image mode; however, conventional Doppler FDOCT was displayed at ~5fps for locating subsurface flows.

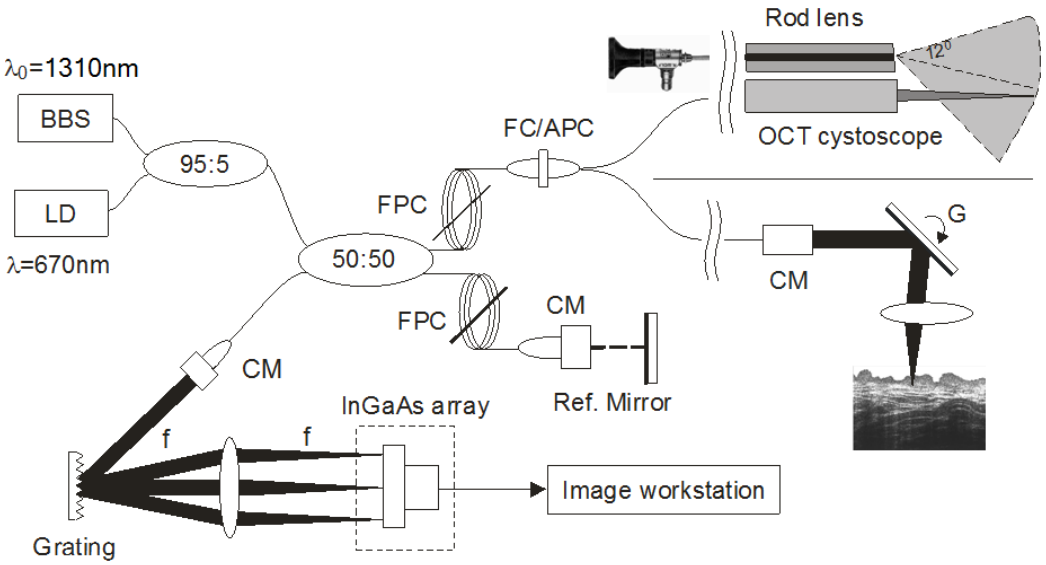

Fig. 5.3 A sketch of a fiberoptic Spectral-domain OCT setup. The sample arm was connected to a handheld stereoscope for phantom study or a MEMS-based OCT endoscope for in vivo imaging. BBS: broadband source (λ0=1320nm, ΔλFWHM=90nm, P=18mW); LD: aiming laser diode (λ=532nm); CM: fiberoptic collimator, FPC: fiberoptic polarization controller. 2D OCT imaging rate: ~8pfs; Spatial resolutions: 9μm axially × 12μm laterally.

5.2 Results

5.2.1 Tissue phantom simulation

In order to evaluate the capability efficacy of DFRM for enhancing the flow detection, we first conducted numerical simulation in which a group of flows with varying sizes and flow velocities were modeled. To do so, we normalized the signal amplitude in Eq. 5.1, i.e., $A_i(k, \Delta z)=1$ and added computer-generated 2D random

Gaussian phase noise $\phi_n(i, \Delta z)$ to simulate the phase noise background in a Doppler OCT image, i.e.,

$$I_i(k,\Delta z) = \cos[2k\Delta z + \phi_n(i,\Delta z) + \nu_f i\tau], \ (i=1, 2, \ldots, Nx) \tag{5.9}$$

For mathematical simplicity, a circular parabolic profile was used to simulate laminar flows, i.e., $\nu_f(x,z)=\nu_{f,max}\{1-[(x-x_0)^2+(z-z_0)^2]^{1/2}/r\}$ where $\nu_{f,max}$ was the vertex at the flow center (x_0, z_0) and r was the radius of the vessel. The A-scan duration was set to τ=1 so that $\nu_f \tau=\nu_f$ in Eq. 5.9. Also, taking into account that the phase term is folded in every [-π, π] period, a flow range normalized to [0, π] would be sufficient to evaluate the SNR characteristics of the flow detection; therefore, two typical flow rates were chosen in our modeling, e.g., $\nu_{f,max}$=0.8π for high-velocity group and $\nu_{f,max}$=0.2π for low-velocity group. The mean of the phase noise $\phi_n(i, \Delta z)$ was set to 0 for both groups and the standard deviation was set to 0.02π and 0.08π respectively as $0.1\,\nu_{f,max}$. In each group, three sizes with radius r descending from 50-, to 35- and 20-pixels were used to simulate large, intermediate and small flows centered at x_0, z_0=100 in an FDOCT image of N_x, N_z=200 pixels. For each of the 6 flow configurations, both DFRM and direct phase subtraction method (PSM) used in ordinary Doppler FDOCT [61] were applied to reconstruct the flow images. In DFRM modeling, ν_0 was set to be 1/10 of the vertex $\nu_{f,max}$, i.e., ν_0=0.08π and ν_0=0.02π for the high- and low-velocity flow groups, respectively. The flow profiles reconstructed by DFRM and PSM (in logarithmic scale) and normalized by their peak values were collaterally plotted in Fig. 5.4, and the results clearly demonstrated the enhancement on flow delectability by DFRM over the PSM.

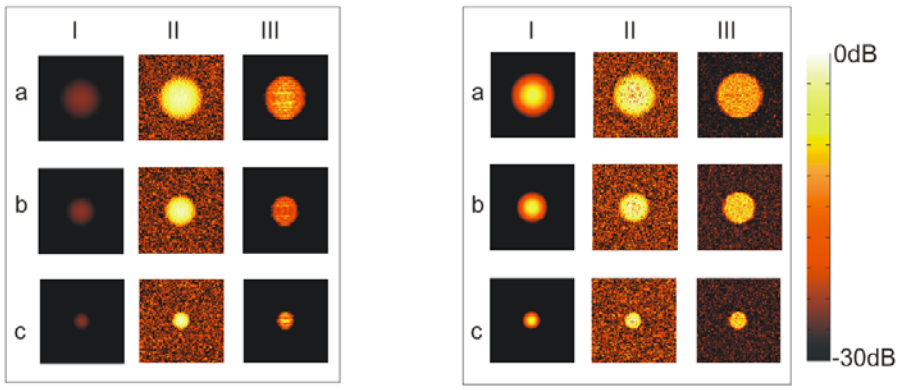

Fig. 5.4 A comparison between PSM and DFRM for simulated flows. Panels (A) and (B) are the results of low-velocity ($v_{f,\,max}$=0.2π) and high-velocity ($v_{f\,max}$=0.8π) flows with phase noise $\phi_n(i, \Delta z)$ proportional to their velocity. Rows (a, b, c): flows with radii of 50-, 35- and 20-pixels, respectively. Columns (I, II, III): noise-free flow inputs, flows reconstructed using PSM and DFRM, respectively. The images from both PSM and DFRM methods were normalized by the maximum value and displayed in log scale with a pseudo color bar from -30dB to 0dB

Yet it is noteworthy that unlike PSM which provided quantitative assessment of flow velocity by subtracting the phase difference between successive axial lines, DFRM by v_0 thresholding could only provide qualitative assessment (i.e., angiography) which detected the existence of flow rather than its velocity. To enable DFRM for quantitative flow imaging, we linearly ramped v_0 with a relatively small step size of Δv_0, i.e.,

$$v_0(i) = v_0 + i \cdot \Delta v_0, \quad (i=1, 2, \ldots, Nx) \tag{5.10}$$

If the velocity of a flow or part of a flow profile $v_f(x,z)$ fell within the range of $[v_0(i),\ v_0(i+1)]$, its lateral phase modulation (LPM), $\Delta v_f(x,z;i) = v_f(x,z) - v_0(i)$ would change sign when v_0(i) was increased to v_0(i+1). According to Eq. 5.6 and Eq. 5.7, the corresponding transverse Hilbert transform would flip the signal from positive to negative to be differentiated by Eq. 5.8. To further enhance the sensitivity of $R_i(\Delta z)$ to differentiate $\Delta v_f(x, z; i)$, the ratio between the positive and negative images, i.e.,

$R_i(\Delta z>0)/R_i(\Delta z<0)$ was calculated, then a threshold of 1 is set to binarize this ratio image to conclude the sign of $R_i(\Delta z)$. Therefore, a subtraction of the two binarized ratio images yields the net flow signals within ($v_0(i), v_0(i+1)$); hence, by ramping v_0 from low to high and from negative to positive, the quantified flow velocity profile can be obtained at the resolution of Δv_0. Fig. 5.5 illustrates the reconstruction procedure for ($v_0(i)$=0.3, $v_0(i+1)$=0.4) of the flow (r50, 0.8π) simulated in Fig. 5.4.

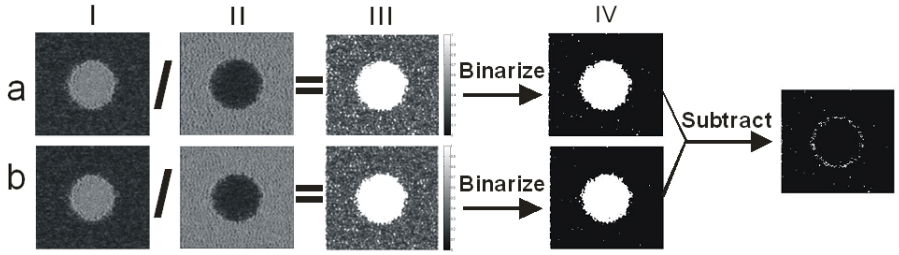

Fig. 5.5 Graphic illustration of DFRM for flow quantification. Rows (a, b) show the DFRM results for $\nu_0(i+1)=0.4\pi$ and $\nu_0(i)=0.3\pi$. Columns (I, II) show the positive and negative parts computed from Eq. 5.8, and columns (III, IV) are the ratio and the binarized ratio images, respectively. The final ring-shaped image shows the area having a velocity profile within the range of (0.3π, 0.4π).

To test the feasibility of this quantitative approach, we applied DFRM to this simulated flow (r50, 0.8π) using step sizes of Δv_0=0.02π and Δv_0=0.01π, respectively. The results were plotted in Fig. 5.6 in which the flow profile computed by PSM was shown for comparison. It is obvious that DFRM was able to recover the flow profile fairly accurately; whereas PSM suffered severely from overwhelming phase noise thus preventing it from effective tracking of the velocity variations along the radial direction. Interestingly, a comparison between the results from Δv_0=0.02π and 0.01π reveals that increasing frequency ramping accuracy did not necessarily yield better quantification results. This suggests that under noisy condition, DFRM may provide limited resolution to threshold or binarize the sign of LPM when $\Delta v_f(x, z; i)\rightarrow 0$ and therefore $\Delta\nu_0$ should be

appropriately chosen to maximize the effort of enhancing the resolution for flow velocity recovery while minimizing the computation load.

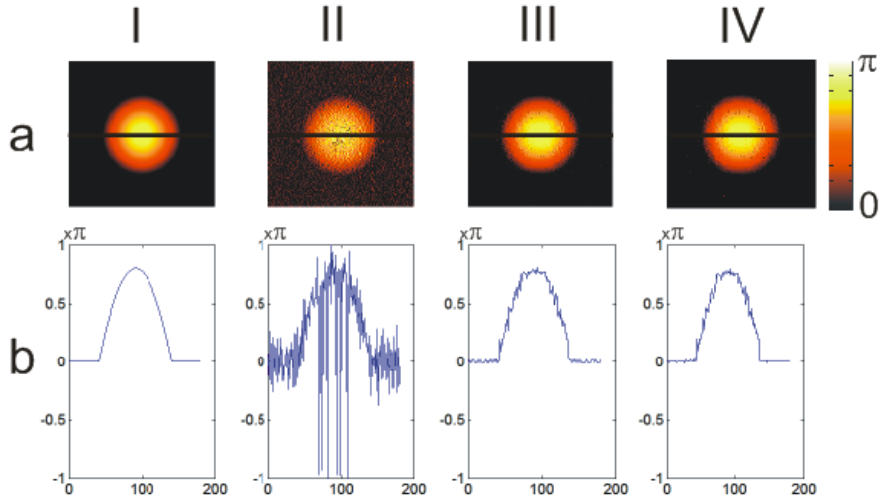

Fig. 5.6 A comparison between PSM and DFRM for quantitative of simulated flow. Row (b): plots the flow profile along the central lines in row (a). Columns (I, II, III, IV): noise-free input circular flow, flows quantified by PSM and DFRM with $\Delta\nu 0=0.02\pi$, 0.01π, respectively.

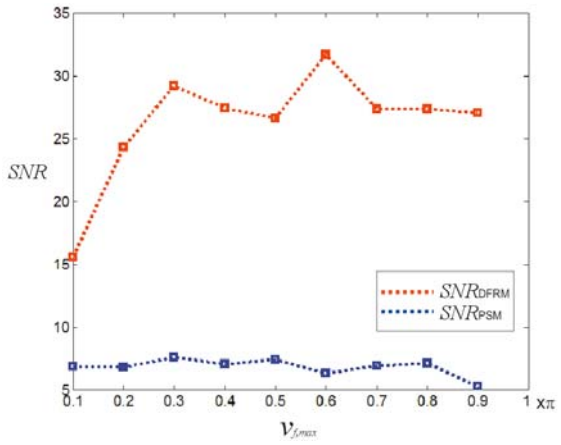

Fig. 5.7 SNR comparison between PSM and DFRM for quantitative reconstruction of computer simulated flow at different velocities, e.g., $\nu_{f,\,max}$, from 0.1π to 0.9π. The step size of DFRM was set to $0.02\,\nu_{f,\,max}$.

Fig. 5.7 further compares the SNR between PSM and DFRM for quantitative reconstruction of flows at different velocities, e.g., νf, max, from 0.1π to 0.9π. In the modeling, the calculated velocity noise νn was defined as the difference between the

reconstructed velocity νr and the input noise-free velocity νf , i.e., νn=νr-νf ; then, the SNR was according defined as the ratio between νf, max and the standard deviation of νn, i.e., SNR=νf, max/σn. The DFRM step size was set to 0.02νf, max. The results clearly indicate that DFRM provides superior SNR (~25) over PSM (~7) for quantitative flow imaging. Interestingly, in the low flow range (e.g., νf, max=0.1π to 0.3π), the SNR increases dramatically from 15 to 25 whereas PSM shows no significant difference.

Fig. 5.8 further shows the result of DFRM to extend the dynamic range of flow measurement beyond the [-π, π] limit to 10π high flow velocity. As a result of enhanced SNR, DFRM was to provide high-contrast concentric rings that reflected the 2π phase wrapping effect so that the high flow velocity could be computed by summing up the ring numbers. In comparison, PSM could barely resolve the rings due to excessive phase noise background. It is noteworthy that for proof of principle, this simplified flow model did not simulate the phase washout effect, a high complex issue in the presence of fast flow which may lead to fringe washout of the spectral interferometric signals if recorded in finite acquisition time. This undesirable effect could potentially affect the accuracy of high flow recovery using DFRM.

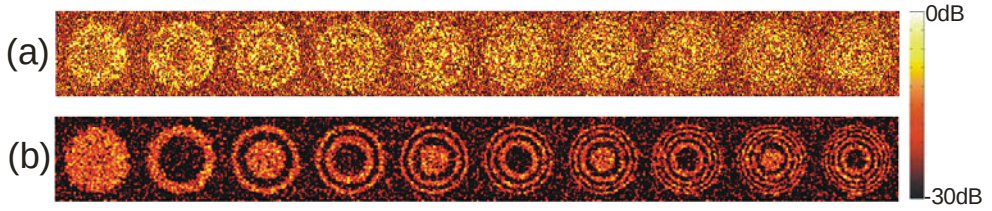

Fig. 5.8 Graphic illustration for extending the dynamic range of flow velocity from π to 10π using PSM (a) and DFRM with thresholding at 0.1π (b). Both images were normalized by their peak values and displayed logarithmically in pseudo color ranging from -30dB to 0dB. DFRM is able to clearly resolve all 5 concentric rings resulted from phase wrapping of the fast flow, whereas PSM barely differentiate them from the background noise.

5.2.2 Experimental validations

Fig. 5.9 shows the result of flow validation study using tissue phantom, in which the cross section of a controlled flow consisting of 1% intralipid solution ($\mu_s \approx 2.4 cm^{-1}$) in a ϕ0.50mm translucent conduit was imaged by FDOCT at a tilting angle of $\theta = 12^0$. Both DFRM and PSM were able to quantify the flow profile. However, in consistence with the simulation results in Fig. 5.6, DFRM suppressed the phase noise around the non-flow area more effectively (e.g., the noise level or the background variation decreased 75%) so that the reconstructed velocity profile was smoother, i.e., more accurately quantified.

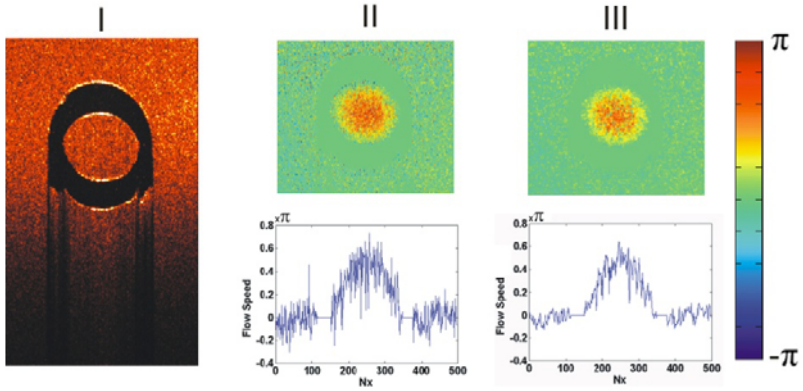

Fig. 5.9 Experimental validation using tissue flow phantom. Column (I): structural FDOCT image of flow in a ϕ0.50mm translucent conduit using 1% intralipid solution ($\mu s \approx 2.4 cm-1$); columns (II, III): cross-sectional Doppler OCT images and median velocity profiles quantified by PSM and DFRM ($\Delta v0 = 0.02\pi$), respectively.

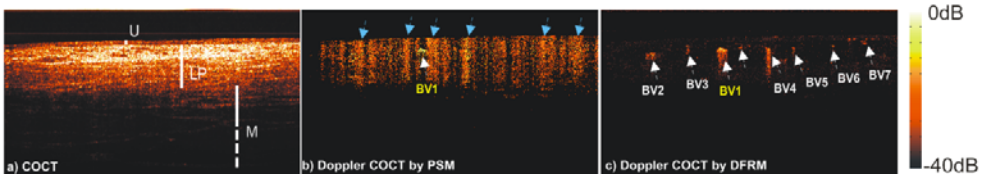

Fig. 5.10 Endoscopic FDOCT images of human bladder *in vivo*. a): structural OCT image, b), c) Doppler OCT images reconstructed by PSM and DFRM (single frequency thresholding at 0.2π), respectively. U: urothelium, LP: lamina propria, M: muscularis. White arrows: blood vessels (BVs); blue arrows: vertical stripes (phase noises) induced by bladder motion or surgeon's handshaking.

Following successful simulation and tissue flow phantom calibration studies, we

further validated the technique *in vivo* in our ongoing clinical study for bladder cancer diagnosis. Detection of abnormal angiogenesis in bladder wall is of great clinical significance for both cancer diagnosis and for analysis and assessment of other pathological and physiological diseases in the bladder. For instance, angiogenesis into bladder epithelium is deterministic of bladder carcinogenesis; therefore, detection of angiogenesis in bladder epithelium by Doppler OCT can potentially provide crucial diagnosis of bladder cancer, thereby further improving the diagnostic sensitivity and specificity. However, the excessive phase noise has been found to impose a major challenge leading to limited dynamic range of flow detection in endoscopic Doppler OCT. Results of our in vivo clinical study revealed that the excessive phase noise induced by bladder motion and handshaking compromised the detectability of subsurface blood flows in bladder wall; therefore, enhancing the sensitivity of endoscopic Doppler OCT is of high clinical relevance. For the purpose of bladder cancer diagnosis, angiography instead of quantitative Doppler flow imaging is sufficient. Fig. 5.10 compared the results of MEMS-based cystoscopic FDOCT reconstructed by DFRM versus PSM. Panel a) showed the morphological image of a normal human bladder in which the urothelium (U), lamina propria (LP) and upper muscularis were clearly delineated based on their backscattering differences. Panels b) and c) showed the corresponding Doppler COCT images reconstructed by PSM and DFRM based on a single frequency thresholding (in order to suppress the vibration noise caused by handshake, a relatively high threshold at 0.2π was applied, i.e., $\nu_0=0.2\pi$). Because of high phase noise, only a large, high-velocity flow BV1 was affirmatively identified and the phase noise $\nu_s(x)$ induced by bladder motion and handshake was obvious as indicated by the blue arrows (vertical stripes) in

panel B). In comparison, 7 more blood flows were uncovered among which BV1-BV5 were affirmatively identified and BVs 6-7 were likely smaller vessels but artifacts could not be ruled out. Interestingly, motion-induced vertical stripes were effectively reduced by taking advantage of the high SNR of the DFRM method.

5.3 Discussion and conclusion

Doppler OCT, in both time-domain and Fourier-domain, has been developed over the past several years to permit subsurface flow imaging in biological tissue quantitatively and at high spatiotemporal resolutions. It is particular interesting for FDOCT technique because both structural and Doppler flow images can be acquired and overlapped in real time and with no or minimal system modification. Yet, the majority of Doppler OCT techniques published so far are based on direct measurement of Doppler flow induced phase changes between successive axial lines or A-scans of a 2D or 3D OCT image [11-19]. This approach, however, is prone to excessive noise due to phase instability induced by the complications such as speckle noise, sample heterogeneity, dynamic multiple scattering of living tissue, and system vibration. Optical angiography (OAG) [69, 73] is a newly developed technique which OAG utilizes hardware implementation (e.g., by either moving the reference mirror with a PZT translator or scanning an off-center servo mirror at sample arm) to generate a proper threshold frequency modulation to separate moving elements from noisy static background. Although not yet quantitative, this technique has been shown to substantially increase the sensitivity and resolution for detecting subsurface flow distribution, including minute arteriolar flows which conventional Doppler OCT based on direct PSM failed to detect.

In this article, we proposed a numerical approach (DFRM) to effectively enhance flow imaging capability of standard FDOCT technique with no further hardware modification. As derived in Eq. 5.5, this technique allows for numerical introduction of an arbitrary phase modulation to the interference spectrograph measured by FDOCT, thus circumventing the need for phase modulation by mechanical scanning. Simulation of various flows in noisy background presented in Fig. 5.4 indicates that DFRM was able to effectively offset and thus separate the flow signal from noise background, thus greatly enhancing the sensitivity and SNR for flow detection. As a software-based approach, this method can lift the potential complications of the hardware counterpart in terms of imaging rate, calibration (i.e., pre-selection) of threshold frequency ν_0, drift of ν_0 caused by nonlinearity and instability of mechanical scanning. More importantly, by digital ramping of ν_0 using Eq. 5.10 which can be computed post FDOCT imaging, DFRM enables quantitative Doppler flow imaging with increased SNR as shown in flow simulation (Fig. 5.6-Fig. 5.7) and flow phantom (Fig. 5.9) studies. Such quantitative flow imaging capability can be very useful for applications in quantitative analyses of the spatiotemporal hemodynamics of functional brain activations and responses to behavioral, cognitive, and pharmaceutical paradigms. In addition, the phase noise induced by tissue motion, in particular, by handshaking in endoscopic Doppler OCT can be numerically compensated by DFRM, thus rendering a promising method for clinical diagnosis, such as angiogenesis associated with carcinogenesis.

Despite dramatic improvement provided by OAG and DFRM, Doppler flow imaging is inherently prone to ambient noise deterioration. Unlike structural OCT, a high-velocity flow does not necessarily result in equivalently enhanced SNR due to the

fact that the flow signals fold every 2π. Although our high-velocity flow model in Fig. 5.8 demonstrated the potential DFRM for unwrapping the phase folding induced by fast flows, it is noteworthy that the simulation did not considered other complications in real imaging scenario, e.g., phase washout, sample heterogeneity, amplitude noise and so on. Therefore, our future work will improve current DFRM algorithm to more effectively suppress the background noise and to examine its performances in various experimental conditions and in animal and clinical applications. It is also noteworthy that DFRM, especially quantitative DFRM is exclusively computation intensive which involves multi-dimensional Hilbert transform and FFT. For a 1024pixel × 1000pixel flow image, a 50-step quantitative DFRM reconstruction takes ~60s on a 3.2GHz PC with a custom MATLAB program whereas PAM only takes ~3s; thus, parallel computing or fast computation unit, e.g., exquisite digital signal processing (DSP) with optimized algorithms is required to facilitate instantaneous 2D and even 3D flow display, which is of high clinical relevance for on-site endoscopic OCT/ Doppler OCT diagnosis.

In conclusion, a phase ramping technique termed DFRM is reported to effectively enhance the flow imaging capability of conventional FDOCT. Results of theoretical modeling, tissue flow phantom validation and preliminary endoscopic FDOCT demonstrate the potential of DFRM to significantly enhance the sensitivity and SNR of FDOCT for quantitative subsurface flow imaging at high spatiotemporal resolutions. As a numerical approach, DFRM involves no additional hardware modification to standard FDOCT technique, thus rendering it highly suitable for real-time 2D and 3D flow imaging.

Chapter 6 DFR-OCT optimization and denoising

Chapter 5 describes a numerical method called DFRM to effectively improve the performances of Doppler OCT. As this method demands intensive computation, DFRM is usually performed post data acquisition session so as to not affect the system speed and therefore lacks the capability for real-time or instantaneous imaging. In addition, despite the SNR improvement by DFRM, Doppler OCT still suffers excessive background noises that requires attention. To address these problems, this chapter describes several methods, including 1) DFRM acceleration: a new algorithm proposed to half the computation load of DFRM, this method is then programmed to run on GPU to further reduce the computation time to >10 times; 2) Bulky noise rejection: an iterative correction method invented to effectively remove the motion caused phase noise; 3) Quantitative capillary flow measurements: by combining high sensitivity OCT angiogram and Doppler OCT, we demonstrate the potential of quantitative measurement of capillary flows in biological tissues

6.1 DFRM acceleration

As discussed in previous chapter, the detected spectral interferogram can be denoted by the following equation

$$I_{OCT}(k;\Delta L,x) = S(k)\left[(I_s + I_r) + 2\sqrt{I_s I_r}\cdot cos(k\Delta L + \phi_\tau(\Delta L,x))\right] \quad (6.1)$$

where I_s and I_r are the intensities in the sample and reference arms, x is the transverse position, *S(k)* is the source spectrum ($k=2\pi/\lambda$ is the wavelength of light). The relative phase $\phi_\tau(\Delta L, x)$ is can be expressed as[74]

$$\phi_\tau(\Delta L, x) = \phi_0 + (2\pi/\lambda)\cdot\left(v_f + v_b + v_R\right)\cdot\tau\cdot n_x \tag{6.1}$$

where ϕ_τ is the initial phase, n_x=1,2,…,N_x is A-scan index (N_x is the number of scans along x-axis), v_f and v_b are the velocities of Doppler flow and background noise flow. If the digitally imposed frequency-ramping offset v_R is chosen to ensure,

$$\left(v_f + v_b + v_R\right)\cdot(v_b + v_R) < 0 \tag{6.2}$$

Hilbert transform (sensitive to frequency thresholding, i.e., flipping sign) along x-axis can easily separate these two types of flow signals, i.e., to differentiate all Doppler flows with v_f above the noise ground v_b for non-quantitative angiographic detection[74]. To further quantify Doppler flow rate v_f which can be normalized to the range of (-1, 1], v_R can be similarly ramped over N steps with a step size of $\Delta v=1/N$:

$$v_R(i) = v_R + i\cdot\Delta v \text{ (where } i=-N/2,\ldots,N/2) \tag{6.3}$$

to search for points at which the transverse modulation frequency of Hilbert transform flips sign. Here, because of phase wrapping effect, the ramping range can be further reduced to half to save computation efforts. Then, based on Eq. 6.3 and Eq. 6.4 the flow rate for DFR-OCT can be derived as

$$\left|v_f\right| = \Delta v\left\{\sum_{i=-N/2}^{-1}\left[(v_f - i\Delta v) < 0\right] + \sum_{i=1}^{N/2}\left[(v_f - i\Delta v) > 0\right]\right\} \tag{6.4}$$

where the two sets of summation operations accumulate the results from each step and effectively reduce the noise level because of the averaging effect. Here, $(v_f - i\Delta v)>0$ and

$(v_f - i\Delta v) < 0$ are both Boolean functions (i.e., 1 for 'true', 0 for 'false'), and the sign of v_f can be determined by

$$sign(v_f) = \begin{cases} (+) & if \sum_{i=1}^{N/2}\left[(v_f - i\Delta v) > 0\right] > \sum_{i=-N/2}^{-1}\left[(v_f - i\Delta v) < 0\right] \\ (-) & if \sum_{i=1}^{N/2}\left[(v_f - i\Delta v) > 0\right] < \sum_{i=-N/2}^{-1}\left[(v_f - i\Delta v) < 0\right] \end{cases} \quad (6.5)$$

To compare the new algorithm with previously reported one, 2D and 3D Doppler OCT imaging was performed in an animal study where. We applied both to the same OCT raw data and the results are shown in Fig. 6.1. The left column collaterally plots flow images reconstructed by a) conventional phase subtraction method, b) previous DFRM, and c) DFRM with new algorithm respectively. Apparently, the last one shows the minimum background noise. In panel (d), a 3D quantitative CBF image acquired by Doppler OCT is shown to demonstrate that with the new approach, Doppler OCT is able to visualize some big capillary flows around 10~15um.

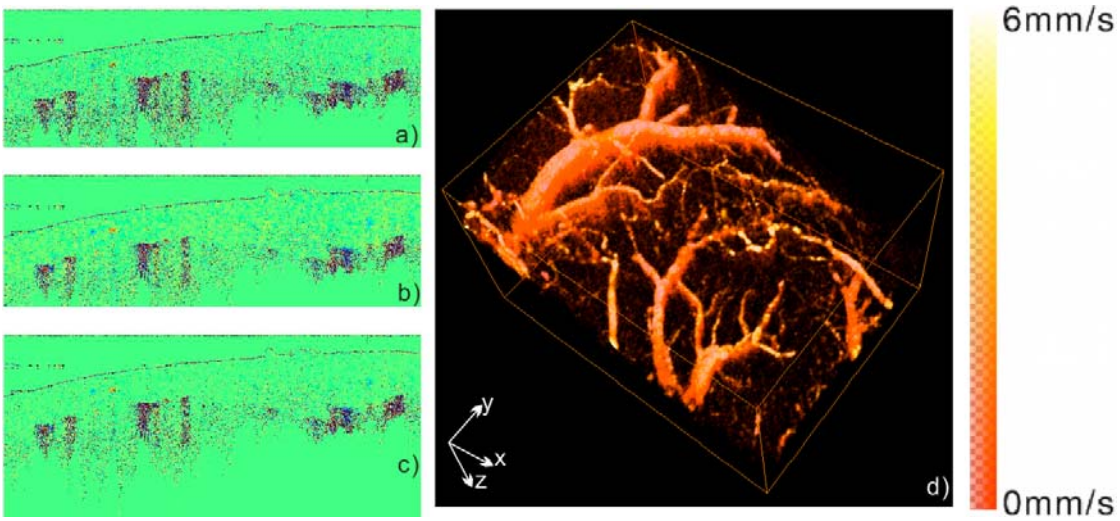

Fig. 6.1 comparison of flow reconstruction using different methods. a)PSM, b)DFRM and c)DFRM with new algorithm, image size: 3mm by 1.2mm. d): 3D CBF image by DFRM with new algorithm. Image size: 3mm by 2.2mm by 1.7mm (x-y-z).

Recently, dedicated graphic processing units (GPUs) installed in video cards in

desktop computers have shown it great power for general purpose computation. This was realized by a multi-core architecture to perform numerous threads in parallel. A close look into DFRM suggests the computation of this method can be conveniently distributed to multiple threads, as both FFT and Hilbert transform can be performed simultaneously and independently, therefore DFRM is ready to utilize the power of GPU to speed up the calculation. To validate the usage of GPU in DFRM, we adapted the algorithm in MATLAB with a GPU enabled package, JACKET[75], and compared the flow image and time spent using GPU and CPU in Fig. 6.2. As for this case, an nVidia Geforce 9300 GE is able to provide identical results but ~3 times faster than an intel Xeon CPU at 3.20GHz CPU. It is noticeable that current GPUs such as nVidia GTX 295 run dozens of times faster than 9300 GE, hence renders the possibility of instantaneous or even real-time blood flow measurement by DFRM enhanced Doppler OCT.

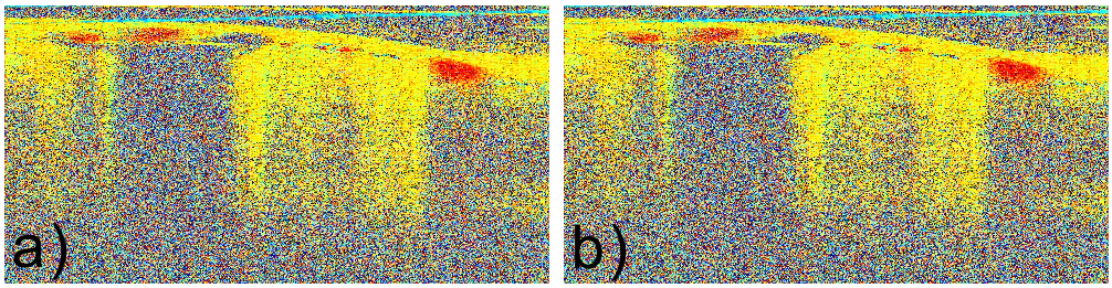

Fig. 6.2 Comparison of GPU and CPU for DFRM flow reconstruction, image size 3mm (width) by 1.5mm (depth). Elapse time for (a)CPU: 86.429885 second, (b)GPU: 30.730168 second. GPU provides identical results and is ~3 times faster.

6.2 Compensation of bulky motion artifact

Bulky motion caused phase artifact (BMA) is inevitable in most *in vivo* applications and greatly compromise the fidelity of measured Doppler signal. Compensation methods based on histogram analysis or A-line averaging have recently

been reported to remove BMA in human retina imaging based on the assumption that BMA appears as DC-offset of the phase signal for each A-line[73, 76]. However, in some extreme cases such as handheld endoscopic OCT studies, constant intensive handshaking can cause overwhelming BMA that hampers histogram analysis. A-line averaging, on the other hand, only works when most of the A-line signal originates from static tissue, but fails to Compensate BMA when high blood volume exists within the scanned area. Hence, a more robust method that tolerable to such extremities is highly desirable.

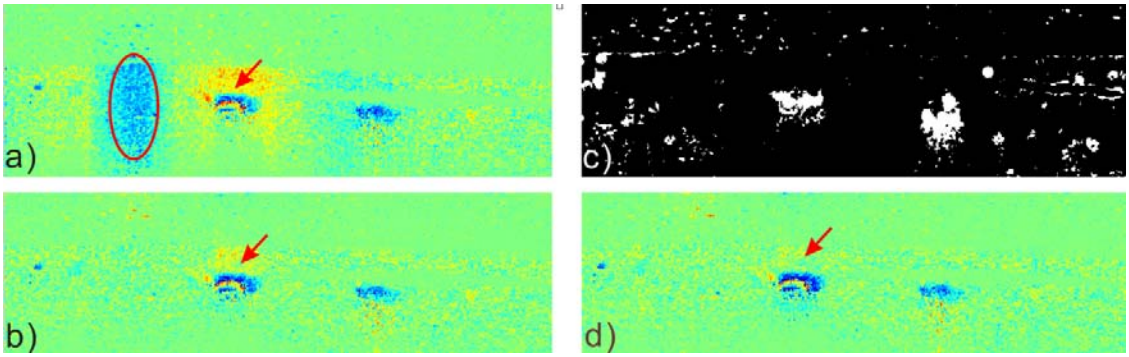

Fig. 6.3 BMA compensation using modified A-line averaging method. a) Doppler flow image with BMA, b) flow image compensated by direct A-line averaging, c) the mask used to exclude blood flows, d) flow image compensated by A-line averaging of the flow image screened by mask in c)

Here we describe a new method to address this issue by excluding the dynamic flow part before A-line averaging to estimate bulk motion caused phase offset. In order to eliminate the heterogeneity noise, A-scan usually is performed at a relatively high sample density, e.g., 10 samples per size of focus profile in sample arm. This ensures a high correlation between adjacent A-lines and prevents sudden phase change caused by sample heterogeneity. As a result, the intensity change between adjacent A-lines is also smoothened. However, this change is augmented by dynamic flows where the moving particles change scattering patterns and thus the intensity continuously. Therefore, by

calculating the intensity difference between adjacent A-lines, an image can be generated as a non-quantitative flow map. This intensity based flow map is not sensitive to BMA, whose major effects apply only to Doppler phase signals and thus can be used to screen the flows before A-line averaging for BMA estimation. Fig. 6.3 shows the DFR-OCT acquired cross sectional CBF images before (a) and after the compensation of BMA using direct (b) and screened (d) A-line averaging. The mask used to screen dynamic flows is shown in panel c). Both approaches successfully remove the BMA within the red circle, but as indicated by the arrow direct A-line averaging fails to completely remove the BMA above a big blood vessel panel b). This residual noise is removed in Panel d) after excluding the flow area by mask in panel c) for A-line averaging. Fig. 6.4 further shows that the method is able to compensate for severe BMA in extreme cases such as *in vivo* endoscopic imaging to recover blood flows buried in BMA.

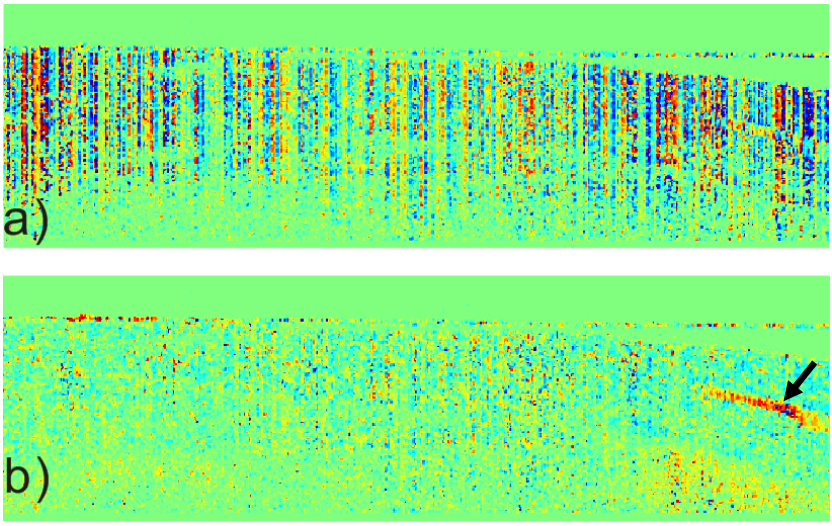

Fig. 6.4 *in vivo* bladder Doppler flow imaging acquired by endoscopic DFR-OCT. a) Doppler flow image with severe BMA, b) flow image after correction manifests a clear blood vessel that hides in BMA in panel a)

6.3 Doppler image filtering

Doppler noises inherited from physical factors such as tissue heterogeneity, short noise and speckle noise are persistent throughout the regular processing method and can only be effectively reduced by over-sampling and averaging at the cost of imaging speed. Therefore, it is necessary to balance the Doppler noise level and averaging number according to specific experimental requirements. To find out the relationship between Doppler noise level and sampling/averaging numbers, **we** designed an experiment and analyzed the data as follows: *in vivo* CBF cross sectional images were taken by the DFR-OCT system described in Chapter 5. The system ran at 15kHz and the B-scan covered 2.1mm in 700 steps. For each step point, the measurement was repeated 100 times for extendable averaging. The Doppler flow signal was then reconstructed and averaged from 1 to 100 times. Fig. 6.5a shows a selection of resulted flow images that were averaged at different numbers 1, 3, 10 and 50. The background phase noise level decreases substantially when averaging number increases. Fig. 6.5b plots the curve to show this relationship between noise level and averaging number. Based on this curve, an appropriate averaging or oversampling numbers can be figured according to the phase sensitivity or SNR requirement. In addition, both the images and the curve shows that averaging as an approach to remove noise works more sufficient at low numbers (10 times averaging removes ~80% background noises).

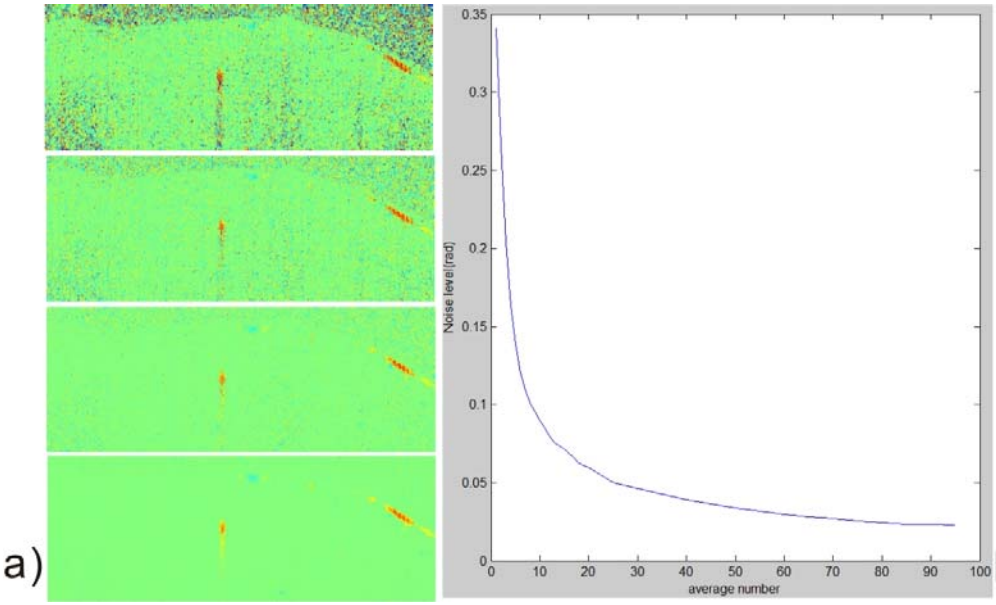

Fig. 6.5 Noise level at different averaging numbers. Panel a) shows the 2D flow images with averaging number of 1, 3, 10, 50. Panel b) shows the complete curve of noise level vs. averaging number.

In the case of high speed imaging where averaging is not applicable, digital imaging processing methods such as image filtering is usually carefully designed and applied to suppress the phase noises without obvious image resolution degradation. This raises a problem in Doppler images, which contain artifacts that are caused by the phase wrapping effect and have to be taken care of to avoid unnecessary phase cancelation during image filtering. Complex domain filtering for Doppler images is thus proposed and the procedure can be mathematically described as the following:

$$\begin{cases} C(x,y) = \cos(P(x,y)) + i\sin(P(x,y)) \\ C'(x,y) = imfilter(C(x,y)) \\ P'(x,y) = angle(C'(x,y)) \end{cases} \tag{6.6}$$

where P is the original phase image whose value ranges from $-\pi$ to $+\pi$. By converting the image from real domain to complex domain, common filtering methods calculate real and imaginary part separately, thus avoiding the phase cancellation caused by wrapping effect.

Fig. 6.6 shows the filtered Doppler flow images in real domain and complex domain filtering by a 5×5 Gaussian window. In real domain, the original saturated flow areas, Fig. 6.6(a), were diminished substantially in the filtered Fig. 6.6(c). On the contrary, all flows were well preserved in complex domain filtering, Fig. 6.6(d), with effectively suppressed background noise.

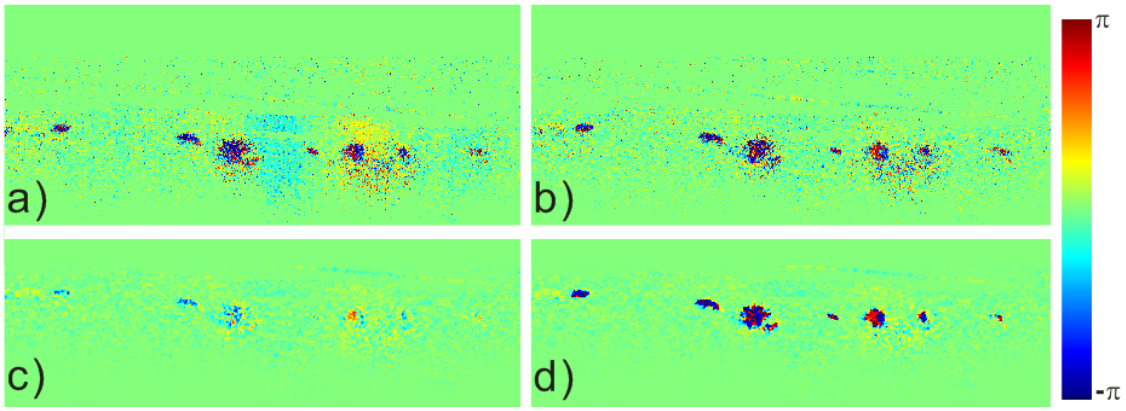

Fig. 6.6 Doppler flow filtering in complex domain. a) Doppler flow image acquired without image processing; b) flow image with BMA removed; c) flow image filtered by 5x5 Gaussian filter; d) flow image filtered by 5x5 Gaussian filter in complex domain.

In summary, Doppler OCT flow image suffers from excessive intrinsic noise that is difficult to remove and requires further processing to improve the SNR and improve flow visualizations. The methods presented here show the potential of such image processing techniques to remove BMA and background noise. It is noteworthy that the unique features in Doppler signal, such as phase wrapping and BMA, have to be taken into account before conventional methods can be applied. Nevertheless, simple image processing methods presented here were demonstrated to be crucial for Doppler flow image enhancement. Advanced 3D filtering and adaptive filtering are possible approaches to further improve flow image quality.

Chapter 7 DFR-OCT for brain functional imaging

The relationship between hemodynamic and neuronal activations is of great importance to understand brain functions. Current research in this field majorly relies on several conventional imaging tools including functional magnetic resonance imaging (fMRI), diffused optical imaging (e.g., NIR spectroscopy and imaging) by imaging oxygen metabolic and hemodynamic responses of the interested cerebral tissues. However, these techniques only provide macroscopic images with spatial resolution at ~mm level which is insufficient to resolve individual vascular compartments or neuron cells. Advanced light microscopy such as confocal and milt-photon microscopy offers sub-micron resolution to visualize capillary vasculatures and cellular detains of brain in vivo[77-80], however, there FOV and imaging depth are limited to ~300um[80], thus restricting its utility in imaging neurovascular networks. Other recent optical methods include laminar optical tomography[81] and laser speckle imaging (LSI)[82] to improve the spatial resolution for mapping brain hemodynamic activities by deploying intrinsic hemoglobin absorption contrast. Unfortunately, laminar optical tomography is unable to identify individual vessels. Although LSI can resolve individual blood vessels, it only provides "relative" measures of cerebral blood flow (CBF).

Recently, we demonstrated a dual-imaging modality for high-resolution quantitative imaging of local cerebral blood flow in the rat cortex by combining simultaneous 2D Doppler OCT and full-field laser speckle imaging[83]. Preliminary

studies in tissue flow phantom and cocaine-induced cerebral blood flow changes indicated that by correlating coregistered cortical arterial blood flow, the relative measurement of flow changes by LSCI could be accurately calibrated by the absolute flow imaging provided by SDOCT (least square fit, r2≈0.96), therefore enable quantitative LSI analyses of the spatiotemporal hemodynamic of functional brain activations and thus improved understanding of neural process[83]. In this chapter, we further investigate the possibility to combine 3D DFR-OCT and LSI for high spatiotemporal resolution quantitative CBF monitoring during brain functional challenges.

7.1 Combine DFR-OCT and LSI for cocaine study

7.1.1 Animal model

Cocaine-naive female Sprague–Dawley rats (250–300g/each, n=12) were anesthetized and ventilated with 2% isoflurane mixed in pure oxygen during the surgical procedures. The right carotid artery was catheterized for continuous arterial blood pressure monitoring and the left carotid artery was set apart by a 3.0 suture. A ~ϕ6mm cranial window was created on one lateral side of the parietal bone that exposed the somatosensory and motor cortex area. After the dura was carefully removed, the exposed brain surface was immediately submerged in saline to avoid dehydration which might otherwise result in increased surface scattering and specular reflection. After the surgery, the anesthesia was then switched to α-chloralose using an initial bolus of 50mg/kg followed by continuous infusion of 25mg/kg/hr through the femoral vein during the experiment. To do the drug challenges in the brain, a bolus of cocaine (1mg/kg, i.v.) was administrated through the tail vein followed by a 0.5cc saline. During the experiment, the

physiological parameters of the animal were continuously monitored, including the mean arterial blood pressure (MABP), respiration rate and body temperature (PC-SAM monitor, SA Inc.). In addition, blood gases were periodically measured (ABL 700, Radiometer Medical) to ensure that the rat remained under normal physiological condition. For example, the typical physiological parameters in the baseline were: pH=7.35–7.40, pCO_2=35–45mmHg, pO_2=97.5–100%, MABP=80 ~ 100mmHg and T=36.5–37.5°C.

7.1.2 Image acquisition

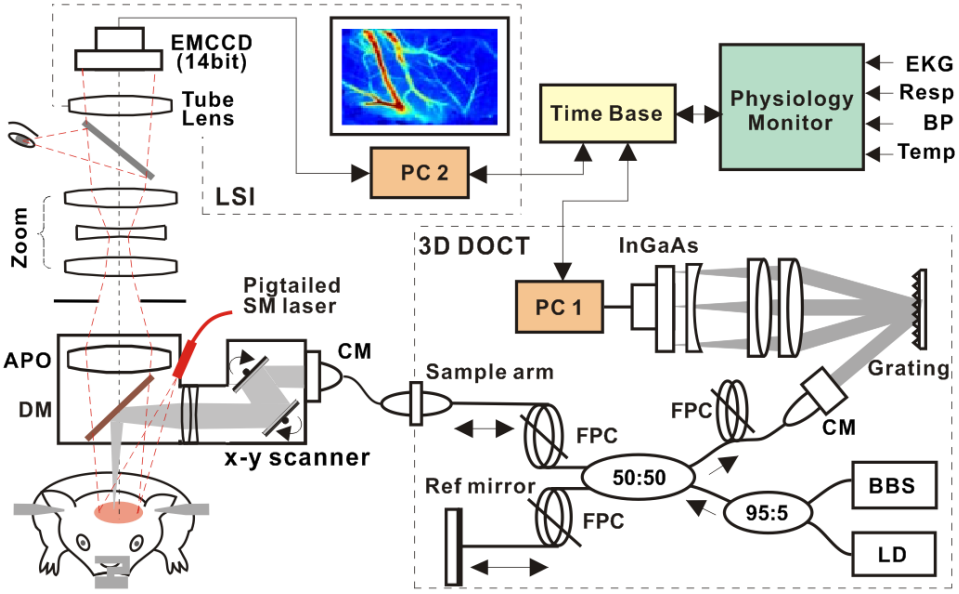

Fig. 7.1 A platform combining 1310nm DFR-OCT and 830nm LSI based on a modified zoom scope. BBS: broadband light source; LD: aiming diode laser; FPC: fiber polarization controller; CM: collimator; DM: dichroic mirror (λ_{DM}=900nm).

As illustrated in Fig. 7.1, a dual-modality imaging platform based on a modified zoom microscope was used to enable simultaneous SDOCT and LSI imaging of the CBF network over a cranial window, in which the LSI and SDOCT systems were combined by a dichroic beam splitter (DM). Here, LSI which is capable of fast *en face* CBF imaging of cortical brain was used to compare with the flow changes quantified by SDOCT. In the

LSI system, a pigtailed SM fiber laser (830nm, 10mW) was used to provide coherent illumination on the cranial window and a 2×/0.22NA objective (APO) was used to relay the cortical image to a 14bit EMCCD. By extraction of flow-induced speckle variance in either time or spatial domain, LSI of cortical CBF mapping can be acquired at high spatiotemporal resolutions (e.g., ~30μm, up to 30Hz) across a large FOV (e.g., $6\times8mm^2$). In the parallel SDOCT system, a pigtailed 18mW broadband source at 1310nm with ~90nm of spectral bandwidth was used for OCT illumination (coherence length $L_c\approx8\mu m$). The sample arm was connected to a scan head mounted on the zoom microscope in which light exiting the SM fiber was collimated (CM) to ~ϕ5mm, scanned transversely (x-y) by a pair of close-loop servo mirrors and focused on cortical brain by a f/50mm achromate which in turn collected the backscattered light from the brain tissue. The light beams from the sample and reference arms were recombined in the detection fiber, spectrally diffracted, focused by a lens group onto a fast linear InGaAs array to detect each interference spectrogram (A-scan) at up to 47kHz. Inverse FFT provided 2D and 3D morphological images of cortical brain, and the transverse and axial resolutions were 15μm and 8μm, respectively. By further applying Hilbert transform with digital-frequency ramping (i.e., DFR-OCT)[74] in the transverse direction to detect flow induced phase change, we were able to provide quantitative 2D and 3D CBF images. During the experiment, LSI was run at ~10frames/s to continuously monitor the CBF changes in response to cocaine challenges, while DFR-OCT was performed at specific time point t_b (baseline) and t_p (plateau during cocaine challenge) to measure the quantitative flow changes induced by cocaine. The two imaging systems were synchronized by a time base together with the physiological parameters of the animal under examination.

7.1.4 Results

A pilot study was first performed to investigate the feasibility of combing LSI and 3D DFR-OCT. The results were presented in Fig. 7.2, where panel (a-c) displays DFR-OCT images in pseudo color to map the CBF network and their flow rate, panel (a) is the corresponding maximum intensity projection (MIP) of the 3D DFR-OCT image, panel (b) presents the image in 3D volume to visualize the microvascular networks and depth profiles, panel(c) shows that owing to 3D imaging capability, a minute CBF ($\phi \approx 13\mu m$) in panel (a, b), descending from 150μm to 750μm under the cortical surface, could be traced and quantitatively measured, which shows the capabilities of 3D DFR-OCT for high-resolution imaging of detailed CBF changes in different layers of the cerebral cortex in a rat brain. Parallel to DFR-OCT, panel (d) shows the LSI image with large field of view (FOV, ~5mm×~3mm) that easily covers the FOV of the simultaneous (~2.2mm×~2.2mm) in red box. Obviously, the *en face* LSI image is highly correlated to the MIP image of DFR-OCT with almost identical CBF network distributions, which enables a possible co-registration between these two imaging modalities, therefore to quantify LSI flow rates by DFR-OCT.

Fig. 7.3 depicts the quantitative CBF change curves measured by LSI and calibrated by DFR-OCT in response to an acute cocaine challenge. Fig. 7.3(a) shows that LSI provides *enface* CBF images over The CBF flow indices ($\nu_1 \approx 7.8k$, $\nu_2 \approx 3.5k$) in different-size vessels (e.g., $\phi_1 \approx 130\mu m$, $\phi_2 \approx 37\mu m$) can be readily differentiated by LSI despite its reliance on relative measurements. Unlike LSI, DFR-OCT enables quantitative 3D imaging of the local CBF network at ~10μm spatial resolution. Fig. 7.3(c) shows a

projected 3D DFR-OCT image of the vascular CBF network ($2.5\times2.5\times2mm^3$) whose enface FOV corresponds to the cortical area landmarked by the dashed rectangle in Fig. 7.3(a). A comparison between the upper and lower panels indicates that both DFR-OCT and LSI imaging modalities were able to track the CBF increase as indicated by flow rates (i.e., in pseudo color) both in the larger and smaller vessels in response to cocaine challenge. Specifically, the DFR-OCT measured flow profiles for vessels 1 and 2 before and after cocaine injection were plotted, indicating that the averaged flow rates were increased from $\nu_1(t_b)\approx3.1$mm/s, $\nu_2(t_b)\approx1.4$mm/s to $\nu_1(t_p)\approx4.1$mm/s, $\nu_2(t_p)\approx2.0$mm/s. These values were used to calibrate LSI measurements to yield the quantitative and normalized CBF changes curves in Fig. 7.3(e) and (f) respectively, which enables the high spatiotemporal resolution of LSI to distinguish the time-lapse CBF responses to cocaine in the different vessels (e.g., curves 1, 2) and within the brain tissue (e.g., tissue perfusion, green curve). It is noteworthy that the transient decrease in CBF at 3-4min following cocaine administration was consistently observed in all experiments (e.g., Fig. 3, Fig. $4A_5$). This early dynamic change in CBF (e.g., the 'dipping' effect) did not appear in the vehicle animals challenged by saline (0.1cc/100g, i.v., data not shown), suggesting that it was a pharmacological effect from acute cocaine administration rather than measurement artifacts. Similar effects on CBV and BOLD were observed in previous MRI studies[89-90]. In contrast to the "dip", which was not seen with saline administration, the immediate transient increase in CBF (peaked within 1min) upon cocaine administration was also observed after saline administration, indicating that it is most likely caused by the bolus flush of solution.

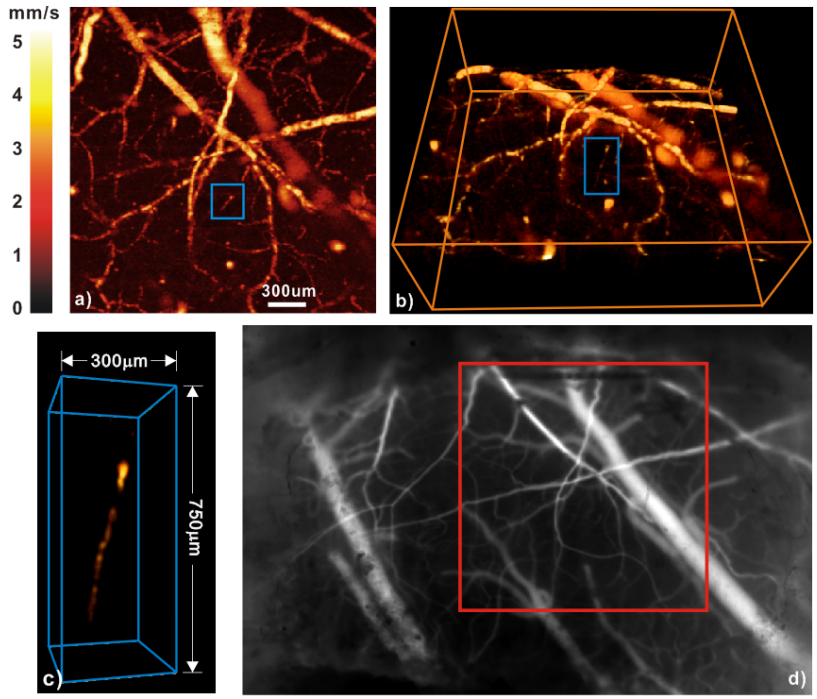

Fig. 7.2 3D DFR-OCT images of vascular CBF network compares to LSI. a), b) Maximal projection and 3D CBF images, respectively; c) Magnified view of a minute CBF marked by the blue box in the panels a) and b); d) *en face* LSI image with larger FOV, the red box encloses the area corresponding to DFR-OCT.

In summary, this study demonstrated that the combined DFR-OCT and LSI imaging modality enables: 1) Full-Field and high spatial resolution: LSI enables imaging of the vascular CBF network at high spatial resolution (~30μm) and over a large FOV ($4\times5mm^2$). By co-registering with DFR-OCT, quantitative 3D imaging of the CBF network is permitted over a cubic cortical volume of $2.5\times2.5\times2mm^3$ at ~10μm resolution. Such high spatial resolution and large FOV will bridge the gap between conventional mesoscopic (e.g., fMRI, PET) and microscopic (e.g., confocal, 2-photon) imaging modalities to study cerebral neuron-vascular coupling effects which require both high resolution and large field of view. 2) High temporal resolution: The frame rates of our current LSI and 2D DFR-OCT are 10fps and 47fps and can be easily upgraded to 30fps and 94fps (i.e., 0.25Hz for 3D DFR-OCT). Such high temporal-resolution 2D and 3D

CBF imaging enables to capture transient neurovascular events (as shown in this study for the case of cocaine) to provide new insights to advance our understanding of the coupling between neuronal activity, metabolism and hemodynamic changes and the perturbation by pharmacological agents and or animal models of brain diseases.

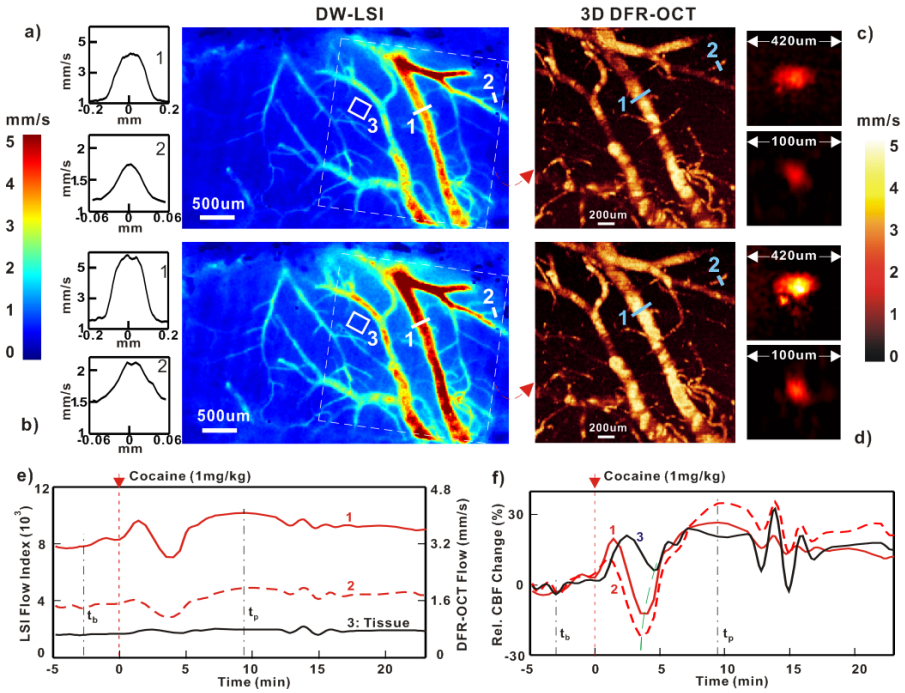

Fig. 7.3 3D DFR-OCT quantifies CBF changes in LSI. (a, c) prior and (b, d) post cocaine injection (1mg/kg, i.v.). Relative 1D and quantitative 2D flow profiles of vessels 1, 2 are shown in the left and right small panels. Flow depths of $z_{1,2}$=240, 330um are given by 3D OCT. The cocaine-evoked CBF changes from the selected ROIs of 1 (large), 2 (small) and 3 (tissue perfusion) are shown in panels e)-f) where t_b and t_p are baseline and elevated CBF periods of DFR-OCT acquisition.

7.2 Angiogram enhanced DFR-OCT

By taking advance of fast imaging rate and high detection sensitivity of spectral-domain optical coherence tomography (SDOCT), a number of angiographic approaches have been recently reported[69, 91-92], which showed significantly improved sensitivity and resolution for visualizing detailed 3D cerebral microvasculature. However, quantitative imaging of capillary CBF network, critical to brain functional studies,

remains a challenge due to excessive phase noise in the detection of capillary CBF induced minute Doppler phase changes. In this section, we present a method tailored to facilitate angiography-enhanced 3D Doppler OCT that enables quantitative imaging of cortical microvasculature. In addition, we demonstrate its performance to quantify capillary CBF changes in response to brain functional challenge using an animal cerebral hypercapnia model *in vivo*.

A mouse hypercapnia model was used to examine the utility of the techniques for providing quantitative CBF imaging of brain functional changes (e.g., cerebral vasodilation)[91], in which a female FVB mouse of 20g body weight was anesthetized first with inhalational 2% isoflurane mixed with 100% O_2 and mounted on a custom stereotaxic frame. A ϕ5mm cranial window was created on the dorsal side of the mouse brain and the exposed cortical surface was covered with 2% agarose gel to avoid dehydration and minimize tissue deformation during the imaging study. After the baseline CBF imaging data was acquired, hypercapnia was induced by switching the ventilation from 100% O_2 to a mixture of 5% CO_2 and 95% O_2 (blood gas) during which the CBF changes in response to cerebral vasodilation were continuously monitored by LSI and DFR-OCT.

Fig. 7.4 illustrates the procedure that combines OCT angiography and DFR-OCT to enhance capillary CBF quantification. As shown in Fig. 7.4(a-b), an alternative fast–slow transverse scan scheme was used for each B-scan (x-z plane, $x = x_1 \rightarrow x_2$), so that 4 consecutive 2D SDOCT images were first acquired at 47kHz to derive a standard deviation graph (STD) for 2D OCT angiograph of the cortical cerebral vasculature[92] in Fig. 7.4(c). A slow-scan was followed to acquire the corresponding SDOCT image at

5kHz and post-processed by digital frequency ramping to derive each DRF-OCT image of quantitative CBFs in Fig. 7.4(d). Noteworthily, an A-scan rate of 5kHz was empirically determined to optimize imaging rate and minute-flow delectability. Fig. 7.4(e-f) show the corresponding MIP images of 3D OCT angiograph and 3D DFR-OCT.

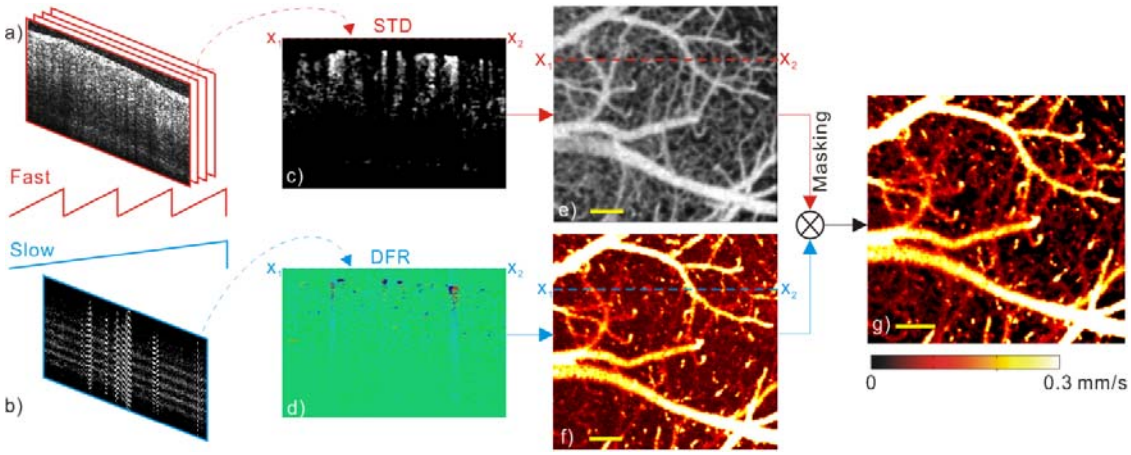

Fig. 7.4 Image formation of angiography-enhanced DFR-OCT (aDFR-OCT). a, c) 4 sequential 2D SDOCT images (500×1k) were acquired at 47kHz to derive a normalized standard deviation image (STD); b, d) 2D spectral graph (2k×1k) was acquired at 5kHz to derive a 2D DFR-OCT image (downsized to 500×1k); e, f) MIPs of 3D OCT angiograph and 3D DFR-OCT (500×500×1k); g) MIP of 3D aDFR-OCT by multiplexing binarized e) with f), enabling 3D quantitative CBF imaging with capillary details. Image size: $1.25\times1.25\times1mm^3$ on cortical brain.

A comparison between these two image sets indicates that although DFR-OCT was quantitative, it was prone to background phase noise to affirmatively detect minute CBFs under 0.06mm/s (apparent flow rate, without angle correction); whereas OCT angiography clearly provided superior sensitivity to resolve the capillary CBF network. Thereafter, to combine the merits of these two modalities, the capillary CBFs in DFR-OCT can be uncovered by spatially filtering the noise background using a 3D microvascular mask provided by the OCT angiogram. More specifically, Fig. 7.4(e) was binarized to form a 3D angiographic mask M, i.e., $M(x,y,z)\equiv1$ if $\sigma(x,y,z)\geq\sigma_T$ and

$M(x,y,z)\equiv 0$ if $\sigma(x,y,z)<\sigma_T$, where σ_T (e.g., $\sigma_T=0.2$, $p<0.01$) was derived by statistically evaluating the contrast-to-noise ratio (CNR) of Fig. 7.4(e). The 3D binary matrix M was then multiplied with Fig. 7.4(f) to eliminate the noise background of DFR-OCT to yield the final angiography-enhanced quantitative flow image aDFR-OCT. Fig. 7.4(g) clearly shows that aDFR-OCT based on a simple masking algorithm enabled visualization of the capillary CBF network which was otherwise barely identifiable in the noise background of DFR-OCT (f).

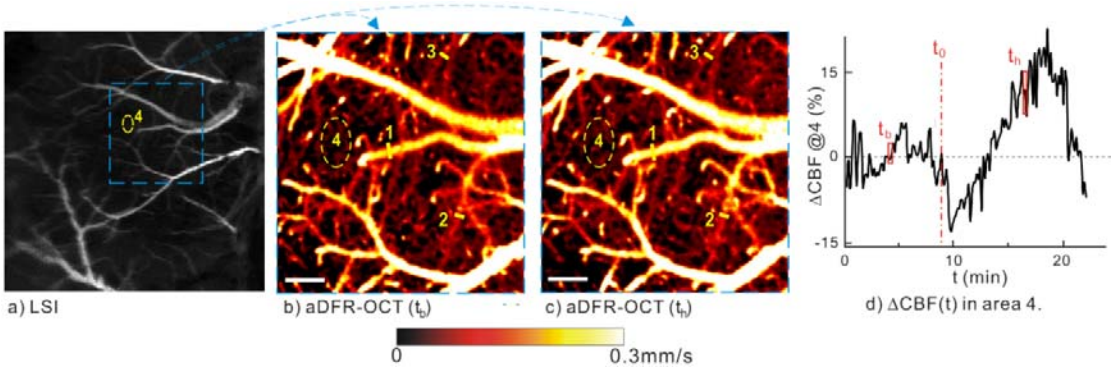

Fig. 7.5 Quantitative functional imaging of mouse cerebral hemodynamic changes induced by hypercapnia. a) LSI image base line t_b (FOV: 4×5 mm^2); b, c) MIPs of 3D aDFR-OCT acquired at t_b and at t_h=6min after hypercapnia (FOV: 1.25×1.25×1mm^3); d) Time course of perfusion rate change within RIO 4 measured by LSI to compare with aDFR-OCT. Scale bar: 200μm. 1-3: large, small and capillary CBFs; 4: perfusion flow.

To examine whether aDFR-OCT was able to image quantitative hemodynamic changes under brain functional challenge, we measured the cortical capillary CBF changes of an animal in response to hypercapnia, which has been known to induce cerebral hyperperfusion. Results of LSI at t_b (baseline) and aDFR-OCT at t_b and at $t_h\approx$6min after hypercapnia are shown in Fig. 7.5(a, b, c), respectively. Apparently, the overall CBF increase can be seen in Fig. 7.5(c), and a detailed comparison of 4 typical regions of interest (e.g., ROIs 1-4) indicates that the relative flow rate increase of flow 1 (larger, ~ϕ65μm) was $\Delta v_1=[v_1(t_h)-v_1(t_b)]/v_1(t_b)\approx 25\%$. Flow 2 (median, ~ϕ35μm) was

barely resolvable and flow 3 (small, ~ϕ15μm) was unresolvable by DFR-OCT; however, the measured increases by aDFR-OCT were $\Delta v_2 \approx 28\%$ and $\Delta v_3 \approx 21\%$, respectively. Tissue perfusion rate within ROI 4 (i.e., resulting from local unresolvable capillary flows) increased $\Delta v_4 \approx 14\%$. To further compare with the LSI results, for the larger vessel 1 resolvable by other methods, the aDFR-OCT measurement of $\Delta v_1 \approx 25\%$ correlates well with that of $\Delta v_1 \approx 22\%$ by LSI. More interestingly, Fig. 7.5(d) shows that perfusion rate increase $\Delta v_4 \approx 14\%$ by aDFR-OCT approximately matches $\Delta v_4 \approx 12\%$ by LSI. The underestimate of Δv_4 compared to $\Delta v_1 \sim \Delta v_3$ was likely due to the fact of fractural averaging effect within the tissue volume instead of pure flow measures within the 3 flows.

In summary, we present a new method, aDFR-OCT, which combines OCT-angiography and DFR-OCT to enhance quantitative imaging of the cortical capillary CBF network. Such imaging techniques may play an important role in many neuroscience studies that require quantitative and high spatiotemporal resolution imaging of neurovascular hemodynamics and their functional changes. Results of animal study demonstrate the potential of aDFR-OCT to uncover the capillary CBF network and quantitatively measure hypercapnia-induced cerebral hyperperfusion. It is noteworthy that the resolution of this technique is affected by the accuracy of the binarizing angiography mask M which was derived by a simple statistical test of CNR. Subsequently, the sizes of the uncovered capillary CBFs in Fig. 7.4(g) tended to be overestimated in comparison to OCT angiograph in Fig. 7.4(e). More effective image processing methods can be applied to derive more accurate binarizing mask and thus

further enhance the visualization of the capillary CBF network. Additionally, it should be noted that Fig. 7.4-Fig. 7.5 showed apparent flows resulting in underestimated flow rates. Therefore, angle correction in 3D image processing is needed for absolute flow quantification.

Chapter 8 **Conclusions and future work**

OCT is an emerging non-invasive optical imaging technique that provides cross-sectional imaging capabilities with sub-10μm spatial resolution and 1~3mm imaging depth. Since its first demonstration, advances to OCT techniques have greatly improved its performances in all aspects including imaging speed, image quality and resolution. Moreover, as a fiber-optic device, OCT imaging probe can be miniaturized to accommodate special circumstances, such as endoscopic applications. With this unique feature, OCT can be readily combined with advanced MEMS techniques to provide a new approach for disease diagnosis in internal organs. Recently studies already demonstrate OCT as a powerful tool that greatly facilitates clinical diagnosis in various tissues and internal organs.

However, because of its physical limitations, OCT suffers some intrinsic imperfections such as excessive speckle noise and limited imaging depth. In addition, numerous problems concerning signal processing and retrieving have been raised by new technologies such as Fourier domain OCT and Doppler OCT. This dissertation describes a range of methods to solve some of these existing problems, therefore, to enhance the utility of SDOCT for both pathological and physiological/functional studies. More specifically, Chapter 3 proposes a time-lapse ultrahigh resolution OCT for sub-cellular imaging. With a simple averaging of co-registered images the sub-cellular structures were efficiently enhanced from OCT speckle noise. The method was also demonstrated in 3D

imaging, allowing for the differentiation of cancerous and normal tissue by accurately measuring the cell nuclear size. Chapter 4 compares ultrasound and OCT for cancer diagnosis, the results shows OCT provides better diagnosis than ultrasound providing superior spatial resolution while ultrasound is able to offer deeper imaging depth, thus enabling the grading of tumors up to stage 2~3. Combining them for parallel endoscopic imaging can potentially facilitate such diagnosis.

Besides the utility of OCT for pathological imaging, recent developments in OCT for functional imaging, in particular the Doppler OCT, is quickly becoming a research focus by offering quantitative measurement of dynamic flows. However, Doppler OCT suffers a major drawback from excessive phase noise. Chapter 5 describes a DFRM which provides ~6dB SNR improvement of the Doppler flow image at no hardware cost. Several complementary phase processing methods were discussed in Chapter 6 to deal with specific problems in DFR-OCT. These methods include computation acceleration, bulky motion artifacts removal, complex domain phase noise filtering and angiogram base vascular screening. The DFR-OCT was applied to animal brain studies to visualize micro-vascular networks and measure drug induced CBF changes and demonstrated abilities as a powerful imaging tool for blood flow based functional researches.

To further improve the performances of SDOCT and extend its applications, future developments will be focusing on:

1）SDuOCT has shown its capability to differentiate cancerous tissue from normal tissue by detecting the cell nuclear size changes in *ex vivo* animal studies. More data from different lesions, such as hyperplasia, dysplasia, CIS and papillary

tumors, are required for a full assessment of its potential to accurately diagnosis diseases and grade cancers.

2）To enable *in vivo* imaging capabilities the uOCT system, especially the sample probe, needs to be integrated into endoscope by utilizing MEMS mirror or other miniaturization techniques. This also raises another challenge to the time lapse frame averaging method since the severe motion artifacts during *in vivo* studies could ruin the inter-frame correlation. This therefore hinders the accurate frame registration and averaging for speckle noise removal. Potential solutions are a) faster imaging speed b) 3D image co-registration and c) probe design that temporally immobilizes the tissue for short time imaging.

3）Chapter 6 describes the new algorithm of DFR-OCT with GPU implementation to shorten the half computation. Since the processing was done using MATLAB, flow reconstruction takes too long time to display the flow images instantaneously. In the future, DFRM implementation based C or other dedicated programming languages are necessary to enable instantaneous or even real-time imaging with the power of GPU or similar low cost supercomputing infrastructures.

4）The dynamic range of Doppler OCT is limited to [-π, π] because of the phase wrapping effect. Although it can be corrected to some extent in big blood vessels where phase wrapping shows as concentric rings, in many cases the Doppler signal can easily exceed the measurement range multiple times to ruin quantitative measurement. While OCT A-line rate has been improved substantially by advances to the technique to extend the measurement range, the flow sensitivity declines reciprocal to the A-line rate. Therefore, a method or

technique to enable Doppler OCT to widen the velocity dynamic range and high sensitivity is desirable and challenging. Possible solutions are multi-beam scanning or fast patterned scanning[93] to generate variable time delays between adjacent A-lines in different dimensions. The long delay can boost the Doppler phase changes to enhance the sensitivity for slow flows while the short delay constricts the changes in fast flow to avoid phase wrapping.

5）OCT only measures the Doppler signal generated by the velocity components along the optic axis, i.e., $v_{oct} = v\cos\theta$ where θ is the angle between the vessel and the optic axis. The flow orientation can greatly affect the results and therefore needs to be incorporated to the measurement to recover the absolute flow rate. Although the flow orientation can be retrieved based on 3D image, the overall calculation for every vessel can be complex and computationally expensive. Currently only the absolute flow rate of the specific vessel of interest is calculated when needed. A method that enables absolution flow measurement or fast angular correction is highly desirable and could greatly benefit the functional studies.

6）*in vivo* functional studies are consider to be highly complicated and could be affected by numerous physiological parameters. For instance, to validate and confirm the discoveries of the Doppler OCT in brain functional studies, it is necessary to incorporate other measurements to such as SEP for neuronal activities, an oxymeter for oxygenation level, fluorescence imaging for targeted ion concentration, etc. Such multimodality systems will provide unprecedented comprehensive measurements to deepen the understanding of brain functions. On

the other hand, more systematic experiments need to be design to help understand and interpret the data from such complicated system.

7）The methods presented in this dissertation have been demonstrated to enhance the performances and functionalities of our SDOCT systems. These improvements can potentially expand the applications of SDOCT to many relevant biological researches including wound healing assessment, tumor grading and tumorigenesis in variant biological tissues. More detailed animal and human data and analysis are required to investigate and validate those applications.

References

1. Andersen, P.E., Optical coherence tomography. 2004, Optics and Plasma Research Department, Risø National Laboratory.
2. Huang, D., et al., Optical Coherence Tomography. Science, 1991. **254**(5035): p. 1178-1181.
3. Leitgeb, R.A., et al., Real-time measurement of in vitro flow by Fourier-domain color Doppler optical coherence tomography. Optics Letters, 2004. **29**(2): p. 171-173.
4. Vakoc, B.J., et al., Phase-resolved optical frequency domain imaging. Optics Express, 2005. **13**(14): p. 5483-5493.
5. Wojtkowski, M., et al., Three-dimensional retinal imaging with high-speed ultrahigh-resolution optical coherence tomography. Ophthalmology, 2005. **112**(10): p. 1734-1746.
6. Chen, Z.P., et al., Optical Doppler tomography. Ieee Journal of Selected Topics in Quantum Electronics, 1999. **5**(4): p. 1134-1142.
7. S. Yazdanfar, M. D. Kulkarni, and J. A. Izatt, High resolution imaging of in vivo cardiac dynamics using color Doppler optical coherence tomography. Optics Express, 1997. **1**(13): p. 424-431.
8. de Boer, J.F., et al., Imaging thermally damaged tissue by polarization sensitive optical coherence tomography. Optics Express, 1998. **3**(6): p. 212-218.
9. Morgner, U., et al., Spectroscopic optical coherence tomography. Optics Letters, 2000. **25**(2): p. 111-113.
10. Wang, X.D. and L.H.V. Wang, Propagation of polarized light in birefringent turbid media: A Monte Carlo study. Journal of Biomedical Optics, 2002. **7**(3): p. 279-290.
11. Bouma, B., et al., High-Resolution Optical Coherence Tomographic Imaging Using a Mode-Locked Ti-Al2o3 Laser Source. Optics Letters, 1995. **20**(13): p. 1486-1488.
12. Boppart, S.A., et al., In vivo cellular optical coherence tomography imaging. Nature Medicine, 1998. **4**(7): p. 861-865.
13. Drexler, W., Ultrahigh-resolution optical coherence tomography. Journal of Biomedical Optics, 2004. **9**(1): p. 47-74.
14. Tang, S., et al., Imaging subcellular scattering contrast by using combined optical coherence and multiphoton microscopy. Optics Letters, 2007. **32**(5): p. 503-505.
15. Pan, Y.T., et al., Subcellular imaging of epithelium with time-lapse optical coherence tomography. Journal of Biomedical Optics, 2007. **12**(5): p. -.
16. Tearney, G.J., et al., In vivo endoscopic optical biopsy with optical coherence tomography. Science, 1997. **276**(5321): p. 2037-2039.

17. Pan, Y.-T. and D.L. Farkas, Dual-color, 3-D imaging of biological tissues using optical coherence tomography. Journal of Biomedical Optics, 1998. **3**(4): p. 446-455.
18. Wang, Z.G., et al., Assessment of dermal wound repair after collagen implantation with optical coherence tomography. Tissue Engineering Part C-Methods, 2008. **14**(1): p. 35-45.
19. Feldchtein, F.I., et al., In vivo OCT imaging of hard and soft tissue of the oral cavity. Optics Express, 1998. **3**(6): p. 239-250.
20. Izatt, J.A., et al., Optical coherence tomography and microscopy in gastrointestinal tissues. Ieee Journal of Selected Topics in Quantum Electronics, 1996. **2**(4): p. 1017-1028.
21. Sergeev, A.M., et al., In vivo endoscopic OCT imaging of precancer and cancer states of human mucosa. optics Express, 1997. **1**(13): p. 432-440.
22. Mikhail-Hanna, N., et al., Optical coherence tomography of the lung and lower airway. Chest, 2003. **124**(4): p. 77s-77s.
23. Zagaynova, E.V., et al., In vivo optical coherence tomography feasibility for bladder disease. Journal of Urology, 2002. **167**(3): p. 1492-1496.
24. Pan, Y.T., et al., Detection of tumorigenesis in rat bladders with optical coherence tomography. Medical Physics, 2001. **28**(12): p. 2432-2440.
25. Xie, T.Q., M.L. Zeidel, and Y.T. Pan, Detection of tumorigenesis in urinary bladder with optical coherence tomography: optical characterization of morphological changes. Optics Express, 2002. **10**(24): p. 1431-1443.
26. Escobar, P.F., et al., Diagnostic efficacy of optical coherence tomography in the management of preinvasive and invasive cancer of uterine cervix and vulva. International Journal of Gynecological Cancer, 2004. **14**(3): p. 470-474.
27. Brezinski, M.E., et al., Assessing atherosclerotic plaque morphology: Comparison of optical coherence tomography and high frequency intravascular ultrasound. Heart, 1997. **77**(5): p. 397-403.
28. Bouma, B.E. and G.J. Tearney, Handbook of Optical Coherence Tomography, ed. . 2002: Marcel Dekker, Inc.
29. Tearney, G.J., B.E. Bouma, and J.G. Fujimoto, High-speed phase- and group-delay scanning with a grating-based phase control delay line. Optics Letters, 1997. **22**(23): p. 1811-1813.
30. Ha¨usler, G. and M.W. Lindner, COHERENCE RADAR AND SPECTRAL RADAR—NEW TOOLS FOR DERMATOLOGICAL DIAGNOSIS. Journal of Biomedical Optics, 1998. **3**(1): p. 21-31.
31. Leitgeb, R., C.K. Hitzenberger, and A.F. Fercher, Performance of fourier domain vs. time domain optical coherence tomography. Optics Express, 2003. **11**(8): p. 889-894.
32. FFTW home page, http://fftw.org/.
33. Tiff library and tools for TIFF images, http://gnuwin32.sourceforge.net/packages/tiff.htm.
34. Microsoft Inc., http://msdn.microsoft.com/en-us/library/dd370987(VS.85).aspx.
35. Drexler, W., et al., In vivo ultrahigh-resolution optical coherence tomography. Optics Letters, 1999. **24**(17): p. 1221-1223.

36. Leitgeb, R.A., et al., Ultrahigh resolution Fourier domain optical coherence tomography. Optics Express, 2004. **12**(10): p. 2156-2165.
37. Hitzenberger, C.K., et al., Dispersion effects in partial coherence interferometry: Implications for intraocular ranging. Journal of Biomedical Optics, 1999. **4**(1): p. 144-151.
38. Liu, X.M., M.J. Cobb, and X.D. Li, Rapid scanning all-reflective optical delay line for real-time optical coherence tomography. Optics Letters, 2004. **29**(1): p. 80-82.
39. Xie, T.Q., Z.G. Wang, and Y.T. Pan, Dispersion compensation in high-speed optical coherence tomography by acousto-optic modulation. Applied Optics, 2005. **44**(20): p. 4272-4280.
40. Fercher, A.F., et al., Numerical dispersion compensation for Partial Coherence Interferometry and Optical Coherence Tomography. Optics Express, 2001. **9**(12): p. 610-615.
41. Cense, B., et al., Ultrahigh-resolution high-speed retinal imaging using spectral-domain optical coherence tomography. Optics Express, 2004. **12**(11): p. 2435-2447.
42. Wojtkowski, M., et al., Ultrahigh-resolution, high-speed, Fourier domain optical coherence tomography and methods for dispersion compensation. Optics Express, 2004. **12**(11): p. 2404-2422.
43. Yasuno, Y., et al., In vivo high-contrast imaging of deep posterior eye by 1-mu m swept source optical coherence tomography and scattering optical coherence angiography. Optics Express, 2007. **15**(10): p. 6121-6139.
44. Makita, S., T. Fabritius, and Y. Yasuno, Full-range, high-speed, high-resolution 1-mu m spectral-domain optical coherence tomography using BM-scan for volumetric imaging of the human posterior eye. Optics Express, 2008. **16**(12): p. 8406-8420.
45. Park, B.H., et al., Real-time fiber-based multi-functional spectral-domain optical coherence tomography at 1.3 mu m. Optics Express, 2005. **13**(11): p. 3931-3944.
46. Wang, Z.G., et al., Increasing the imaging depth of spectral-domain OCT by using interpixel shift technique. Optics Express, 2006. **14**(16): p. 7014-7023.
47. Yasuno, Y., et al., Three-dimensional and high-speed swept-source optical coherence tomography for in vivo investigation of human anterior eye segments. Optics Express, 2005. **13**(26): p. 10652-10664.
48. Mujat, M., et al., Autocalibration of spectral-domain optical coherence tomography spectrometers for in vivo quantitative retinal nerve fiber layer birefringence determination. Journal of Biomedical Optics, 2007. **12**(4): p. -.
49. Dorrer, C., et al., Spectral resolution and sampling issues in Fourier-transform spectral interferometry. Journal of the Optical Society of America B-Optical Physics, 2000. **17**(10): p. 1795-1802.
50. Yuan, Z.J., H.G. Ren, and Y.T. Pan, Accurate k-sampling and Dispersion Compensation in Spectral-domain Ultrahigh-resolution Optical Coherence Tomography. Applied Optics, 2008: p. under review.
51. Cancer Facts&Figurs. http://www.cancer.org/downloads/STT/CAFF2006PWSecured.pdf.

52. Zhenguo Wang , C.S.D.L., Wayne Waltzer , Jingxuan Liu , Huikai Xie , Zhijia Yuan In vivo Bladder Imaging with MEMS-based Endoscopic Spectral Domain Optical Coherence Tomography. Journal of Biomedical Optics, 2007.
53. Malone, P.R., et al., The Use of Transabdominal Ultrasound in the Detection of Early Bladder-Tumors. British Journal of Urology, 1986. **58**(5): p. 520-522.
54. Koraitim, M., et al., Transurethral Ultrasonographic Assessment of Bladder-Carcinoma - Its Value and Limitation. Journal of Urology, 1995. **154**(2): p. 375-378.
55. Tanaka, S., et al., Clinical usefulness of high-frequency ultrasound probes (HFUP) for new invasion depth diagnosis in submucosal colorectal carcinoma. Gastrointestinal Endoscopy, 2002. **56**(4): p. S146-S146.
56. Fishman, D.A., et al., The role of ultrasound evaluation in the detection of early-stage epithelial ovarian cancer. American Journal of Obstetrics and Gynecology, 2005. **192**(4): p. 1214-1221.
57. Char, D.H., et al., 20 MHz high frequency ultrasound assessment of scleral and intraocular conjunctival squamous cell carcinoma. British Journal of Ophthalmology, 2002. **86**(6): p. 632-635.
58. Xiao, Z., et al., Characterization of a novel transplantable orthotopic rat bladder transitional cell tumour model. British Journal of Cancer, 1999. **81**(4): p. 638-646.
59. Chen, Z.P., et al., Noninvasive imaging of in vivo blood flow velocity using optical Doppler tomography. Optics Letters, 1997. **22**(14): p. 1119-1121.
60. Barton, J.K., A.J. Welch, and J.A. Izatt, Investigating pulsed dye laser-blood vessel interaction with color Doppler optical coherence tomography. Optics Express, 1998. **3**(6): p. 251-256.
61. Zhao, Y.H., et al., Phase-resolved optical coherence tomography and optical Doppler tomography for imaging blood flow in human skin with fast scanning speed and high velocity sensitivity. Optics Letters, 2000. **25**(2): p. 114-116.
62. Michaely, R., et al., Vectorial reconstruction of retinal blood flow in three dimensions measured with high resolution resonant Doppler Fourier domain optical coherence tomography. Journal of Biomedical Optics, 2007. **12**(4): p. -.
63. Ahn, Y.C., W. Jung, and Z.P. Chen, Quantification of a three-dimensional velocity vector using spectral-domain Doppler optical coherence tomography. Optics Letters, 2007. **32**(11): p. 1587-1589.
64. Leitgeb, R.A., et al., Real-time assessment of retinal blood flow with ultrafast acquisition by color Doppler Fourier domain optical coherence tomography. Optics Express, 2003. **11**(23): p. 3116-3121.
65. White, B.R., et al., In vivo dynamic human retinal blood flow imaging using ultra-high-speed spectral domain optical Doppler tomography. Optics Express, 2003. **11**(25): p. 3490-3497.
66. Wang, R.K.K. and Z.H. Ma, Real-time flow imaging by removing texture pattern artifacts in spectral-domain optical Doppler tomography. Optics Letters, 2006. **31**(20): p. 3001-3003.
67. Chen, Y.L., P. Willett, and Q. Zhu, Frequency tracking in optical Doppler tomography using an adaptive notch filter. Journal of Biomedical Optics, 2007. **12**(1).

68. Ren, H.W. and X.D. Li, Clutter rejection filters for optical Doppler tomography. Optics Express, 2006. **14**(13): p. 6103-6112.
69. Wang, R.K., et al., Three dimensional optical angiography. Optics Express, 2007. **15**(7): p. 4083-4097.
70. Szkulmowski, M., et al., Flow velocity estimation using joint Spectral and Time Domain Optical Coherence Tomography. Optics Express, 2008. **16**(9): p. 6008-6025.
71. Tao, Y.K., A.M. Davis, and J.A. Izatt, Single-pass volumetric bidirectional blood flow imaging spectral domain optical coherence tomography using a modified Hilbert transform. Optics Express, 2008. **16**(16): p. 12350-12361.
72. Wang, R.K.K. and S. Hurst, Mapping of cerebro-vascular blood perfusion in mice with skin and skull intact by Optical Micro-AngioGraphy at 1.3 mu m wavelength. Optics Express, 2007. **15**(18): p. 11402-11412.
73. An, L. and R.K.K. Wang, In vivo volumetric imaging of vascular perfusion within human retina and choroids with optical micro-angiography. Optics Express, 2008. **16**(15): p. 11438-11452.
74. Yuan, Z.J., et al., A digital frequency ramping method for enhancing Doppler flow imaging in Fourier-domain optical coherence tomography. Optics Express, 2009. **17**(5): p. 3951-3963.
75. AccelerEyes, http://www.accelereyes.com/. 2010.
76. Yu, L.F. and Z.P. Chen, Doppler variance imaging for three-dimensional retina and choroid angiography. Journal of Biomedical Optics, 2010. **15**(1): p. -.
77. Hudetz, A.G., Blood flow in the cerebral capillary network: a review emphasizing observations with intravital microscopy. Microcirculation, 1997. **4**(2): p. 233-52.
78. Villringer, A., et al., Capillary perfusion of the rat brain cortex. An in vivo confocal microscopy study. Circ Res, 1994. **75**(1): p. 55-62.
79. Kleinfeld, D., et al., Fluctuations and stimulus-induced changes in blood flow observed in individual capillaries in layers 2 through 4 of rat neocortex. Proc Natl Acad Sci U S A, 1998. **95**(26): p. 15741-6.
80. Dirnagl, U., et al., Three-dimensional reconstruction of the rat brain cortical microcirculation in vivo. J Cereb Blood Flow Metab, 1991. **11**(3): p. 353-60.
81. Hillman, E.M., et al., Laminar optical tomography: demonstration of millimeter-scale depth-resolved imaging in turbid media. Opt Lett, 2004. **29**(14): p. 1650-2.
82. Dunn, A.K., et al., Dynamic imaging of cerebral blood flow using laser speckle. Journal of Cerebral Blood Flow and Metabolism, 2001. **21**(3): p. 195-201.
83. Luo, Z.C., et al., Optical coherence Doppler tomography quantifies laser speckle contrast imaging for blood flow imaging in the rat cerebral cortex. Optics Letters, 2008. **33**(10): p. 1156-1158.
84. Du, C.W., et al., Cocaine increases the intracellular calcium concentration in brain independently of its cerebrovascular effects. Journal of Neuroscience, 2006. **26**(45): p. 11522-11531.
85. Du, C., et al., Detection of Ca2+-dependent neuronal activity simultaneously with dynamic changes in CBV and tissue oxygenation from the live rat brain. Journal of Innovative Optical Health Sciences, 2009. **2**(2): p. 189-200.

86. Du, C.W., et al., Simultaneous detection of blood volume, oxygenation, and intracellular calcium changes during cerebral ischemia and reperfusion in vivo using diffuse reflectance and fluorescence. Journal of Cerebral Blood Flow and Metabolism, 2005. **25**(8): p. 1078-1092.
87. Luo, Z.C., et al., Simultaneous imaging of cortical hemodynamics and blood oxygenation change during cerebral ischemia using dual-wavelength laser speckle contrast imaging. Optics Letters, 2009. **34**(9): p. 1480-1482.
88. Luo, Z., et al., Optical coherence Doppler tomography quantifies laser speckle contrast imaging for blood flow imaging in the rat cerebral cortex. Opt Lett, 2008. **33**(10): p. 1156-8.
89. Luo, F., et al., Characterization of effects of mean arterial blood pressure induced by cocaine and cocaine methiodide on BOLD signals in rat brain. Magnetic Resonance in Medicine, 2003. **49**(2): p. 264-270.
90. Schwarz, A.J., et al., Functional MRI using intravascular contrast agents: detrending of the relative cerebrovascular (rCBV) time course. Magnetic Resonance Imaging, 2003. **21**(10): p. 1191-1200.
91. Srinivasan, V.J., et al., Rapid volumetric angiography of cortical microvasculature with optical coherence tomography. Optics Letters, 2010. **35**(1): p. 43-45.
92. Mariampillai, A., et al., Optimized speckle variance OCT imaging of microvasculature. Optics Letters, 2010. **35**(8): p. 1257-1259.
93. Grulkowski, I., et al., Scanning protocols dedicated to smart velocity ranging in Spectral OCT. Optics Express, 2009. **17**(26): p. 23736-23754.